



Norwegian University of
Science and Technology

LNG - Leakage, spreading and fire

Magnus M Skinnemoen

Master of Science in Mechanical Engineering

Submission date: June 2016

Supervisor: Ivar Ståle Ertesvåg, EPT

Co-supervisor: Kjell Erik Rian, ComputIT AS
Rune N. Kleiveland, ComputIT AS
Nils Inge Lilleheie, ComputIT AS

Norwegian University of Science and Technology
Department of Energy and Process Engineering

EPT-M-2016-119

MASTEROPPGAVE

for

Student Magnus Magnussen Skinnemoen

Våren 2016

LNG - Utslepp, spreiiing og brann*LNG - leakage, spreading and fire***Bakgrunn**

Stadig meir naturgass vert transportert som LNG. Styresmakter og næringa er interesserte i å sikre folk og materiell mot uhell. Korleis kan vi redusere skadeverknadene om ei ulukke likevel skulle skje? I denne samanhengen vil det vere svært viktig for tryggleiken å kunne modellere og rekne på utslepp og spreiiing av LNG for realistiske vilkår, og eventuelt påfølgjande eksplosjon og brann

Oppgåva er i samarbeid med ComputIT AS i Trondheim og kan sjåast i samanheng med tidlegare oppgåver innanfor temaet LNG ved den same verksemda.

I oppgåva skal studenten

Vidareføre arbeidet utført som prosjektoppgåva hausten 2015 og saman med rettleiarane vidareutvikle problemstillingane der.

Eventuelt utvide og oppdatere litteraturstudiet omkring utslepp av LNG med brann (inkludert fysiske mekanismar som varmeoverføring, fordamping, dam-spreiiing og forbrenning).

Særleg aktuelle spørsmål er betre modellering av geometrien, modellering av utslepp og spreiiing av LNG og verknader av stråling og sot.

Bruke eit eigna program for å simulere utslepp, spreiiing og brann. Diskutere resultatata, inkludert modellar og moglege avvik mellom utrekningar og målingar.

Senest 14 dager etter utlevering av oppgaven skal kandidaten levere/sende instituttet en detaljert fremdrift- og eventuelt forsøksplan for oppgaven til evaluering og eventuelt diskusjon med faglig ansvarlig/veiledere. Detaljer ved eventuell utførelse av dataprogrammer skal avtales nærmere i samråd med faglig ansvarlig.

Besvarelsen redigeres mest mulig som en forskningsrapport med et sammendrag både på norsk og engelsk, konklusjon, litteraturliste, innholdsfortegnelse etc. Ved utarbeidelsen av teksten skal kandidaten legge vekt på å gjøre teksten oversiktlig og velskrevet. Med henblikk på lesning av besvarelsen er det viktig at de nødvendige henvisninger for korresponderende steder i tekst, tabeller og figurer anføres på begge steder. Ved bedømmelsen legges det stor vekt på at resultatene er grundig bearbeidet, at de oppstilles tabellarisk og/eller grafisk på en oversiktlig måte, og at de er diskutert utførlig.

Alle benyttede kilder, også muntlige opplysninger, skal oppgis på fullstendig måte. For tidsskrifter og bøker oppgis forfatter, tittel, årgang, sidetall og eventuelt figurnummer.

Det forutsettes at kandidaten tar initiativ til og holder nødvendig kontakt med faglærer og veileder(e). Kandidaten skal rette seg etter de reglementer og retningslinjer som gjelder ved alle (andre) fagmiljøer som kandidaten har kontakt med gjennom sin utførelse av oppgaven, samt etter eventuelle pålegg fra Institutt for energi- og prosesssteknikk.

Risikovurdering av kandidatens arbeid skal gjennomføres i henhold til instituttets prosedyrer. Risikovurderingen skal dokumenteres og inngå som del av besvarelsen. Hendelser relatert til kandidatens arbeid med uheldig innvirkning på helse, miljø eller sikkerhet, skal dokumenteres og inngå som en del av besvarelsen. Hvis dokumentasjonen på risikovurderingen utgjør veldig mange sider, leveres den fulle versjonen elektronisk til veileder og et utdrag inkluderes i besvarelsen.

I henhold til ”Utfyllende regler til studieforskriften for teknologistudiet/sivilingeniørstudiet” ved NTNU § 20, forbeholder instituttet seg retten til å benytte alle resultater og data til undervisnings- og forskningsformål, samt til fremtidige publikasjoner.

Besvarelsen leveres digitalt i DAIM. Et faglig sammendrag med oppgavens tittel, kandidatens navn, veileders navn, årstall, instituttnavn, og NTNUs logo og navn, leveres til instituttet som en separat pdf-fil. Etter avtale leveres besvarelse og evt. annet materiale til veileder i digitalt format.

- Arbeid i laboratorium (vannkraftlaboratoriet, strømningsmekanisk, varmeteknisk)
 Feltarbeid

NTNU, Institutt for energi- og prosesssteknikk, 13. januar 2015

Olav Bolland
Instituttleder

Ivar S. Ertesvåg
Faglig ansvarlig/veileder

Medveiledere/kontaktpersoner:
Kjell Erik Rian, ComputIT AS
Nils Inge Lilleheie, ComputIT AS
Rune N. Kleiveland, ComputIT AS

Preface

This master's thesis ends my fifth and final year of study at Mechanical Engineering under the department of Energy and Process Engineering at the Norwegian University of Science and Technology (NTNU). This thesis was written in cooperation with Computational Industry Technologies (ComputIT) AS.

I would like to thank my supervisors at ComputIT, Kjell Erik Rian, Rune N. Kleiveland and Nils Inge Lilleheie, for your motivation and continued support through the work on this thesis. Your dedication when answering all questions and helping with problems that have arisen during this year – big and small – have been much appreciated. To my supervisor at NTNU, Ivar S. Ertesvåg, for helpful feedback and guidance right up until the due date of this thesis, thank you. I would also like to thank all the people at ComputIT for being very welcoming, and for informative discussions of the simulations I would like to thank Bård Grimsmo.

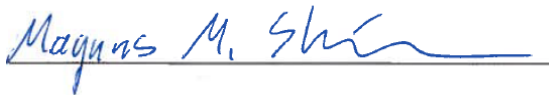
A special thank you goes to Céline (not Dion) for being so patient and understanding, and for your help in making me the best that I can be.

Finally, a very special thanks goes to my grandfather, Bjørn F. Magnussen, for your commitment and encouragement during all stages of work on this thesis.

*Anyone who stops learning is old,
whether at twenty or eighty.
Anyone who keeps learning stays young.
The greatest thing in life is to keep your mind young.*

— Henry Ford

Trondheim, June 9, 2016



Magnus Magnussen Skinnemoen

Abstract

This master's thesis continues the line of LNG related theses in cooperation with ComputIT AS. The Phoenix series large-scale LNG pool fire experiments have been simulated using the CFD software Kameleon FireEx (KFX) for validation purposes of the software to experimental data.

A number of simulations were performed, and the main investigations of the experiment – thermal radiation, pool spreading and flame morphology – have been compared to results from KFX, using a range of different simulation scenarios. Scenarios included simulating the LNG as either a liquid release or as a gaseous release of methane from a circular equivalent of the quasi-steady LNG pool area obtained on the experiment. Other variations included transient or constant release, where the transient release was based on an approximated flow rate from the experiment, and the constant release was based on the average flow rate over the duration of the experiment. Due to limitations in the pool model in KFX, the liquid releases were simulated on a flat ground instead of on a pool of water, with various heat transfer coefficients to account for the heat transfer between the water and the LNG.

The radiative heat fluxes from the simulations compared to experimental values were initially low by factors between two and four, regardless of simulation scenario. The soot model was investigated, and found to give an excess of relatively cold soot outside of the flame, acting as a radiation screen, thus reducing the thermal radiation from the fire to the surroundings. The soot model was modified, and subsequent simulations produced very comparable values for the radiative heat fluxes for the majority of simulation scenarios.

For all liquid, transient simulations, the LNG pool spread much faster than in the experiment, and only the simulations with adiabatic conditions between the LNG and ground reached the same maximum area as the experiment. All simulations with non-adiabatic conditions had a maximum pool area below that of the experiment. As a result, it was concluded that the LNG vaporized too quickly, and consequently the duration of the fire was about 250 s shorter in the simulations than in the experiment. As a consequence of the high vaporization rate in the simulations, the flame grew to heights far above the experiment, and at some instances the flame in the simulations exceeded the flame height in the experiment of over 100 m.

A new, simple model for LNG spreading through water was introduced, and initial computations in MATLAB produced highly promising results.

Sammendrag

Denne masteroppgaven fortsetter arbeidet med LNG-relaterte oppgaver i samarbeid med ComputIT AS. Eksperimentene med LNG-pølbrann fra Phoenix-serien ble brukt for validering og sammenlikning av CFD-programvaren Kameleon FireEx (KFX) mot eksperimentelle data.

Et stort antall simuleringer ble foretatt, og de tre hovedpunktene undersøkt i eksperimentet – varmestråling, pølspredning og morfologi – har blitt sammenliknet med resultater fra KFX, gjennom en rekke forskjellige simuleringsscenarier. Forskjellige scenario inkluderte oppsett av simuleringene som enten et utslipp av LNG, eller som avdampet metan fra et sirkulært område tilsvarende det kvasi-stasjonære pølarealet oppnådd i eksperimentet. Andre variasjoner inkluderte transient eller konstant masseutslipp, der det transiente utslippet ble basert på en tilnærmet massestrøm fra eksperimentet, og det konstante utslippet ble basert på en gjennomsnittlig massestrøm over hele utslippet. Grunnet begrensninger i pølspredningsmodellen i KFX, ble de flytende utslippene simulert som et utslipp på bar bakke, i motsetning til på en vanndam, med forskjellige varmeovergangstall for å ta høyde for varmeutvekslingen mellom vann og LNG.

Strålingsfluksene fra simuleringene sammenliknet med eksperimentalverdier var innledningsvis for lave med en faktor mellom to og fire, uavhengig av simuleringsscenario. Sotmodellen ble undersøkt, og det ble funnet ut at den ga for store mengder relativt kald sot utenfor flammen som fungerte som sotskjerming, og dermed reduserte varmestrålingen fra flammen til omgivelsene. Sotmodellen ble modifisert, og påfølgende simuleringer ga meget sammenliknbare resultater for majoriteten av simuleringsscenarioene.

For de flytende, transiente simuleringene spredde LNG-pølen seg mye raskere enn i eksperimentet, og kun simuleringene med adiabatisk forhold mellom LNG-et og bakken ga et maksimalt pølareal på nivå med eksperimentet. Alle simuleringene med ikke-adiabatisk forhold hadde et lavere maksimalt pølareal enn i eksperimentet. Grunnet dette, ble det konkludert med for høy fordamping av LNG, og følgelig ble varigheten til brannen omtrent 250 s kortere i simuleringene enn i eksperimentet. Som følge av den høye fordampingsraten ble flammehøyden i simuleringene langt høyere enn i eksperimentet, og ble i enkelte tilfeller over 100 m høyere.

En ny, relativt enkel modell for LNG-spredning gjennom vann ble introdusert, og innledende beregninger i MATLAB ga svært lovende resultater.

Contents

Preface	v
Abstract	vii
Sammendrag	ix
Nomenclature	xiii
1 Introduction	1
1.1 Motivation	1
1.2 Limitations and restrictions	1
1.3 Report outline	2
2 Theory and Physical Models	3
2.1 General Equations	3
2.2 Turbulent Flows	6
2.3 Heat Transfer	11
2.4 Radiation	12
2.5 Combustion	18
2.6 KFX Models and Numerics	27
3 The Phoenix Series Large Scale LNG Pool Fire Experiments	35
3.1 Experimental Setup	35
3.2 Pool Spreading and Area	36
3.3 Radiative Heat Flux and Surface Emissive Power	37
3.4 Uncertainties and Errors	38
3.5 Key Results	39
4 Simulations - Radiative Heat Fluxes	41
4.1 Initial Work and Basis for the Thesis	41
4.2 Simulation Setup	41
4.3 Numerical Solvers, Convergence and Grid Resolution	43
4.4 Initial Simulations and Radiative Heat Fluxes	44

4.5	Radiative Heat Fluxes with Modified Soot Model	52
5	Simulations - Pool Spreading and Area	57
5.1	LNG Pool Area	57
5.2	Mean Pool Depth	58
5.3	Cross-Sectional Pool Depth	59
5.4	No Ignition, Constant Fuel Regression Rate	62
5.5	Effect of Surrounding Water Pool	64
6	Simulations - Flame Morphology	67
6.1	Flame Centroid and Maximum Height	67
6.2	Flame Anchoring	71
7	Non-KFX Analysis of Pool Spreading	73
7.1	New Model for Oil Pool Spreading Through Water	73
7.2	Calculations Based on the Phoenix Experiment Data	79
7.3	Comparison to Other Models	82
8	Discussion	85
9	Conclusions and Further Work	91
9.1	Conclusions	91
9.2	Recommendations for Further Work	92
	Bibliography	93
A	Appendix A	97
B	Appendix B - Videos and simulations	105
B.1	Links to Videos of the SNL Phoenix LNG Experiments	105
B.2	Animations of KFX simulations	106
C	Appendix C	107
C.1	MATLAB Codes and Scripts	107

Nomenclature

Due to the fact that there are a limited number of letters in the combined Greek and Latin alphabets, and seemingly endless number of quantities and variables in need of a symbol, some of these symbols will have different meanings depending on context. However, to the educated reader, what is meant will be clear when reading.

Abbreviations

CAD	Computer aided design
CFD	Computational fluid dynamics
DNS	Direct numerical simulation
DTM	Discrete transfer model
EDC	Eddy Dissipation Concept
KFX	Kameleon FireEx
LES	Large eddy simulation
LHS	Left-hand side (of equation)
ODE	Ordinary differential equation
RHS	Right-hand side (of equation)
RTE	Radiative transfer equation
SEP	Surface emissive power
SNL	Sandia National Laboratories
TKE	Turbulence kinetic energy

Greek symbols

α	Thermal diffusivity	$[\text{m}^2/\text{s}]$
α	Absorptance	$[-]$
γ	Intermittency factor in the EDC	$[-]$
δ_{ij}	Kronecker delta	$[-]$
δ_L	Characteristic flame thickness	$[\text{m}]$
ϵ	Emittance	$[-]$
ε	Dissipation rate of mean turbulence energy	$[\text{m}^2/\text{s}^3]$
η	Wave number of electromagnetic waves	$[1/\text{m}]$
η	Kolmogorov length scale	$[\text{m}]$
θ	Time scale for large eddies ($= \ell'/u'$)	$[\text{s}]$
κ_η	Absorption coefficient	$[1/\text{m}]$
λ	Wavelength of electromagnetic waves	$[\text{m}]$
μ	Dynamic viscosity	$[\text{Ns}/\text{m}^2]$
ν	Frequency of electromagnetic waves	$[\text{Hz}=1/\text{s}]$
ν	Kinematic viscosity	$[\text{m}^2/\text{s}]$
$\xi_{i,j}$	Mass fraction of element j in species i	$[(\text{kg})_j/(\text{kg})_i]$
ρ	Density	$[\text{kg}/\text{m}^3]$
ρ	Reflectance	$[-]$
ρ_k	Mass concentration/density of species k	$[(\text{kg})_k/\text{m}^3]$
σ	Stefan-Boltzmann constant	$[\text{W}/\text{m}^2\text{K}^4]$
σ_ϕ	Turbulent Prandtl-Schmidt number for quantity ϕ	$[-]$
τ	Shear stress	$[\text{N}/\text{m}^2]$
τ	Kolmogorov timescale	$[\text{s}]$
τ	Transmittance	$[-]$
τ_c	Chemical time scale for reactions	$[\text{s}]$
τ_{ij}	Viscous stress tensor	$[\text{N}/\text{m}^2]$
ϕ	General quantity	$[-]$
χ	Reaction fraction of the fine structures in the EDC	$[-]$
ω	(Angular) Frequency	$[1/\text{s}]$

Latin symbols

A	Area	$[\text{m}^2]$
A_k	Atomic mass of element k	$[\text{kg}]$
c_0	Speed of light in vacuum ($= 2.998 \times 10^8 \text{ m/s}$)	$[\text{m/s}]$
c_p	Specific heat capacity	$[\text{J/kgK}]$
C_{Di}	Model constant in the EDC	$[-]$
C_2	Planck's second constant ($= 0.01439 \text{ mK}$)	$[\text{mK}]$
\mathcal{D}	Mass diffusivity	$[\text{m}^2/\text{s}]$
Da	Dahmköler number for reactive system	$[-]$
d	Diameter	$[\text{m}]$
E	Emissive power	$[\text{W}/\text{m}^2]$
$f_{k,i}$	Acceleration of species k due to external force in direction of x_i	$[\text{m}/\text{s}^2]$
g	Gravitational constant	$[\text{m}/\text{s}^2]$
G	Irradiation	$[\text{W}/\text{m}^2]$
h	Convection coefficient	$[\text{W}/\text{m}^2\text{K}]$
h	Planck's constant ($= 6.626 \times 10^{-34} \text{ Js}$)	$[\text{Js}]$
h_k	Specific enthalpy of species k	$[\text{kJ}/\text{kg}]$
h_{fg}	Latent heat of vaporization	$[\text{kJ}/\text{kg}]$
H_R	Heat of reaction	$[\text{J}/(\text{kg fuel})]$
I	Radiation intensity	$[\text{W}/\text{m}^2 \cdot \text{sr}]$
J	Radiosity	$[\text{W}/\text{m}^2]$
k	Boltzmann constant ($= 1.3807 \times 10^{-23} \text{ J/K}$)	$[\text{J}/\text{K}]$
k	Turbulence kinetic energy ($= \frac{1}{2} \overline{u_i u_i}$)	$[\text{m}^2/\text{s}^2]$
k	Thermal conductivity	$[\text{W}/\text{mK}]$
ℓ'	Length scale for large eddies	$[\text{m}]$
m''	Mass per unit area	$[\text{kg}/\text{m}^2]$
\dot{m}	Mass flow	$[\text{kg}/\text{s}]$
n	Refractive index of a medium	$[-]$
P_k	Production, rate of production of k	$[\text{m}^2/\text{s}^3]$

q''	Heat flux	[W/m ²]
q	Heat transfer rate	[W]
q_i	Heat flux per area in direction of x_i	[W/m ²]
q^*	Volumetric heat generation in the EDC	[W/m ³]
\dot{Q}	Source term in the energy balance equation	[W/m ³]
r	Mass of oxidant reacting with 1 kg fuel	[kg]
\mathcal{R}	Universal gas constant (= 8.3144598 J/mol K)	[J/mol K]
R_k	Rate of reaction for component k	[(kg) _k /(m ³ s)]
Re_x	Reynolds number based on length x	[-]
Re_T	Turbulent Reynolds number (= $k^2/\nu\varepsilon$)	[-]
\bar{S}_{ij}	Mean rate-of-strain tensor ($\frac{1}{2}\partial\bar{u}_i/\partial x_j + \partial\bar{u}_j/\partial x_i$)	[1/s]
T	Temperature	[K]
u	x component of velocity	[m/s]
u_η	Kolmogorov velocity scale	[m/s]
u'	Time scale for large eddies	[m/s]
u_L	Spreading velocity for premixed laminar flames	[m/s]
v	y component of velocity	[m/s]
$V_{k,i}$	Speed of diffusion of species k in direction of x_i	[m/s]
w	z component of velocity	[m/s]
w'	Energy transfer in the cascade model	[m ² /s ³]
Y_k	Mass fraction of species k in mixture (usually air)	[(kg) _k /kg]

Superscripts

$\dot{\phi}$	Time derivative of ϕ /per unit time
'	Fluctuation from mean value (on a time/Reynolds basis)
"	Fluctuation from mean value (on a mass/Favre basis)
*	Fine structure region in the EDC
\rightarrow	Vector in non-Einstein notation
$\tilde{\phi}$	Favre averaged quantity ϕ
$\bar{\phi}$	Reynolds averaged quantity ϕ

Subscripts

ϕ	Property of the quantity ϕ /per unit ϕ
a	Air
b	Blackbody property
c	Combustion (of species or quantity)
C	Carbon
f	Formation (of species or quantity)
F	Flame
fu	Fuel
i, j, k	Vector indication in the Einstein notation
l	Liquid
nuc	Nucleus
ox	Oxidant
p	Particle
pr	Combustion product(s)
t	Turbulent/property of the turbulence
s, soot	Soot
w	Wall
x, y, z	x -, y - or z -direction

1 Introduction

The demand for energy seems to be ever-increasing. With a rapidly rising world population and standard of living in many countries, the need for steady and reliable energy sources shows no signs of slowing down any time soon. Liquefied natural gas (LNG) has been proposed as being a partial solution to this problem as LNG is capable of transferring and storing large amounts of energy in places and situations regular gas pipelines and tanks cannot, with countries such as Japan and the US being among the forerunners in this field.

1.1 Motivation

More and more natural gas is being transported as LNG. This liquid form of natural gas is made in a process called cryogenic cooling. Both this process, and transport and storage of LNG in general, is potentially highly hazardous, due to the extremely cold nature of LNG and the highly flammable hydrocarbons present. Governments and the industry have great interest in safeguarding people, equipment and assets against accident. In the case of an accident – say, a leakage and spreading of LNG from a ship or storage tank – it would be of great interest to be able to model, predict and make calculations of LNG spreading under realistic conditions, and possible explosions and fires as a consequence.

Sandia National Laboratories, based in New Mexico, USA, conducted two large-scale LNG pool fire on water experiments in 2009 to improve the understanding of various aspects related to LNG safety, including radiative heat fluxes, pool spreading, flame size and burn rate [2, 3]. As experiments on expected scales in the case of an accident are extremely costly and environmentally unfriendly, the use of computer simulation programs such to investigate various accident scenarios are of considerable interest.

1.2 Limitations and restrictions

The aim of this thesis is to validate and compare the computational fluid dynamics (CFD) software Kameleon FireEx (KFX) developed by ComputIT AS against the

Phoenix large-scale LNG experiments. The larger of the two experiments, named LNG Test 2, was chosen for the simulations performed in KFX. As a continuation of previous work [31], some of the theory, results and comments are repeated here, to ensure that this thesis can be read separately.

Due to limitations on the KFX software, the majority of the simulations performed were simulated as either a liquid methane release on flat ground with a surrounding water ring of water to emulate the water pool, or as a gaseous release of methane from a circular enclosure. The speed and direction of wind were treated as constant and, unless specified, a simple CAD model of the test site was used for the simulations. In the case of a liquid release, the heat transfer coefficient to the ground (in $\text{W}/\text{m}^2\text{K}$) is assumed constant, either as zero or as a constant value based on discussion and knowledge of supervisors.

1.3 Report outline

Ch. 2 describes the most important underlying physical theory and numerical methods included in KFX. Ch. 3 summarizes the SNL Phoenix large scale LNG tests and gives information necessary for understanding the simulation setup and key data for comparison to the CFD simulations. Chs. 4, 5 and 6 details and discusses the various simulations performed and compared to the Phoenix experiment. Ch. 7 introduces a new, simple model for LNG spreading through water and discusses some computations performed in MATLAB with this model and compares to data from the Phoenix experiment. This is followed by a summarizing discussion in Ch. 8 and conclusion and recommendation for further work in Ch 9.

Appendix A gives various figures deemed too big or unfit for the main part of the report. Appendix B contains links to some descriptive and informative videos from the Phoenix experiment, as well as animations illustrating the transient behavior of some of the KFX simulations. Various computer scripts are given in Appendix C.

2 Theory and Physical Models

This chapter will present some of the physical aspects related to turbulent flows and combustion. Parts of this chapter is meant as orientation to readers not fully educated on subjects such as turbulence and heat transfer (Secs. 2.1 - 2.3), and other parts are used to present some of the underlying models and numerical schemes used in KFX to perform the calculations.

2.1 General Equations

2.1.1 Conservation of Energy, Mass and Momentum

The governing principles in fluid mechanics and dynamics are the conservation laws for energy, mass and momentum.

2.1.1.1 Conservation of Energy

The equation for conservation of energy in differential form can be written [6, p. 207]

$$\frac{\partial}{\partial t} (\rho e_{\text{tot}}) + \frac{\partial}{\partial x_i} (\rho e_{\text{tot}} u_i) = \rho f_i u_i + \frac{\partial}{\partial x_i} (\tau_{ij} u_j) - \frac{\partial}{\partial x_i} (p u_i) - \frac{\partial q_i}{\partial x_i} + \dot{Q}, \quad (2.1)$$

where $e_{\text{tot}} = e + \frac{1}{2} u_i u_i$ is the total energy in the system, and it is the sum of internal and kinetic energy. Additionally, Eq. (2.1) includes terms for work, energy exchange and heat transfer on a fluid particle. The first term on the RHS is the rate of work done a fluid particle by external forces (e.g. gravitation), and the second term on the RHS is total rate of work done on a fluid particle by surface stresses. \dot{Q} is an source term which accounts for, among others, net incident radiation. q_i is the thermal energy flux to and from the fluid particle, and can be divided into

$$q_i = q_{c,i} + q_{d,i} + q_{D,i}, \quad (2.2)$$

where the different terms are the energy fluxes in direction x_i due to conduction, species diffusion and concentration gradients, respectively. The energy flux due to conduction can be expressed by Fourier's law, Eq. (2.41). The energy flux due to

diffusion occurs because of molecular diffusion of species with different enthalpies. For species k , this can be expressed by

$$q_{d,i} = \sum_{j=k}^N h_k j_{k,i}, \quad (2.3)$$

where $j_{k,i}$ follows from Eq. (2.10) and N is the number of species present. The final term, called the Dufour effect, usually small compared to the other two, and is often neglected [9, p. 43].

2.1.1.2 Conservation of Mass and Momentum

When ignoring nuclear reactions and relativistic effects¹, mass can neither be created or destroyed – mass is always conserved. The equation representing conservation of mass in differential form is called the *continuity equation* and can, for a single phase flow, be written

$$\frac{\partial \rho}{\partial t} + \frac{\partial}{\partial x_i} (\rho u_i) = 0. \quad (2.4)$$

By applying Favre averaging (see Sec. 2.1.3), Eq. (2.4) is written

$$\frac{\partial \bar{\rho}}{\partial t} + \frac{\partial}{\partial x_i} (\bar{\rho} \tilde{u}_i) = 0. \quad (2.5)$$

Momentum is defined as the mass of an object multiplied with the velocity of said object. Similarly, momentum within a closed domain can neither be created or destroyed, but only changed due to the effect of forces, as can be described by Newton's laws of motion. The equation for conservation of momentum can be written

$$\frac{\partial}{\partial t} (\rho u_i) + \frac{\partial}{\partial x_j} (\rho u_i u_j) = -\frac{\partial p}{\partial x_i} + \frac{\partial \tau_{ij}}{\partial x_j} + \rho f_i, \quad (2.6)$$

where, for a Newtonian fluid, the viscous stress tensor τ_{ij} is

$$\tau_{ij} = \mu \left(\frac{\partial u_i}{\partial x_j} + \frac{\partial u_j}{\partial x_i} \right) + \left(\mu_v - \frac{2}{3}\mu \right) \frac{\partial u_k}{\partial x_k}. \quad (2.7)$$

The quantity μ_v is called the *coefficient of bulk viscosity*. The *Stokes assumption* gives $\mu_v = 0$, and is found to be accurate in many situations [12, pp. 113-114]. The LHS of Eq. (2.6) describes the acceleration of a fluid particle, and is equal to the surface forces and body forces experienced by the fluid particle on the RHS [30, p. 16]. The body forces f_i in Eqs. (2.1) and (2.6) are typically limited to the gravitational force.

¹Physical phenomena observed when the speed of bodies or particles approach the speed of light.

2.1.2 Transport Equations

The transport of a general scalar quantity ϕ can be written

$$\underbrace{\frac{\partial}{\partial t}(\rho\phi)}_{\text{Local derivative}} + \underbrace{\frac{\partial}{\partial x_j}(\rho\phi u_j)}_{\text{Advection}} = \underbrace{\frac{\partial}{\partial x_j}(-j_{\phi,j})}_{\text{Diffusion}} + \underbrace{S_\phi}_{\text{Source term}}, \quad (2.8)$$

where Fick's law of diffusion is $-j_{\phi,j} = \Gamma_\phi \frac{\partial \phi}{\partial x_j}$, and Γ_ϕ is some diffusion coefficient related to ϕ in the direction of x_j . S_ϕ is a source term and accounts for any creation or destruction of ϕ . In words, this can be stated as [36, p. 5]:

$$\left[\begin{array}{c} \text{Rate of change} \\ \text{of } \phi \text{ in the} \\ \text{control volume} \\ \text{with respect} \\ \text{to time} \end{array} \right] = \left[\begin{array}{c} \text{Net flux of} \\ \phi \text{ due to} \\ \text{convection into} \\ \text{the control} \\ \text{volume} \end{array} \right] + \left[\begin{array}{c} \text{Net flux of} \\ \phi \text{ due to} \\ \text{diffusion into} \\ \text{the control} \\ \text{volume} \end{array} \right] + \left[\begin{array}{c} \text{Net rate of} \\ \text{creation of} \\ \phi \text{ inside} \\ \text{the control} \\ \text{volume} \end{array} \right].$$

If the fluid is a mixture of two or more species, and by introducing the species mass fraction for species k , $Y_k = \rho_k/\rho$, Eq. (2.8) can be written

$$\frac{\partial}{\partial t}(\rho Y_k) + \frac{\partial}{\partial x_j}(\rho Y_k u_j) = \frac{\partial}{\partial x_j}(-j_{k,j}) + R_k, \quad (2.9)$$

where R_k is the rate of reaction (production) of species k . Here, $-j_{k,j}$ can be written as

$$-j_{k,j} = -\rho_k V_{k,j} = -\rho Y_k V_{k,j} = \rho \mathcal{D} \frac{\partial Y_k}{\partial x_j}, \quad (2.10)$$

where \mathcal{D} is a diffusion coefficient, and will vary from material to material.

2.1.3 Favre Averaging

In fluid flow, Reynolds averaging, where a field variable is decomposed into a mean part and a fluctuating part, is widely used, as described in Sec. 2.2.1. However, in flows with variable density, such as combustion, *Favre averaging* is conveniently used. A Favre averaged quantity is defined as [6, p. 225]

$$\phi(t) = \tilde{\phi} + \phi''(t), \quad (2.11)$$

where

$$\tilde{\phi} = \frac{\overline{\rho\phi}}{\bar{\rho}}. \quad (2.12)$$

That is, the density is included into the averaging of the mean part. Note that $\overline{\rho\phi} \neq \bar{\rho}\bar{\phi}$, unless the density is constant. If the density is constant, then Eq. (2.11) is

$$\phi = \frac{\overline{\rho\phi}}{\bar{\rho}} + \phi'' = \frac{\bar{\rho}\bar{\phi}}{\bar{\rho}} + \phi'' = \bar{\phi} + \phi'', \quad (2.13)$$

which is equal to the Reynolds decomposition.

2.2 Turbulent Flows

For sufficiently large Reynolds numbers, $Re_L = (\rho UL)/\mu$, fluid flows go from being laminar and become turbulent. Virtually all naturally occurring flows are turbulent, and these flows have to be described and modelled differently from laminar flows. Many different characteristic scales and turbulence models exist, some of which will be presented in brief here.

2.2.1 Fundamentals of Turbulent Motion

A fundamental part of turbulence modelling is the *Reynolds decomposition* of the velocity vector u_i into its mean part \bar{u}_i and fluctuating part u'_i :

$$u_i(t) = \bar{u}_i + u'_i(t) \quad (2.14)$$

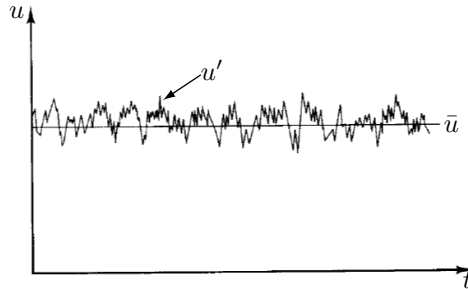


Figure 2.1: Typical point measurement of velocity in turbulent flow. Adapted from Versteeg and Malalasekera [36, p. 42].

The covariance of the velocity fluctuations multiplied with the density are called *Reynolds stresses*, or the *Reynolds stress tensor*, and it is

$$\overline{\rho u'_i u'_j} = \rho \begin{bmatrix} \overline{u_1'^2} & \overline{u_1' u_2'} & \overline{u_1' u_3'} \\ \overline{u_1' u_2'} & \overline{u_2'^2} & \overline{u_2' u_3'} \\ \overline{u_1' u_3'} & \overline{u_2' u_3'} & \overline{u_3'^2} \end{bmatrix}. \quad (2.15)$$

One of the most important characteristics of turbulent flows, is the *turbulence kinetic energy*, k , defined to be half the trace of the Reynolds stress tensor [30, p. 88], or the mean of the turbulence normal stresses:

$$k = \frac{1}{2} \overline{u'_i u'_i} = \frac{1}{2} \left(\overline{(u'_1)^2} + \overline{(u'_2)^2} + \overline{(u'_3)^2} \right). \quad (2.16)$$

The turbulence kinetic energy (TKE) k , can be inserted into a generic transport equation (see Eq. (2.8)) to produce the full form of the TKE transport equation. With constant ρ and ν , we get:

$$\begin{aligned}
 & \overbrace{\frac{\partial k}{\partial t} + \bar{u}_j \frac{\partial k}{\partial x_j}}^{\text{Material derivative } Dk/Dt} = \\
 & \underbrace{\frac{\partial k}{\partial t}}_{\text{Local derivative}} + \underbrace{\bar{u}_j \frac{\partial k}{\partial x_j}}_{\text{Advection}} = \\
 & - \underbrace{\frac{1}{\rho} \frac{\partial \overline{u'_i p'}}{\partial x_i}}_{\text{Pressure diffusion}} - \underbrace{\frac{1}{2} \frac{\partial \overline{u'_j u'_j u'_i}}{\partial x_i}}_{\text{Turbulent transport } \mathcal{T}} + \underbrace{\nu \frac{\partial^2 k}{\partial x_j \partial x_j}}_{\text{Molecular viscous transport}} - \underbrace{\overline{u'_i u'_j} \frac{\partial \bar{u}_i}{\partial x_j}}_{\text{Production } P_k} - \underbrace{\nu \frac{\partial \overline{u'_i}}{\partial x_j} \frac{\partial \overline{u'_i}}{\partial x_j}}_{\text{Dissipation } \varepsilon} - \underbrace{\frac{g}{\rho_o} \overline{\rho' u'_i} \delta_{i3}}_{\text{Buoyancy flux } b}. \quad (2.17)
 \end{aligned}$$

The last term, the buoyancy term, is often omitted from this equation, but can be significant in combination with combustion, where the density can vary quite significantly throughout the domain. The second-to-last term, the dissipation ε , is the transfer of mechanical energy as heat (thermal energy) to the surroundings. It is defined as it stands in the equation. Usually, these forms of equations are of little use in turbulence calculations and *model equations* are instead introduced for the various turbulence models. A large number of turbulence models exist, all with different strengths and weaknesses. The most widely used model, incorporated in most commercial CFD codes², is the $k - \varepsilon$ model [30, p. 373], which will be discussed in Sec. 2.2.3.

2.2.2 Scales of Turbulent Motion

In turbulent flows, the scales range in size from the width of the flow and the size of the largest eddies, to much smaller scales. The smallest scales, and perhaps most important, are called the *Kolmogorov microscales*, or just *Kolmogorov scales*. These scales are descriptive of the characteristic sizes, velocities and time scales of the smallest eddies by the viscosity and dissipation, and are as such:

$$\text{Length scale: } \eta \equiv (\nu^3/\varepsilon)^{1/4}, \quad (2.18a)$$

$$\text{Velocity scale: } u_\eta \equiv (\varepsilon\nu)^{1/4}, \quad (2.18b)$$

$$\text{Time scale: } \tau \equiv (\nu/\varepsilon)^{1/2}. \quad (2.18c)$$

From these, the dissipation rate is given by $\varepsilon = \nu(u_\eta/\eta)^2 = \nu/\tau^2$. Together, they produce a Kolmogorov Reynolds number, $\text{Re}_\eta = (\eta u_\eta/\nu)$, which is approximately unity [30, p. 185]. There are many other scales of turbulent motion, some of which are directly tied to Eq. (2.18), some of which are not tied to them but developed

²Among them KFX [35, p. 208].

in similar fashion and some which are unrelated.

2.2.3 The General $k - \varepsilon$ Model

The $k - \varepsilon$ model is a popular turbulence model, belonging to the class of *two-equation models*, meaning that it solves model transport equations for two turbulence quantities – k and ε in this case. From k and ε three characteristic scales can be formed: a length scale ($L = k^{3/2}/\varepsilon$), a time scale ($\tau = k/\varepsilon$) and a dimensional quantity ($\nu_t = k^2/\varepsilon$).

The $k - \varepsilon$ model includes the specification the turbulent viscosity as

$$\nu_t = C_\mu \frac{k^2}{\varepsilon}, \quad (2.19)$$

where C_μ is one of five model constants, and the *turbulent viscosity hypothesis*, which states that the so-called deviatoric Reynolds stress is proportional to the mean rate of strain, that is

$$-\overline{\rho u'_i u'_j} + \frac{2}{3} \rho k \delta_{ij} = \rho \nu_t \left(\frac{\partial \bar{u}_i}{\partial x_j} + \frac{\partial \bar{u}_j}{\partial x_i} \right) = 2\rho \nu_t \bar{S}_{ij}, \quad (2.20)$$

where \bar{S}_{ij} is the mean rate-of-strain tensor and δ_{ij} is the Kronecker delta. The turbulent viscosity ν_t is a flow property, and not a material property as the kinematic viscosity ν . The *effective viscosity* can be written as $\nu_{\text{eff}} = \nu + \nu_t$.

By assuming constant density, the model equations for k and ε in the standard $k - \varepsilon$ model can be written [30, pp. 372–375]

$$\frac{\partial k}{\partial t} + \bar{u}_j \frac{\partial k}{\partial x_j} = \frac{\partial}{\partial x_j} \left(\frac{\nu_t}{\sigma_k} \frac{\partial k}{\partial x_j} \right) + P_k - \varepsilon, \quad (2.21)$$

and,

$$\frac{\partial \varepsilon}{\partial t} + \bar{u}_j \frac{\partial \varepsilon}{\partial x_j} = \frac{\partial}{\partial x_j} \left(\frac{\nu_t}{\sigma_\varepsilon} \frac{\partial \varepsilon}{\partial x_j} \right) + C_{\varepsilon 1} \frac{P_k \varepsilon}{k} - C_{\varepsilon 2} \frac{\varepsilon^2}{k}, \quad (2.22)$$

respectively, where the turbulence production P_k and dissipation ε are defined in Eq. (2.16). The standard model constants in the $k - \varepsilon$ model are, from Launder and Spalding [13]:

$$\sigma_k = 1.0, \quad \sigma_\varepsilon = 1.3, \quad C_{\varepsilon 1} = 1.44, \quad C_{\varepsilon 2} = 1.44, \quad \text{and} \quad C_\mu = 0.09, \quad (2.23)$$

where σ_k and σ_ε are the turbulent Prandtl numbers for k and ε , respectively.

2.2.4 Extended $k - \varepsilon$ Model

KFX uses a Favre-averaged, extended version of the $k - \varepsilon$ model (Sec. 2.2.3) for the turbulence. The continuity, energy balance, mass balance and momentum

equations are all modified and given on a Favre averaged basis. The turbulence kinetic energy k is modified from Eq. (2.16) to be

$$k = \frac{1}{2} \widetilde{u_i'' u_i''}. \quad (2.24)$$

The momentum equation, Eq. (2.6), is modified to

$$\frac{\partial(\bar{\rho} \widetilde{u}_i)}{\partial t} + \frac{\partial(\bar{\rho} \widetilde{u}_i \widetilde{u}_j)}{\partial x_j} = -\frac{\partial \bar{p}}{\partial x_i} + \frac{\partial}{\partial x_j} \left(\bar{\tau}_{ij} - \bar{\rho} \widetilde{u_i'' u_j''} \right) + \bar{\rho} \widetilde{f}_i, \quad (2.25)$$

where the mass averaged Reynolds stresses, $-\bar{\rho} \widetilde{u_i'' u_j''}$, are modeled as

$$-\bar{\rho} \widetilde{u_i'' u_j''} = -\mu_t \left(\frac{\partial \widetilde{u}_i}{\partial x_j} + \frac{\partial \widetilde{u}_j}{\partial x_i} \right) - \frac{2}{3} \left(\bar{\rho} k + \mu_t \frac{\partial \widetilde{u}_l}{\partial x_l} \right) \delta_{ij}. \quad (2.26)$$

This is then inserted into the turbulence production term to give

$$\bar{\rho} P_k = -\mu_t \left(\frac{\partial \widetilde{u}_i}{\partial x_j} + \frac{\partial \widetilde{u}_j}{\partial x_i} \right) \frac{\partial \widetilde{u}_i}{\partial x_j} - \frac{2}{3} \left(\bar{\rho} k + \mu_t \frac{\partial \widetilde{u}_l}{\partial x_l} \right) \frac{\partial \widetilde{u}_i}{\partial x_j}. \quad (2.27)$$

The model equations for k and ε , Eqs. (2.21) and (2.22), in the modified $k - \varepsilon$ model are written as

$$\frac{\partial(\bar{\rho} k)}{\partial t} + \frac{\partial(\bar{\rho} \widetilde{u}_j k)}{\partial x_j} = \frac{\partial}{\partial x_j} \left(\left(\mu + \frac{\mu_t}{\sigma_k} \right) \frac{\partial k}{\partial x_j} \right) + \bar{\rho} P_k - \bar{\rho} \varepsilon + B, \quad (2.28)$$

and,

$$\begin{aligned} \frac{\partial(\bar{\rho} \varepsilon)}{\partial t} + \frac{\partial(\bar{\rho} \widetilde{u}_j \varepsilon)}{\partial x_j} = \\ \frac{\partial}{\partial x_j} \left(\left(\mu + \frac{\mu_t}{\sigma_\varepsilon} \right) \frac{\partial \varepsilon}{\partial x_j} \right) + C_{\varepsilon 1} f_{\varepsilon 1} \bar{\rho} \frac{P_k \varepsilon}{k} - C_{\varepsilon 2} f_{\varepsilon 2} \bar{\rho} \frac{\varepsilon^2}{k} + C_{\varepsilon 1} C_{\varepsilon 3} \frac{\varepsilon}{k} B, \end{aligned} \quad (2.29)$$

respectively. Two additional effects compared to the standard $k - \varepsilon$ have been included: low-Reynolds number effects and buoyancy effects. f_1 and f_2 are the low-Reynolds number corrections terms, and the final terms in Eqs. (2.28) and (2.29) accounts for the buoyancy. $f_{\varepsilon 1}$ and $f_{\varepsilon 2}$ are by Jones and Launder [11] given as

$$f_{\varepsilon 1} = 1.0 \quad (2.30)$$

and

$$f_{\varepsilon 2} = 1.0 - 0.3 \exp(-\text{Re}_t^2), \quad (2.31)$$

where $\text{Re}_t = \rho k^2 / \mu \varepsilon$ is the turbulence Reynolds number. Additionally, the turbulent viscosity, Eq. (2.19), is modified to

$$\mu_t = C_\mu f_\mu \bar{\rho} \frac{k^2}{\varepsilon}, \quad (2.32)$$

where f_μ is a low-Reynolds number viscosity correction and is modelled as

$$f_\mu = \exp\left(-\frac{2.5}{1 + \text{Re}_t/50}\right). \quad (2.33)$$

2.2.5 Mean Scalar Equation and Reynolds Flux Models

Similarly to the decomposition of the turbulent velocity, Eq. (2.14), a fluctuating scalar $\phi(x_i, t)$ can be decomposed as

$$\phi(x_i, t) = \bar{\phi} + \phi'(x_i, t), \quad (2.34)$$

or Favre averaged as

$$\phi(x_i, t) = \tilde{\phi} + \phi''(x_i, t). \quad (2.35)$$

The transport of a fluctuating scalar variable follows from Eq. (2.8). For the scalars mass fraction and enthalpy, we can write [6]:

$$\begin{aligned} \frac{\partial}{\partial t} (\bar{\rho} \tilde{Y}_k) + \frac{\partial}{\partial x_j} (\bar{\rho} \tilde{Y}_k \tilde{u}_j) = \\ \frac{\partial}{\partial x_j} \left(\bar{\rho} \mathcal{D} \frac{\partial \tilde{Y}_k}{\partial x_j} \right) - \frac{\partial}{\partial x_j} (\overline{\rho u_j'' Y_k''}) + \bar{R}_k + \frac{\partial}{\partial x_j} \left(\overline{\mathcal{D} \rho \frac{\partial Y_k''}{\partial x_j}} \right), \end{aligned} \quad (2.36)$$

and

$$\frac{\partial}{\partial t} (\bar{\rho} \tilde{h}) + \frac{\partial}{\partial x_j} (\bar{\rho} \tilde{h} \tilde{u}_j) = \frac{\partial}{\partial x_j} \left(\bar{\rho} \alpha \frac{\partial \tilde{h}}{\partial x_j} - \overline{\rho u_j'' h''} \right) + \bar{S}_h. \quad (2.37)$$

The scalar Favre flux can be written $\overline{\rho u_j'' \phi''} = \overline{\tilde{\rho} u_j'' \phi''}$. By applying the *gradient-diffusion hypothesis* [30, pp. 92–93], the flux of a scalar can be written

$$\overline{\rho u_j'' \phi''} = \overline{\tilde{\rho} u_j'' \phi''} = -\Gamma_t \frac{\partial \bar{\phi}}{\partial x_j}, \quad (2.38)$$

where Γ_t is a positive scalar known as the *turbulent diffusivity*. For the mass fraction and enthalpy, Eq. (2.38) is

$$\overline{\rho u_j'' Y_k''} = \overline{\tilde{\rho} u_j'' Y_k''} = -\frac{\mu_t}{\sigma_Y} \frac{\partial \bar{Y}_k}{\partial x_j}, \quad (2.39)$$

and

$$\overline{\rho u_j'' h''} = \overline{\tilde{\rho} u_j'' h''} = -\frac{\mu_t}{\sigma_h} \frac{\partial \bar{h}}{\partial x_j}, \quad (2.40)$$

respectively. Here, σ_Y is a turbulence Schmidt number and σ_h is a turbulence Prandtl number, both often given a value of 0.9.

2.3 Heat Transfer

The three fundamental methods of heat transfer are conduction, convection and radiation, and they all act and interact in different ways. Brief reviews of conduction and convection will be given, and the more complex mechanism of radiation will be discussed in more detail in its own section.

2.3.1 Conduction

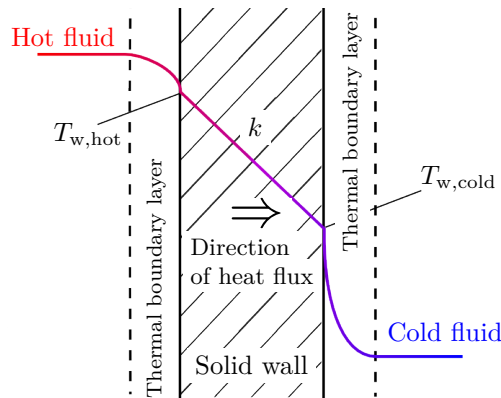


Figure 2.2: Temperature profile through a solid wall with constant conduction coefficient.

For temperature gradients within a solid or stagnant gases or liquids, *conductive* transport of heat will occur. The physical mechanisms is temperature differences within the the medium, or between different mediums, and the heat is conducted from areas with relatively high temperature to areas with relatively low temperatures through molecular interaction. The governing equation of conductive heat transfer is *Fourier's law*, which states that the conductive heat flux is

$$q''_{\text{cond}} = -k\nabla T = -k \frac{\partial T}{\partial x_i}. \quad (2.41)$$

The minus sign is because heat is conducted in the direction of decreasing temperature [8, p. 4], and it is evident that a large temperature gradient leads to a large heat flux. The material property k is the thermal conductivity, which may very well be a function of temperature, but is often approximated as constant. A large value for k implies a good thermal conductor, while a small value of k implies a thermal insulator. Fourier's law part of the energy flux in Eq. (2.1).

2.3.2 Convection

Convective heat transfer is due to the bulk motion of a fluid with a different temperature relative to a solid surface or the boundary of another medium. Strictly speaking, convection includes both energy transfer due to molecular diffusion, and the bulk motion of fluid, advection. However, the terms conduction and advection are often considered synonyms. Two types of convective transfer can be identified: *forced convection* is when the motion of the fluid is caused by some external means, e.g. a fan or atmospheric wind, and *free convection*, when motion in the fluid occur as a result of density changes in the fluid, causing the warmer, less dense fluid elements to rise above the colder, denser fluid elements. In general, forced convection produces a stronger heat flux than free convection. However, the effects of free convection can seldom be completely ignored. In fires, free convection is the reason why a flame rises upwards, and in a zero-gravity environment, flames are often extinguished by their own products due to a lack of oxygen, since the combustion products does not leave the combustion zone as they are not forced away by gravity. This causes an oxygen deficit, and the fuel cannot be oxidized. The nature of free convection can produce substantial velocities for large fires.

The governing equation in convective heat transfer is *Newton's law of cooling* [8, p. 8]:

$$q''_{\text{conv}} = h(T_s - T_\infty), \quad (2.42)$$

where T_s and T_∞ is the surface temperature and the temperature of the fluid, respectively. h is the convective heat transfer coefficient, and is a function of many variables, e.g. fluid velocity, geometry and thermodynamic properties. Determining h can be quite a non-trivial task, especially compared to the conduction coefficient k .

2.4 Radiation

When temperature is high, heat transfer through radiation greatly dominates conduction and convection. When determining hazard zones, for example around a large pool fire, detailed knowledge about radiation heat transfer is needed. The hazard is usually a function of both radiation intensity and exposed time. Buildings and vegetation too close to the plume may catch fire, human skin may get severely burned, and can in worst case scenario cause death. This is a major safety concern in the industry both onshore and offshore, as well as to the public.

2.4.1 Radiation Fundamentals

Radiative heat transfer is fundamentally different from conduction and convection, in that it needs no matter to transport heat. The heat is transferred either by electromagnetic waves or as photons, depending on how you investigate the phenomenon. Radiative properties of gases are more easily viewed as photons

(quantum theory) and those of liquids, solids and interfaces are better predicted by electromagnetic wave theory. The driving force of radiative heat transfer, or thermal radiation, is still temperature differences, however now proportional to the power of fourth: $q \propto T^4 - T_\infty^4$. Radiation is transferred over the entirety of the electromagnetic spectrum, but wavelengths between 10^{-7} m and 10^{-3} m are of greatest importance [25, p. 1]. As thermal radiation may work under extremely large length scales (from 10^{-10} m on a molecular level to 10^{10} m on a planetary level), conservation of energy cannot be applied on an infinitesimal control volume, but has to be applied over the whole volume in effect. This leads to an integral equation with up to seven independent variables, showing the complexity of the issue at hand.

For electromagnetic waves, there exist a number of quantities used to describe the wave. These include the frequency ν , wavelength λ , wavenumber η , and angular frequency ω , which are all related by the equation

$$\nu = \frac{\omega}{2\pi} = \frac{c}{\lambda} = c\eta \quad (2.43)$$

where $c = c_0/n$. c_0 is the speed of light in vacuum and n is the refractive index of the medium transversed by the light. n is approximately equal to unity for most gases. Some terms related to radiation to, from and through media also need to be stated. An *opaque* medium is such that no radiation passes through. A *transparent* medium is a medium in which all radiation passes unattenuated through. A medium in which some radiation passes through and some is attenuated is called *semitransparent*. These properties may depend on various material properties of the medium, and also its thickness. An object may be opaque at some wavelengths but not at others. A surface of an opaque medium which reflects no radiation is called a black surface or black body. This is an idealized case, and serve as a reference for other surfaces.

2.4.2 Emissive Power

All surfaces with temperatures above absolute zero continuously emit radiation randomly in all directions. The radiative heat flux from a surface is called the emissive power, and this emission may happen at various wavelengths. The total emissive power, E , is the spectral emissive power integrated over all wavelengths, frequencies, angular frequencies or wavenumbers:

$$\begin{aligned} E(T) &= \int_0^\infty E_\lambda(T, \lambda) d\lambda = \int_0^\infty E_\nu(T, \nu) d\nu \\ &= \int_0^\infty E_\omega(T, \omega) d\omega = \int_0^\infty E_\eta(T, \eta) d\eta \quad (2.44) \end{aligned}$$

The emissive power distribution from a blackbody, known as *Planck's law* is

$$E_{b\nu}(T, \nu) = \frac{2\pi h\nu^3 n^2}{c_0^2 (e^{h\nu/kT} - 1)}, \quad (2.45)$$

where k is the Boltzmann constant and h is Planck's constant. Using the frequency ν as spectral variable is purely by choice, as one can use any of the variables from Eq. (2.43). The refractive index n is here taken as independent of frequency, which often is reasonable (e.g. for gases), but may not always be the case. The total emissive power of a blackbody is

$$E_b(T) = \int_0^\infty E_{b\nu}(T, \nu) d\nu = n^2 \sigma T^4 \approx \sigma T^4, \quad (2.46)$$

where σ is the Stefan-Boltzmann constant.³

2.4.3 Radiative Intensity

There are many other quantities important to the analysis of radiation heat transfer. The radiative intensity, I , is related to the emissive power E by

$$E_{b\lambda}(\mathbf{r}, \lambda) = \pi I_{b\lambda}(\mathbf{r}, \lambda), \quad (2.47)$$

where \mathbf{r} is a unit vector describing the position in space. Since the emissive power is a function of the temperature, we conclude that the radiative intensity must also be a function of temperature:

$$I_{b\lambda} = I_{b\lambda}(T, \lambda). \quad (2.48)$$

The radiative intensity is the preferred quantity for describing radiative heat transfer, as the emissive power is unable to describe directional dependence of the radiation. The total intensity is found by integrating over the entirety of the domain, following Eq. (2.44):

$$I(\mathbf{r}, \hat{\mathbf{s}}) = \int_0^\infty I_\lambda(\mathbf{r}, \hat{\mathbf{s}}, \lambda) d\lambda, \quad (2.49)$$

where $\hat{\mathbf{s}}$ is a unit direction vector describing the direction of the intensity from a surface. Other important quantities in radiation heat transfer are the irradiation G , which is the rate at which radiation is incident upon a surface per unit area, the radiosity J , which is the rate at which radiation leaves a surface per unit area, and the radiative heat flux q'' , which is the net rate of radiation leaving a surface per unit area, that is, outgoing radiation subtracted by the incoming. The radiative heat flux is thus positive when leaving a surface. The total radiative heat flux at a

³The factor n^2 is often omitted from the equation, as it is approximately equal to 1.

surface is

$$\mathbf{q} \cdot \hat{\mathbf{n}} = \int_0^\infty \int_{4\pi} I_\lambda(\hat{\mathbf{s}}) \hat{\mathbf{n}} \cdot \hat{\mathbf{s}} d\Omega d\lambda. \quad (2.50)$$

2.4.4 Gray Bodies

It is clear that not all surfaces are black. Most bodies are not, and such bodies are called gray. Thus, some fundamental radiative properties needs to be defined. These are the reflectance ρ , absorptance α , transmittance τ and emittance ϵ . ρ , α and τ are defined as [25, p. 21]

$$\begin{aligned} \rho &= \frac{\text{reflected part of incoming radiation}}{\text{total part of incoming radiation}}, \\ \alpha &= \frac{\text{absorbed part of incoming radiation}}{\text{total part of incoming radiation}}, \\ \tau &= \frac{\text{transmitted part of incoming radiation}}{\text{total part of incoming radiation}}, \end{aligned}$$

and ϵ as [25, p. 22]

$$\epsilon = \frac{\text{energy emitted from a surface}}{\text{energy emitted from a black surface at same temperature}}.$$

These are all dimensionless numbers between 0 and 1. All incident radiation on a surface must be either reflected, absorbed or transmitted, and thus we can conclude that

$$\rho + \alpha + \tau = 1. \quad (2.51)$$

A black body, per definition, absorbs all incident radiation. Therefore, for a black surface, $\alpha = 1$ and $\rho = \tau = 0$. From the definition of ϵ , it is evident that $\epsilon = 1$ for a black body.

2.4.5 Radiation Through Gases

Gases, like solids and liquids can emit and absorb radiation. As radiation transverse a gas layer it is attenuated by absorption. Empirically, this leads to an exponential decay in incident radiation, which can be modelled as

$$\tau_\eta = e^{-\kappa_\eta s}, \quad (2.52)$$

where s is the thickness of the gas layer and κ_η is known as the absorption coefficient. Again, the choice of spectral variable is arbitrary, here η is chosen. Since gas does not reflect, we have the spectral absorptivity of a gas layer,

$$\alpha_\eta = 1 - \tau_\eta = 1 - e^{-\kappa_\eta s}. \quad (2.53)$$

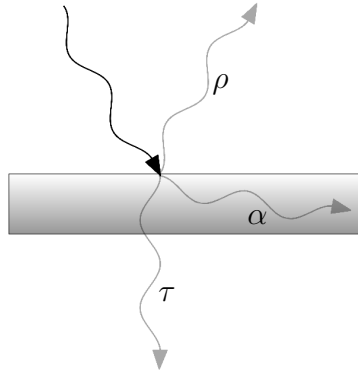


Figure 2.3: Reflected, absorbed and transmitted incident radiation onto a surface.

For radiation through a cloud of small particles, e.g. soot, Eq. (2.52) will have to be modified somewhat. In addition to the mechanisms for a homogeneous medium, e.g. a gas, radiation may be affected through a phenomenon known as *scattering*, where a particle changes the direction a photon travels. Eq. (2.52) is modified to

$$\tau_\eta = e^{-(\kappa_\eta + \sigma_{s\eta})s} = e^{-\beta_\eta s}, \quad (2.54)$$

where $\sigma_{s\eta}$ is the scattering coefficient and β_η is known as the extinction coefficient. The probability that a ray travelling in one direction will be scattered by an angle θ into another direction is called the scattering phase function, Φ_η .

2.4.6 The Radiative Transfer Equation

The *radiative transfer equation* (RTE), perhaps the governing equation of radiative heat transfer, is an energy balance along a so-called *pencil of rays* for a scattering, absorbing and emitting medium. This equation states that, along a unit vector $\hat{\mathbf{s}}$, the intensity changes as

$$\frac{dI_\eta}{ds} = \kappa_\eta I_{b\eta} - \kappa_\eta I_\eta - \sigma_{s\eta} I_\eta + \frac{\sigma_{s\eta}}{4\pi} \int_{4\pi} I_\eta(\hat{\mathbf{s}}_i) \Phi_\eta(\hat{\mathbf{s}}_i, \hat{\mathbf{s}}) d\Omega_i, \quad (2.55)$$

If the gray gas assumption is used, that the absorption coefficient is constant for all wavenumbers [29], Eq. (2.55) can be integrated over all wavenumbers to yield

$$\frac{dI}{ds} = \kappa I_b - \kappa I - \sigma_s I + \frac{\sigma_s}{4\pi} \int_{4\pi} I(\hat{\mathbf{s}}_i) \Phi(\hat{\mathbf{s}}_i, \hat{\mathbf{s}}) d\Omega_i, \quad (2.56)$$

Eqs. (2.55) and (2.56) are integro-differential equations, for which the radiation intensity appear both as a derivative on the LHS and inside the integral on the RHS, and this is extremely hard to solve. Many models, numerical as well as analytical, have been proposed. KFX uses a modified version of the model proposed

by Lockwood and Shah often called the Discrete Transfer Model [34, 35].

2.4.7 The Discrete Transfer Model

The Discrete Transfer Model (DTM), or Lockwood-Shah model, is based on a discrete solution the RTE, Eq. (2.55). Its basis lies in «the solving of representative directed beams of radiation within the enclosure between the well known boundary conditions and on the subsequent computing of the radiation sources which arise within the finite difference control volumes of the flow procedure due to the passage of the beams» [16]. The basic concept of the DTM is that radiative heat transfer within an enclosure is divided into a finite number of cells. From each control volume surface of the boundary, a discrete number of rays are emitted in different spatial directions. Changes in radiation intensity due to absorption and emittance are calculated by numerical integration over the ray until it reaches another boundary. In free flow control volumes, this is included into the source term for the energy conservation equation, and for solid boundaries it is a contribution to the solid temperature equation. As the number of rays go to infinity the DTM converges to the exact solution, however, the computational time also goes to infinity.

The effect of scattering is often ignored, as it is zero for gas flames and negligible for oil flames [16], that is, $\sigma_{s\eta} = 0$ in the RTE. This greatly simplifies Eq. 2.55 to

$$\frac{dI_\eta}{ds} = \kappa_\eta I_{b\eta} - \kappa_\eta I_\eta. \quad (2.57)$$

The intensity around a control volume n is, from Eq. (2.57)

$$I_{\eta,n+1} = \int_0^\infty I_{b\eta}(1 - e^{-\kappa_\eta s})d\eta + \int_0^\infty I_{\eta,n}e^{-\kappa_\eta s}d\eta, \quad (2.58)$$

where $I_{\eta,n+1}$ and $I_{\eta,n}$ are the magnitudes of intensity (per wavenumber) leaving and entering control volume n , respectively. The original paper by Lockwood and Shah [16] states this equation as

$$I_{n+1} = I_n e^{\delta s^\circ} + \frac{E^\circ}{\pi}(1 - e^{\delta s^\circ}), \quad (2.59)$$

where $\delta s^\circ = \beta ds$ is the optical length of the control volume and E° is a modified emissive power, assumed to be uniform in a cell, defined from the RTE as

$$E^\circ = \frac{1}{\beta} \left(\kappa E_b + \frac{\sigma_s}{4\pi} \int_{4\pi} I(\hat{\mathbf{s}}_i) \Phi(\hat{\mathbf{s}}_i, \hat{\mathbf{s}}) d\Omega_i \right). \quad (2.60)$$

The blackbody emissive power, E_b in Eq. (2.60), is equal to σT^4 . Eq. 2.59 is then incorporated into the source term for the energy conservation equation of the flow problem. The contribution to the source term from one beam entering and leaving

a control volume n is

$$S_{n,i} = (I_{n+1} - I_n)\Omega dA d\Omega \quad (2.61)$$

where dA is the area from which the beam of radiation emerges, and Ω is a solid angle representative of the beam. The total radiative source term for control volume n is then found from

$$\dot{Q}_{\text{rad}} dV = S_n = \sum_{i=1}^k S_{n,i}, \quad (2.62)$$

where k is the total number of beams emitted. Eq. (2.62) is the radiant source term in the solved energy equation in KFX, see Eq. (2.117).

2.5 Combustion

Combustion is a highly exothermic chemical reaction between some reactant (or fuel) and an oxidant (normally atmospheric oxygen). For combustion to take place, the «three T's» are needed:

1. **Temperature** – the temperature needs to be high enough for the exothermic reactions to begin. This is called the ignition temperature.
2. **Turbulence** – the fuel and oxygen needs to be molecularly mixed. For this, we need turbulent eddies – «whirls» – to make the reactive molecules come in contact with one another.
3. **Time** – there needs to be sufficient time for breaking up and re-bonding of the fuel and oxidant molecules to different molecules, called products.

As we can see, knowledge about turbulent flows is very important for the understanding of combustion processes. There can be no (or very little) combustion without turbulence. At the very least, some molecular diffusion is needed.

2.5.1 The Eddy Dissipation Concept

The *Eddy Dissipation Concept* (EDC) was first introduced in 1976 by Magnussen and Hjertager [18] and has since been continuously developed and improved. It is based on a cascade model of the turbulence: that kinetic energy enters the turbulence at the largest eddies or length scales, and is then transferred to smaller and smaller scales. At the level of the Kolmogorov scales, the energy is dissipated through viscous forces to the surroundings as heat. In addition, the EDC gives a relation between the small scale and large scale structures by viewing the smaller scales as a function of the largest, and the large scale level can be tied to the mean flow by a turbulence model or solved by Large Eddy Simulation (LES).

The model views the fine structures where the reactions occur as a steady homogeneous reactor. Mass balance for the reactor gives the rate of reaction for the

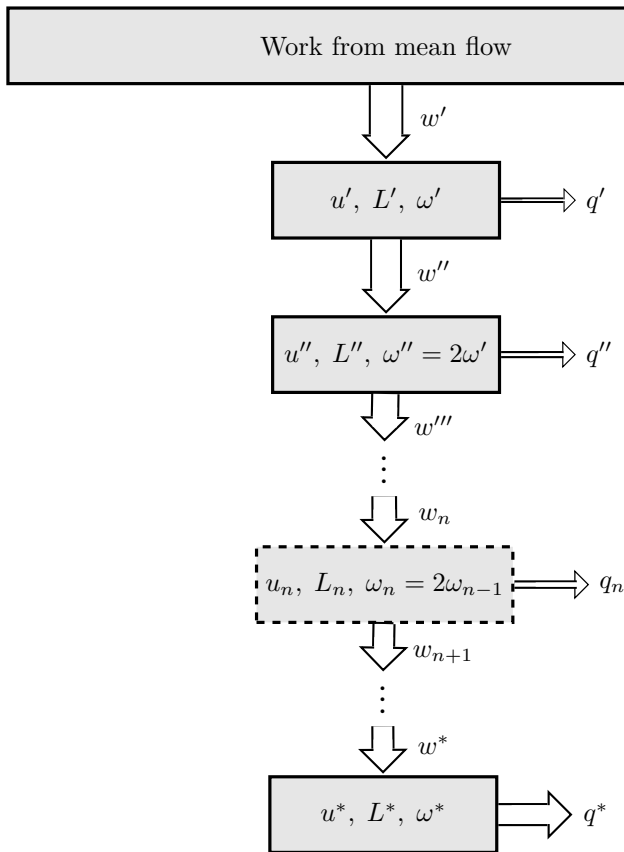


Figure 2.4: Energy cascade in the Eddy Dissipation Concept

reactor, as well as the mean rate of reaction. This is interpreted as the source term in the equation for mean mass fraction. The temperature in the fine structures is found by energy balance for the reactor. Flame extinction properties can be found by modelling the residence time and comparing the the rate of reaction. Calculations for detailed chemical kinetics can also be tied to the model.

Interstructural Energy Transfer

The cascade model is rooted in the mean flow, viewed as the top level of the cascade. From the mean flow, mechanical energy is transferred to the turbulence. This is the production of turbulence energy P_k for an equilibrium ($P_k = \varepsilon$), here denoted as w' . The second level of the cascade – or the first level of the turbulence structures – is the energy and momentum rich large eddies. Characteristic scales include the characteristic velocity u' , length L' and frequency $\omega' = u'/L'$. Mean turbulence equations are solved at this level, e.g. the $k-\varepsilon$ model. From this level, some energy

q' is dissipated to the surroundings as heat and the rest is transferred as mechanical energy, w'' , to the next level of the cascade. The total turbulence dissipation from this level is $\varepsilon = q' + w''$. The second turbulence level has characteristics u'' , L'' and $\omega'' = u''/L'' = 2\omega'$, and the dissipation from this level is $\varepsilon' = q'' + w''$. This continues for every level n where the incoming kinetic energy is w_n , characteristics are u_n , L_n , $\omega_n = u_n/L_n = 2\omega_{n-1}$ and dissipation is $\varepsilon_n = q_n + w_{n+1}$. At the last level, the characteristic scales, u^* , L^* and ω^* , are of the same order of the Kolmogorov scales (see Sec. 2.2.2), and this where the majority and the remaining of turbulence energy is dissipated through viscous friction as q^* .

The model equations can be written as

$$w'' = \frac{3}{2}C_{D1}\omega'2u''^2 \quad \text{and} \quad q' = C_{D2}\nu\omega'^2 \quad (2.63)$$

where C_{D1} and C_{D2} are model constants. Magnussen [17] assumes similar expressions for all levels of the cascade. This gives

$$w_n = \frac{3}{2}C_{D1}\omega_n u_n^2 \quad \text{and} \quad q_n = C_{D2}\nu\omega_n^2 \quad (2.64)$$

for level n of the cascade. Again, assuming equilibrium in the cascade, we get can see that $w_n = q_n + w_{n+1}$. For non-low Reynolds number flows there is little dissipation from the top levels. It is therefore reasonable to say that $q_n \ll w_n$, and as such $w_{n+1} = w_n$ and $(u'')^2 = \frac{1}{2}u'^2$. Eq. (2.63) then becomes

$$w'' = \frac{3}{2}C_{D1}\omega'u'^2 = C_{D1}\omega'k \quad \text{and} \quad q' = C_{D2}\nu\omega'^2. \quad (2.65)$$

k in Eq. (2.65) is the turbulence kinetic energy, see Sec. 2.2.2, and can thus be tied to the $k - \varepsilon$ model. Eq. (2.65) can be seen as an approximation to Eq. (2.63). By modelling the turbulent viscosity as $\nu_t = u'L'$ and using the approximation $\varepsilon = w'' = \frac{3}{2}C_{D1}u'^3/L'$, we get

$$\nu_t = \frac{3}{2}C_{D1} \frac{u'^4}{\varepsilon} = \frac{2}{3}C_{D1} \frac{k^2}{\varepsilon}. \quad (2.66)$$

Noticing that $\frac{2}{3}C_{D1}$ corresponds to C_μ by comparing to the $k - \varepsilon$ model ($\nu_t = C_\mu k^2/\varepsilon$), we get $C_{D1} \approx 0.135$. At the last level of the cascade, where $w^* = q^*$, the equations become:

$$w^* = \frac{3}{2}C_{D1}\omega^*u^{*2} \quad \text{and} \quad q^* = C_{D2}\nu\omega^{*2} \quad (2.67)$$

These derivations follow Ertesvåg [5], but are similar to Magnussen [17], who uses the values $C_{D1} = 4\xi^2 = 0.134$ and $C_{D2} = 15\xi^2 = 0.50$, with ξ being a numerical parameter. It can be shown [17] that the dissipation from one level of the cascade equals a quarter of the dissipation from the succeeding level, and, for high-Reynolds number flows, that the accumulated dissipation ε equals $\frac{4}{3}q^*$. These relationships of the energy balance are used to find typical quantities governing the combustion.

Continuing to assume high-Reynolds number flows, we get [20]

$$\varepsilon \approx w'' = 0.2 \frac{u'^3}{L'} = 0.67\nu \frac{u'^2}{L'^2} = 0.267 \frac{u'^3}{L'^2}. \quad (2.68)$$

By looking at the last two terms of Eq. (2.68), we get

$$L^* = 1.43 \left(\frac{\nu^3}{\varepsilon} \right)^{1/4}, \quad (2.69)$$

and

$$u^* = 1.75(\nu\varepsilon)^{1/4}, \quad (2.70)$$

which together produces the Reynolds number for the fine structures:

$$\text{Re}^* = \frac{u^* L^*}{\nu} = 2.5. \quad (2.71)$$

The Fine Structures

An important assumption of the EDC is that the majority of the chemical reactions occur in the fine structures of the turbulence [17]. To be able to treat the reactions in these structures, a relation between the mass in the fine structure and the surrounding fluid has to be found. This mass fraction is assumed to be⁴ [17]

$$\gamma^* = \left(\frac{u^*}{u'} \right)^3. \quad (2.72)$$

By assuming nearly isotropic turbulence ($k = \frac{3}{2}u'^2$), and by introducing u^* from Eq. (2.70), Eq. (2.72) can be written

$$\gamma^* = 9.8 \left(\frac{\nu\varepsilon}{k^2} \right)^{3/4} = 9.8 \text{Re}_t^{-3/4}, \quad (2.73)$$

where Re_t is the turbulence Reynolds number. Additionally, the ratio of the fine structure regions to the total mass is denoted γ_λ , and is given by

$$\gamma_\lambda = (\gamma^*)^{1/3}. \quad (2.74)$$

The mass transfer between the fine structures and the surrounding fluid per unit mass of the *surrounding fluid* can be expressed as

$$\dot{m} = 2 \frac{u^*}{L^*} \gamma^* \quad \text{or} \quad \dot{m} = 24 \left(\frac{\nu\varepsilon}{k^2} \right)^{1/4} \frac{\varepsilon}{k}, \quad (2.75)$$

⁴In the most recent versions of the EDC, i.e. [20] or [22], the RHS of Eq. (2.72) is to the power of 2, not 3. Consequently, Eq. (2.73) will be $\gamma^* = 4.6 \text{Re}_t^{-1/2}$, and subsequent equations with γ^* will be different. This form of the EDC is not yet fully implemented in KFX.

expressed by fine structure scales or by k and ε , respectively. The mass transfer per unit mass of the *fine structures* can be expressed as

$$\dot{m}^* = 2 \frac{u^*}{L^*} \quad \text{or} \quad \dot{m}^* = 2.45 \left(\frac{\varepsilon}{\nu} \right)^{1/2}, \quad (2.76)$$

here in terms of either by fine structure scales or by dissipation and viscosity. The residence time, that is, how long a fluid particle resides in the fine structures, is consequently

$$\tau^* = \frac{1}{\dot{m}^*}. \quad (2.77)$$

A factor χ is defined to account for that not all of the fine structures react, and is given as [34]

$$\chi = \frac{\tilde{Y}_{\text{Pr}}}{\left(\tilde{Y}_{\text{pr}} + (1+r)\tilde{Y}_{\text{max}} \right) \gamma_\lambda}, \quad (2.78)$$

where

$$\tilde{Y}_{\text{max}} = \max \left\{ \tilde{Y}_{\text{fu}}, \frac{\tilde{Y}_{\text{ox}}}{r} \right\}, \quad (2.79)$$

and r is the mass of oxidant reacting with 1 kg fuel to $1+r$ kg product. A fine structure mixing rate coefficient, η , is given as

$$\eta = \min \left\{ \frac{1}{\gamma_\lambda}, \frac{\tilde{Y}_{\text{pr}}/(1+r) + \tilde{Y}_{\text{min}}}{\tilde{Y}_{\text{min}}} \right\}, \quad (2.80)$$

where

$$\tilde{Y}_{\text{min}} = \min \left\{ \tilde{Y}_{\text{fu}}, \frac{1}{r} \tilde{Y}_{\text{ox}} \right\}. \quad (2.81)$$

The Interstructural Mixing Process - The Reactor Model

The fine structured region in the EDC is viewed as a well-mixed reactor and the reactants are assumed to be homogeneously mixed in this region. In this reactor, a species and enthalpy balance is given as

$$\frac{dY_k^*}{dt} + \frac{1}{\tau^*} (Y_k^* - Y_k^\circ) = \dot{R}_k^*, \quad (2.82)$$

and

$$\frac{dh^*}{dt} + \frac{1}{\tau^*} (h^* - h^\circ) = \frac{1}{\rho^*} \frac{dp}{dt}, \quad (2.83)$$

respectively. $^\circ$ and * indicate incoming surrounding conditions and the the fine structures conditions inside the reactor, respectively, and p is the pressure. \dot{R}_k^* is the reaction rate per unit mass of the burning fine structures. For an adiabatic reactor, the energy going in must equal the energy going out. Assuming a constant

mass flow through this reactor, we get

$$h^\circ = h^*, \quad (2.84)$$

where h° can be found from the enthalpy field. In a mixture at constant pressure, the enthalpy in the fine structures can be given by

$$h^* = C_p(T^* - T_{\text{ref}}) + Y_{\text{fu}}^* H_R, \quad (2.85)$$

where C_p is the specific heat capacity, H_R the heat of reaction of the fuel, and T_{ref} is a reference temperature, usually 298.15 K [6]. The enthalpy in the surroundings h° is given by

$$h^\circ = C_p(T^\circ - T_{\text{ref}}) + Y_{\text{fu}}^\circ H_R. \quad (2.86)$$

Rearranging, the temperature in the fine structures can be given:

$$T^* = \frac{H_R}{C_p}(Y_{\text{fu}}^\circ - Y_{\text{fu}}^*) + T^\circ. \quad (2.87)$$

Assuming all reactions occur in the fine structures, the density weighted average reaction rate is given as [34]

$$\tilde{R}_k = \gamma^* \chi \eta \dot{R}_k^*, \quad (2.88)$$

and the scalar quantities average enthalpy, density weighted average temperature and density weighted average mass fraction are given as

$$\tilde{h} = \gamma^* \chi \eta h^* + (1 - \gamma^* \chi \eta) h^\circ, \quad (2.89)$$

$$\tilde{T} = \gamma^* \chi \eta T^* + (1 - \gamma^* \chi \eta) T^\circ, \quad (2.90)$$

and

$$\tilde{Y}_k = \gamma^* \chi \eta Y_k^* + (1 - \gamma^* \chi \eta) Y_k^\circ, \quad (2.91)$$

respectively.

The Fast Chemistry Limit

In the fast chemistry limit, that is, assuming infinitely fast reactions, the EDC can produce sufficient results for a great number of cases. This is done by looking for the limiting component of the reactions. By using Eq. (2.91) and derivation by Ertesvåg [6], a reaction rate for the fuel can be produced, and given as

$$\dot{R}_{\text{fu}}^* = -\frac{1}{\tau^*(1 - \gamma^* \chi \eta)} \tilde{Y}_{\text{min}}, \quad (2.92)$$

and a density weighted average reaction rate as

$$\tilde{R}_{\text{fu}} = -\frac{\gamma^* \chi \eta}{\tau^*(1 - \gamma^* \chi \eta)} \tilde{Y}_{\text{min}}, \quad (2.93)$$

where \tilde{Y}_{\min} is defined in Eq. (2.81). Finally, the temperature in the fine structures can be given as [6]

$$T^* = \frac{H_R}{C_p} \tilde{Y}_{\min} + \tilde{T}. \quad (2.94)$$

2.5.2 The Eddy Dissipation Soot Model

Soot is a solid mass of mostly carbon particles (along with some hydrogen) resulting from an incomplete combustion of hydrocarbons. Tesner et al. [32] describes it as «a process consisting of a new dispersed phase from the gas phase». This is a multi-stage process where the beginning with the decomposition of fuel into alkynes. These are in turn polymerized into polycyclic aromatic hydrocarbons (PAHs). The next stage is the formation of so-called *radical nuclei*, and the last stage is the growth and aggregation of larger soot particles from these nuclei.

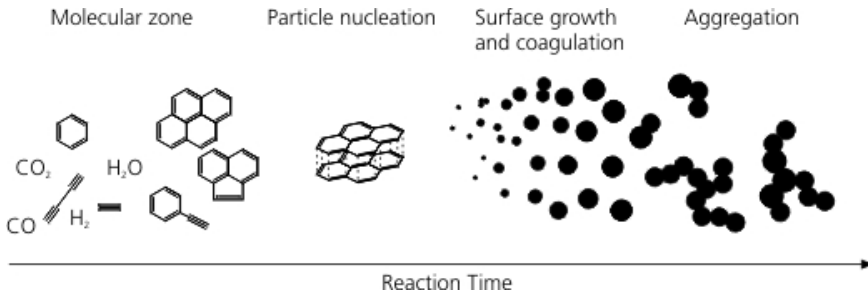


Figure 2.5: Soot formation process. From [10].

Knowledge about soot formation is important for two major reasons. For one, soot is the major contributor to the optical properties of a flame. As most of the radiation of a flame originates in soot at high temperatures, and radiative heat transfer models cannot properly be applied without knowledge about the soot concentration and distribution in and surrounding the flame. Relatively cold soot in the vicinity of the flame lowers radiation from the flame to the surroundings due to so-called soot shielding. Secondly, soot is considered a major pollutant, and in urban areas about 70% of airborne fine particles are a result of combustion processes [4].

2.5.2.1 Soot Formation

The Eddy Dissipation Soot Model is decoupled from the energy and mass species balances. Its basis lies in the work done by Tesner et al. [32] for acetylene. Tesner's soot model was also applied to diffusion flames of other hydrogen-hydrocarbon mixtures [33]. The equation for the formation rate of radical nuclei is given by Tesner et al. [32] as

$$\frac{dn}{dt} = n_0 + (f - g)n - g_0 Nn, \quad (2.95)$$

Table 2.1: Constants in the Eddy Dissipation Soot Model.

Constant	Value	Unit
a	$= 10^5$	part. soot/part. nuc/s
b	$= 8.0 \times 10^8$	$\text{m}^3/\text{part. nuc/s}$
$f - g$	$= 10^2$	–
g_0	$= 10^{-15}$	$\text{m}^3/\text{part. soot/s}$
E/\mathcal{R}	$= 9 \times 10^4$	K
a_0	$= 12.5 \times 10^{36}$	part. nuc/kg carbon/s
ρ_s	$= 2000$	kg/m^3
d_s	$= 128.5$	Å

and the equation for the formation rate of soot particles

$$\frac{dN}{dt} = (a - bN)n. \quad (2.96)$$

n is the concentration of radical nuclei and N is the concentration of soot particles, both with units particles per m^3 . The constant f is a linear branching coefficient and g is a linear termination coefficient. g_0 is a coefficient of linear termination on soot particles, a and b are numerical constants. n_0 is the spontaneous formation rate of radical nuclei, and is by Magnussen [19] given as

$$n_0 = 1.08a_0Y_C\tilde{\rho}_{\text{fu}}e^{-E/\mathcal{R}T}. \quad (2.97)$$

a_0 and E are constants, Y_C is the mass fraction of carbon in the fuel, $\tilde{\rho}_{\text{fu}}$ is the mean concentration of fuel, \mathcal{R} is the universal gas constant and T is the temperature in the region. Eq. (2.97) has been modified from Tesner's original formulation [32] in order to be applicable to fuels other than acetylene. Eqs. (2.95) and (2.96) can be given in mass fractions as [34]

$$\frac{dY_{\text{nuc}}}{dt} = R_{\text{nuc},f} = \frac{n_0}{\rho_a} + (f - g)Y_{\text{nuc}} - \frac{g_0}{m_p}\rho_aY_{\text{nuc}}Y_{\text{soot}}, \quad (2.98)$$

and

$$\frac{dY_{\text{soot}}}{dt} = R_{\text{soot},f} = Y_{\text{nuc}}(am_p - b\rho_aY_{\text{soot}}), \quad (2.99)$$

respectively, where the mass of a soot particle, m_p , has been introduced, and is given by

$$m_p = \frac{\pi}{6}\rho_s d_p^3, \quad (2.100)$$

where d_s is the diameter of a soot particle. An overview over the various constants and coefficients in the EDC soot model are given in Table 2.1.

An important presumption is that no more soot can be formed than the amount of carbon present in the fuel. Additionally, the fact that under certain conditions

virtually all of the carbon in the fuel is converted to soot is worth including in the soot model, including variation due to different fuels. Eqs. (2.98) and (2.99) are then modified to

$$\frac{dY_{\text{nuc}}}{dt} = R_{\text{nuc},f} = \frac{n_0}{\rho_a} + (f - g)Y_{\text{nuc}} \frac{Y_{\text{soot,max},1}}{Y_{\text{soot,max},2}} - \frac{ag_0}{b} Y_{\text{nuc}} \frac{Y_{\text{soot}}}{Y_{\text{soot,max},2}}, \quad (2.101)$$

and

$$\frac{dY_{\text{soot}}}{dt} = R_{\text{soot},f} = \rho_a b Y_{\text{soot,max},1} Y_{\text{nuc}} \left(1 - \frac{Y_{\text{soot}}}{Y_{\text{soot,max},2}} \right). \quad (2.102)$$

The new quantities, $Y_{\text{soot,max},i}$ for $i = 1, 2$, are defined as

$$Y_{\text{soot,max},1} = F_C Y_{\text{fu}} - Y_{\text{soot}}, \quad (2.103a)$$

$$Y_{\text{soot,max},2} = F_C Y_{\text{fu}}, \quad (2.103b)$$

where F_C is the total carbon content in the fuel:

$$F_C = \xi_{\text{fu},C} - \frac{A_C}{2A_O} \xi_{\text{fu},O}. \quad (2.104)$$

Backwards compatibility with Eqs. (2.98) and (2.99) gives

$$Y_{\text{soot,max},1} = Y_{\text{soot,max},2} = \frac{am_p}{b\rho_a}. \quad (2.105)$$

2.5.2.2 Soot Combustion

In the EDC, the fuel burns at a fraction of $\gamma^* \chi$ with a rate of \dot{m}^* . The same applies for the combustion of soot, and a major assumption is that the combustion of nuclei and soot is proportional to the combustion of fuel. That is,

$$R_{\text{nuc},c}^* = R_{\text{fu},c}^* \frac{\tilde{Y}_{\text{nuc}}}{\tilde{Y}_{\text{fu}}}, \quad (2.106)$$

and

$$R_{\text{soot},c}^* = R_{\text{fu},c}^* \frac{\tilde{Y}_{\text{soot}}}{\tilde{Y}_{\text{fu}}}. \quad (2.107)$$

In accord with the EDC, we assume infinitely fast reactions and the combustion rate of the fuel follows as

$$R_{\text{fu},c}^* = -\frac{\rho_a^* \dot{m}^*}{1 - \gamma^* \chi} \tilde{Y}_{\text{min}}, \quad (2.108)$$

and we get the combustion rates for the nuclei and soot:

$$R_{\text{nuc,c}}^* = -\frac{\rho_a^* \dot{m}^*}{1 - \gamma^* \chi} \tilde{Y}_{\text{min}} \frac{\tilde{Y}_{\text{nuc}}}{\tilde{Y}_{\text{fu}}}, \quad (2.109)$$

and

$$R_{\text{soot,c}}^* = -\frac{\rho_a^* \dot{m}^*}{1 - \gamma^* \chi} \tilde{Y}_{\text{min}} \frac{\tilde{Y}_{\text{soot}}}{\tilde{Y}_{\text{fu}}}. \quad (2.110)$$

2.5.2.3 Overall Soot Model

Balancing the formation and combustion rates of the nuclei and soot gives the following equations for the fine structure reactor:

$$R_{\text{nuc,f}}^* + R_{\text{nuc,c}}^* = \frac{\rho_a^* \dot{m}^*}{1 - \gamma^* \chi} \left(Y_{\text{nuc}}^* + \tilde{Y}_{\text{nuc}} \right), \quad (2.111)$$

and

$$R_{\text{soot,f}}^* + R_{\text{soot,c}}^* = \frac{\rho_a^* \dot{m}^*}{1 - \gamma^* \chi} \left(Y_{\text{soot}}^* + \tilde{Y}_{\text{soot}} \right). \quad (2.112)$$

The amount nuclei and soot in the fine structure surroundings can be expressed as

$$Y_{\text{nuc}}^\circ = \frac{\tilde{Y}_{\text{nuc}} - \gamma^* \chi Y_{\text{nuc}}^*}{1 - \gamma^* \chi}, \quad (2.113)$$

and

$$Y_{\text{soot}}^\circ = \frac{\tilde{Y}_{\text{soot}} - \gamma^* \chi Y_{\text{soot}}^*}{1 - \gamma^* \chi}, \quad (2.114)$$

respectively. Consequently, the averaged reaction rates will be

$$\tilde{R}_{\text{nuc}} = \gamma^* \chi (R_{\text{nuc,f}}^* + R_{\text{nuc,c}}^*) + (1 - \gamma^* \chi) R_{\text{nuc,f}}^\circ, \quad (2.115)$$

and

$$\tilde{R}_{\text{soot}} = \gamma^* \chi (R_{\text{soot,f}}^* + R_{\text{soot,c}}^*) + (1 - \gamma^* \chi) R_{\text{soot,f}}^\circ. \quad (2.116)$$

This section focused on the steady-state solution of the soot formation. For investigation into the transient behaviour, see e.g. [34].

2.6 KFX Models and Numerics

In this section, implementation of various physical models in KFX and computational schemes are explained in brief. Most of the information comes from the KFX Theory Manual [34], and some information is from other sources.

2.6.1 Conservation of Energy

For incompressible flow in KFX, the enthalpy equation is written as

$$\frac{\partial \tilde{\rho} \tilde{h}}{\partial t} + \frac{\partial \tilde{\rho} \tilde{u}_j \tilde{h}}{\partial x_j} = \frac{\partial}{\partial x_j} \left(\frac{\mu_t}{\sigma_{\tilde{h}}} \frac{\partial \tilde{h}}{\partial x_j} \right) + \tilde{\rho} \tilde{Q}_{\text{gs}} + \tilde{\rho} \tilde{Q}_{\text{rad}} + \tilde{\rho} \tilde{Q}_{\text{liq}}. \quad (2.117)$$

\tilde{Q}_{rad} is the radiative source term and follows from Eq. (2.62). \tilde{Q}_{gs} and \tilde{Q}_{liq} is the energy transfer from the solids and liquids present to the gas.

2.6.2 Turbulence Model

KFX uses the Favre averaged $k - \varepsilon$ model outlined in Sec. 2.2.4. The buoyancy coefficient B in Eqs. (2.28) and (2.29) should follow from the buoyancy term in Eq. (2.17). By applying a gradient model on ρ' (Eq. (2.38)) we can write the buoyancy coefficient as

$$B = -\frac{\mu_t}{\sigma_\rho} \frac{\partial \bar{\rho}}{\partial x_i} \frac{g}{\rho_o} \delta_{i3}, \quad (2.118)$$

where σ_ρ is the turbulent Prandtl number, and takes a value of 0.7. ρ_o is the ambient density. The value of the model constant $C_{\varepsilon 3}$ is either 1 or 0, depending on whether there is stability or instability in the local region, respectively. For the most part, $C_{\varepsilon 3}$ is equal to zero. However, during the work on this thesis, a programming error was found in the KFX source code, and the buoyancy term is programmed according to the equation

$$B = -\frac{\mu_t}{\sigma_\rho} \frac{\partial \bar{\rho}}{\partial z} g, \quad (2.119)$$

giving wrong units for the buoyancy term in Eqs. (2.28) and (2.29).⁵

Near walls and in boundary layers, law walls are used as a way to avoid the need of having a much finer grid in these areas, and therefore less computationally expensive. For discussion into wall laws and turbulent boundary layers, see e.g. Pope [30, pp. 264–310] or Ertesvåg [6, pp. 66–77].

2.6.3 Combustion and Soot Model

KFX uses the EDC combustion and soot models outlined in Secs. 2.5.1 and 2.5.2, respectively. The soot mass fraction is used to find the radiative absorption coefficient used in the implemented version of the DTM to calculate radiative heat transfer inside the flame and between the flame and the surroundings.

⁵However, the implications of this error is small. ρ_o is the reference density of air, and as this is approximately 1 kg/m³, this does not do much of a difference numerically.

2.6.4 Radiation Model

KFX uses the DTM by Lockwood and Shah [16] described in Sec. 2.4.7, with extensions to enable computationally efficient and accurate calculations of the radiation exchange between gas, soot and surroundings. Evident from the radiative transfer equation (RTE), Eq. (2.55), the radiation is strongly dependent on the absorption coefficient, κ . The absorption coefficient typically varies greatly with wavelength [24, p. 557], and the calculation of spectral dependence is a complex task, so averages over the spectral bands are often used instead. The radiant properties of a flame are for the most part a function of temperature and concentration of combustion products – CO₂, H₂O and soot – and the absorption coefficient calculated in KFX is thus a function of these.

As there are a lack of satisfactory expressions for the absorption coefficient, it is found by determining the emission coefficient instead. This is done by applying Kirchoff's law of thermal radiation in an equilibrium, $\alpha_\lambda = \epsilon_\lambda$, to Eq. (2.53):

$$\epsilon_\lambda = \alpha_\lambda = 1 - \tau_\lambda = 1 - e^{-\kappa_\lambda s}. \quad (2.120)$$

By using total properties averaged over all wavelengths ($\kappa_\lambda \approx \kappa$, etc.) and solving for the absorption coefficient κ , we get

$$\kappa = -\frac{1}{s} \ln(1 - \epsilon). \quad (2.121)$$

The total emission coefficient is then written

$$\epsilon = \epsilon_s + \epsilon_g - \epsilon_s \epsilon_g, \quad (2.122)$$

where ϵ_s is the integrated emissivity of soot, ϵ_g is the integrated emissivity of H₂O and CO₂ combined, and $\epsilon_s \epsilon_g$ represents a correction term due to overlap of the two.

The emissivity of soot, ϵ_s , can be given by the expression [26, 28]

$$\epsilon_s = 1 - \frac{15}{\pi^4} \Psi^{(3)} \left(1 + \frac{7\tilde{T}_F C s}{C_2} \right), \quad (2.123)$$

where s is the optical thickness, or path length, of the flame, \tilde{T}_F is the flame temperature, C is an effective soot concentration parameter, C_2 is Planck's second constant and $\Psi^{(3)}$ is the penta-gamma function. A poly-gamma function, $\Psi^{(n)}$, is a function evaluated by the poly-gamma series expansion

$$\Psi^{(n)}(z) = (-1)^{n+1} n! \sum_{k=0}^{\infty} (z+k)^{-n-1}, \quad (2.124)$$

by Abramowitz and Stegun [1, pp. 255–260], with the penta-gamma function being

$$\Psi^{(3)}(z) = 6 \sum_{k=0}^{\infty} \frac{1}{(z+k)^4}, \quad (2.125)$$

by Hamming [7, p. 209].

The effective soot concentration parameter C , can be expressed as

$$C = \frac{\rho_a}{\rho_{\text{soot}}} Y_{\text{soot}}, \quad (2.126)$$

where Y_{soot} follows from the EDC soot model in Sec. 2.5.2.

Evaluation of the emission from the gas phases, ϵ_g is more complex. The model implemented in KFX is according to the work of Leckner [14]. Firstly, the $\text{H}_2\text{O}-\text{CO}_2$ emissivity has modelled similarly to the soot-gas emissivity:

$$\epsilon_g = \epsilon_{\text{H}_2\text{O}} + \epsilon_{\text{CO}_2} - \Delta\epsilon, \quad (2.127)$$

where $\Delta\epsilon$ accounts for the overlapping emissivity region of the two gases. Two important parameters being used in this model are

$$\tau = \tilde{T}/1000 \quad (2.128)$$

and

$$\zeta = \log(100ps), \quad (2.129)$$

where \tilde{T} is the temperature, p is the partial pressure and s is the mean path length. It is worth noting that here, τ is *not* the transmittance, but rather a model parameter. The total emissivity from one of the gaseous components can be given as

$$\epsilon = \epsilon_0 \left(1 + \left(\frac{Ap_E + B}{p_E + A + B - 1} - 1 \right) \exp(-\chi(\zeta_{\text{max}} - \zeta)^2) \right). \quad (2.130)$$

Here, A , B , χ and ζ_{max} are model constants and coefficients varying for each of the species. p_E is an equivalent pressure dependent on the partial pressure p_i , the total pressure p_{tot} , and temperature, and is also dependent on the specie. Additionally, the factor ϵ_0 which is the emissivity at zero partial pressure, is computed from the polynomial

$$\log \epsilon_0 = \sum_{i=0}^M b_i \zeta^i \quad (2.131)$$

where b_i is the polynomial

$$b_i = \sum_{j=0}^N c_{ji} \tau^j. \quad (2.132)$$

i and j are indices summed over, and M and N are the integers being summed to by i and j , respectively. Values for c_{ji} for CO_2 and H_2O used in KFX are given in

Table 2.2: Values for c_{ji} for CO₂. $M = 3$, $N = 4$. $T > 400$ K.

c_{ji}	$j = 0$	$j = 1$	$j = 2$	$j = 3$	$j = 4$
$i = 0$	-3.9781	2.7353	-1.9882	0.31054	0.015719
$i = 1$	1.9326	-3.5932	3.7247	-1.4535	0.20132
$i = 2$	-0.35366	0.61766	-0.84207	0.39859	-0.063356
$i = 3$	-0.080181	-0.31466	-0.19973	0.046532	-0.0033086

Table 2.3: Values for c_{ji} for H₂O. $M = 2$, $N = 2$. $T > 400$ K.

c_{ji}	$j = 0$	$j = 1$	$j = 2$
$i = 0$	-2.2118	-1.1987	0.035596
$i = 1$	0.85667	0.93048	-0.14391
$i = 2$	-0.10838	-0.17156	0.045915

Tables 2.2 and 2.3. The model constants and coefficients for CO₂ are given as

$$p_E = p_{\text{tot}} \left(1 + 0.28 \frac{p_{\text{CO}_2}}{p_{\text{tot}}} \right), \quad (2.133a)$$

$$\zeta_{\text{max}} = \log(0.225\tau^2), \quad (2.133b)$$

$$A = 0.10\tau^{-1.45} + 1.0, \quad (2.133c)$$

$$B = 0.23, \quad (2.133d)$$

$$\chi = 1.47, \quad (2.133e)$$

and for H₂O as

$$p_E = p_{\text{tot}} \left(1 + 4.9 \frac{p_{\text{H}_2\text{O}}}{p_{\text{tot}}} \sqrt{273/\tilde{T}} \right), \quad (2.134a)$$

$$\zeta_{\text{max}} = \log(13.2\tau^2), \quad (2.134b)$$

$$A = 1.888 + 2.053 \log \tau, \quad (2.134c)$$

$$B = 1.1\tau^{-1.4}, \quad (2.134d)$$

$$\chi = 0.5. \quad (2.134e)$$

Finally, the term $\Delta\epsilon$, representing the overlapping emissivity region for CO₂ and H₂O, has to be identified. Leckner [14] proposed the expression

$$\Delta\epsilon = \left(\frac{\beta}{10.7 + 101\beta} - 0.0089\beta^{10.4} \right) \zeta_{\text{CO}_2+\text{H}_2\text{O}}^{2.76}, \quad (2.135)$$

with β being

$$\beta = \frac{p_{\text{H}_2\text{O}}}{p_{\text{H}_2\text{O}} + p_{\text{CO}_2}} \quad (2.136)$$

and $\zeta_{\text{CO}_2+\text{H}_2\text{O}}$ following from Eq. (2.129):

$$\zeta_{\text{CO}_2+\text{H}_2\text{O}} = \log(100(p_{\text{CO}_2} + p_{\text{CO}_2})s). \quad (2.137)$$

2.6.5 Pool Spreading in KFX

In KFX, an extended version of the shallow water equations is implemented [27]. They are based on the incompressible Navier-Stokes equations in two dimensions and solved using Rusanov's method. A simplification inherent to the equations is that the length scale normal to the pool is far less than its radial length scale. This allows for the averaging of various quantities in the z -direction of the liquid pool. These equations form a conservation law by the vector of conserved variables q_i , flux function F_{ij} and source term S_i :

$$\frac{\partial q_i}{\partial t} + \frac{\partial F_{ij}}{\partial x_j} = S_i, \quad (2.138)$$

where q_i , F_{ij} are

$$q_i = \begin{pmatrix} m'' \\ m''u_x \\ m''u_y \\ m''T_l \\ m''_k \end{pmatrix}, \quad F_{ij} = \begin{pmatrix} m''u_x & m''u_y \\ m''u_x^2 + \frac{g}{2\rho}m''^2 & m''u_xu_y \\ m''u_yu_x & m''u_y^2 + \frac{g}{2\rho}m''^2 \\ m''T_lu_x & m''T_lu_y \\ m''_ku_x & m''_ku_y \end{pmatrix}, \quad (2.139)$$

and the source term S_i

$$S_i = \begin{pmatrix} -\dot{m}''_{\text{vap}} \\ -\tau_x - gm''\frac{\partial b}{\partial x} - \dot{m}''_{\text{vap}}u_x \\ -\tau_y - gm''\frac{\partial b}{\partial y} - \dot{m}''_{\text{vap}}u_y \\ \frac{1}{c_{pt}}Q - T_l\dot{m}''_{\text{vap}} \\ \dot{m}''_{\text{vap}} \end{pmatrix}. \quad (2.140)$$

The function Q in the source term represents the various modes of heat transfer to and from the liquid pool, and is

$$Q = E(\dot{q}_{\text{rad}} - \sigma T_l^4) + h_{\text{amb}}(T_{\text{amb}} - T_l) + h_w(T_w - T_l) - \sum_k h_{\text{fg},k}\dot{m}''_{\text{vap},k}. \quad (2.141)$$

In these equations, subscripts i and j are tensor notation, while the k represents the various species present in the liquid, and the last term in Eqs. (2.139) and (2.140) are equal in number to the number of species in the liquid phase. m'' is the mass of liquid per area of the pool. The quantity h_w in Q represents the heat transfer coefficient from the water or ground on which the pool is spreading, and has been the subject of a master's thesis in its own, see Myrmo [27]. The other heat transfer mechanisms are taken care of by other models in KFX, e.g. the radiative

heat transfer \dot{q}_{rad} which is found by the Discrete Transfer Model described in Sec. (2.4.7).

2.6.6 Staggered Grid

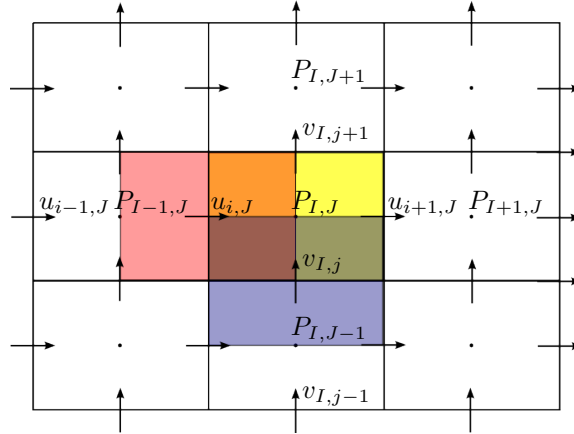


Figure 2.6: Configuration of a staggered grid in 2D. u and v denotes the horizontal and vertical components of the velocity vector, respectively, and P denotes the center-point node.

For the numerical computations, KFX uses a Finite Volume Method (FVM) on a staggered grid. The staggered grid is introduced as a way to avoid unphysical «checkerboard patterns» of the pressure at the various nodes. In the staggered grid, the velocity convective fluxes are computed at skewed cell faces, e.g. in 2D, the grid for the horizontal convective fluxes are skewed half a grid spacing to the west, and the grid for the vertical convective fluxes are skewed half a grid spacing to the south, as seen in in Figure 2.6. The horizontal arrows (\rightarrow) indicate the position where the u -velocities are calculated, and the vertical arrows (\uparrow) indicate the position where the v -velocities are calculated. All scalar values, such as pressure, density and temperature, are computed at the center-point nodes (\cdot).

2.6.7 Courant Number

The Courant number is an important non-dimensional parameter in CFD. It is defined [15, p. 70] as

$$C = \left| \frac{\vec{u}\Delta t}{\Delta x} \right|. \quad (2.142)$$

The Courant number is a parameter describing about how fast information is allowed to propagate in a system. If the Courant number is too high, information

may spread too quickly, which may result in unphysical results or no convergence of the problem. The maximum allowable value of the Courant number depends on the method used to solve the discretized problem. Explicit solvers typically requires $C_{\max} \leq 1$, but implicit solvers, like KFX, tolerates higher values while still maintaining convergence.

The KFX Manual [35] gives guidelines regarding choice of Courant number. For pool fires, this has been found empirically to have a value of $C_{\max} \leq 5$ with a recommended value of $C_{\max} = 2$. A Courant number of 2 was used for the majority of simulations performed in this thesis.

2.6.8 SIMPLEC Algorithm

KFX uses the SIMPLEC algorithm, a solution algorithm for the FVM where the idea is to correct a preliminary guess for the pressure and velocity fields such that the continuity equation is fulfilled. The pressure and velocities are decoupled in the following way:

$$p = p^* + p' \quad (2.143a)$$

$$u = u^* + u' \quad (2.143b)$$

$$v = v^* + u' \quad (2.143c)$$

where * indicates the preliminary guess, and the correction, denoted by ', is the difference between correct value the preliminary guess.

SIMPLEC is an acronym for *Semi Implicit Method for Pressure Linked Equations - Consistent*, and the general solution procedure is [36, pp. 148-150]:

0. Specify boundary conditions and guess or use initial values from previous time step.
1. Calculate pseudo-velocities.
2. Solve the momentum equations to determine u^* and v^* for the next time step.
3. Solve the equation for p' .
4. Correct the preliminary velocities and pressure, using under-relaxation if necessary.
5. Repeat from point 2 until convergence.
6. Solve equations for all the other scalar quantities.
7. Execute necessary corrections between each time step for quantities ϕ .
8. Repeat from point 2 for the new time step.

3 The Phoenix Series Large Scale LNG Pool Fire Experiments

Prior to the large scale LNG experiments by Sandia National Laboratories (SNL) in 2009, few to none experimental LNG pool fires of this size had been conducted. Consequently, there are knowledge gaps for very large LNG pool fires. Typical topics regarding LNG pool fires include the duration time, maximum and average flame size and surface emissive power (SEP) as a function of the pool diameter. These are some of the topics regarding safety engineering in need of quantitative (and qualitative) knowledge. To address some of these issues, the Phoenix series large scale LNG pool fire experiments were conducted in Albuquerque, New Mexico, USA in 2009.

Two large scale LNG tests were completed [3]; LNG Test 1 with a circular pool spreading diameter of 23 m, and LNG Test 2 with a circular pool spreading diameter of 83 m. Short videos describing the background of the experiments, setup, goals and some analysis are given as links in App. B.1.

As the larger LNG Test 2 was the one investigated, detailed results will be presented from this only. Key results from LNG Test 1 are briefly mentioned.

3.1 Experimental Setup

The experiments were conducted in relatively flat terrain in the New Mexico desert. A large pond was excavated for containing the water pool approximately 120 meters in diameter. The LNG was kept in a large elevated reservoir and released onto the water through three concrete pipes from the reservoir to the center of the water pool, which can be seen in Fig. 3.1. The LNG was approximated as liquid methane (>99.5%). Methane was used to minimize the potential for explosive rapid phase transitions (RPTs) and to minimize general uncertainty parameters associated with multicomponent liquids. Previously conducted LNG fire experiments with typical LNG composition have shown [2] that the methane is the first component to burn off, with little to no involvement of the heavier hydrocarbons until late in the test, so liquid methane was considered a good approximation to the typical multicomponent mixture of LNG. The depth of the pool was shallow compared to the circular diameter (~ 2 m deep, 120 m across), to minimize convective effects in the water.



Figure 3.1: Overhead view of the experimental setup. N indicates magnetic north. From [3].

3.2 Pool Spreading and Area

Determination of spreading pool area (and effective diameter) of the LNG was done by still images extracted at certain times by overhead videos shot from helicopters. An image processing software was used to determine the LNG spreading area by comparing two images at identical times from two different angles. An example can be seen in Fig. 3.2. A curve fitting tool was then used to get a time series of the pool area (see Fig. A.1). The average pool area was determined from images at 240 s, 270 s and 310 s, and was found to be $5392 \pm 517 \text{ m}^2$, equivalent to a circular diameter of $82.9 \pm 26 \text{ m}$. This averaging interval was later used to determine various quantities, such as steady-state plume heat flux and quasi-steady burn rate.

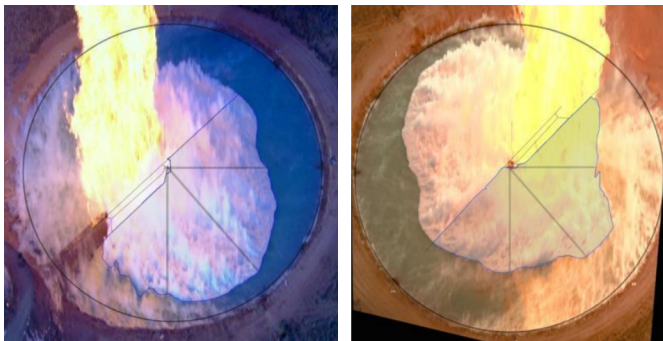


Figure 3.2: Aerial stills of the LNG pool at 240 s. From [3].

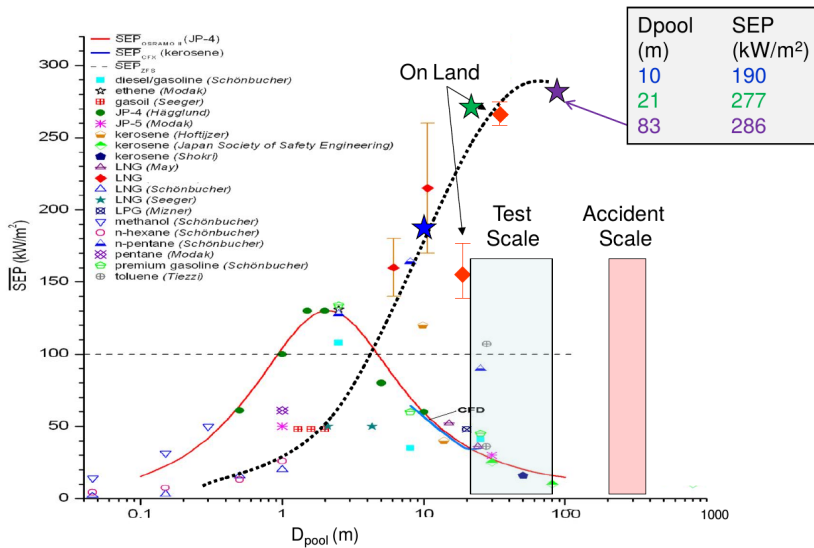


Figure 3.3: Average SEP for various LNG pool fire experiments. LNG Test 1 and 2 in green and purple, respectively. From [3].

3.3 Radiative Heat Flux and Surface Emissive Power

Another key aspect to the report by Blanchat et al. [3] was the surface emissive power (SEP) of the flames. To correctly be able to predict hazard zones around an accident, knowledge about the SEP as a function of pool diameter is important. The data obtained from the experiments were in agreement with existing theory. Various values for the SEP as a function of pool diameter obtained from different experiments can be seen in Fig. 3.3, plotted on a semi-logarithmic axis. The two experiments (the green and purple stars) fit nicely into the assumed trend of average SEP as a function of diameter for LNG pool fires, where the SEP rises sharply from a pool diameter of about 1 meter, reaches a maximum at a diameter of about 60 meters, then declines somewhat. This indicates that for LNG pool fires with a diameter of ~100 meters, an average SEP of ~286 kW/m² is to be expected. To further predict and verify this curve, more large-scale testing is needed.

In both tests, the SEP was measured using wide-angle (or wide-view) radiometers mounted on small towers on four principal axes, or spokes, around the pool, with three towers per spoke, totaling 12 towers. The towers can be seen as small dots forming an axis cross around the pool in Fig. 3.1. These radiometers were combined with high-speed video cameras filming the flames over the duration of the fire. In the post-processing of the experiments, advanced image processing was used. Each frame from the high-speed cameras was filtered with a red threshold of the spectral analysis to account for the number pixels determined to

be «fire» [3]. This was then inserted into the equation

$$E_{\text{source}} = \frac{q_{\text{sensor}}}{\alpha_{\text{sensor}} \frac{1}{\pi} \int_{\Omega_{\text{source}}} \cos \theta d\Omega}. \quad (3.1)$$

Here, E_{source} is the SEP of the flame, α_{sensor} is the absorptivity of the radiometer, q_{sensor} is the measured heat flux by the radiometer, Ω_{source} is the solid angle of the radiation source (e.g. the flame) as seen from the radiometer and θ is the angle between the surface normal of the radiometer and the incident radiation. The integral in Eq. (3.1) had to be determined by the image processing. This was approximated as

$$\int_{\Omega_{\text{source}}} \cos \theta d\Omega \approx \sum_{\substack{\text{pixels} \\ \text{in source}}} \cos \theta \frac{\cos \phi dA_{\text{pixel}}}{S^2}, \quad (3.2)$$

where dA_{pixel} is the area of each pixel, S is the distance from the radiometer to the pixel, and ϕ is the angle between the surface normal of the image and the ray from the pixel to the radiometer. The flame was approximated to lie uniformly on the image plane. See Fig. A.2 for reference.

3.4 Uncertainties and Errors

Any experiment has a degree of uncertainty for measurements, and these uncertainties usually increases as the experiment grows in size and complexity. The main comparisons between the KFX simulations and Phoenix experiment in this thesis, are the radiative heat fluxes, pool spreading and flame morphology, all with individual inherent uncertainties.

The radiometers measuring the radiative heat fluxes are given with a measurement uncertainty by factoring in the uncertainty the radiometers and calibration uncertainty, and is given [3] as $\pm 3\%$ of the measured heat fluxes. In addition to this, averaging unsteady data series produces a statistical error for for the averaging, which can be somewhat quantified by computing the standard deviations.

Values for the error for the average SEP and flow rate in Table 3.1 are given by Blanchat et al. [3], but their derivation are not explained.

An uncertainty factor in the pool spreading analysis of the Phoenix experiment lies in the videos shot from overhead helicopters, from which still images were extracted to estimate the pool area, as described in Sec. 3.2. These images were extracted every 30 s, giving a possibility of sampling error. Additionally, as the pool fire evolved, the LNG vapor obscured the edges of the pool, complicating the analysis of the instantaneous pool area. The average pool area (and equivalent circular diameters) was found by averaging over the pool areas at 240 s, 270 s and 300 s, again producing an averaging error.

Quantities regarding the flame morphology were found in video analysis, by

one high-speed camera for each spoke. When computing these quantities, i.e. the centroid, the three-dimensional flame was mapped onto a two-dimensional plane, producing an error for the measurements of the distances from each camera to the centroid, as the flame would be closer to the camera at its center, but further away at the edges. In the two-dimensional mapping, this error is not included.

A source of error for the experiment is the LNG mass flow rate. The mass flow was computed by measuring the height reduction of LNG in the reservoir by use of laser measurements. A number of uncertainties are listed [3]:

1. Uncertainties in the laser measurements from which the relationship of radius to height is derived
2. Uncertainties that arise from data manipulation (a coordinate system transformation which identifies the central axis of the reservoir)
3. Uncertainties due to representing the mean square radius as a function of height with a curve fit through a collection of data points
4. Uncertainty due to possible mismatch in coordinate system zero between liquid height measurements and the reservoir model curve fit
5. Inherent uncertainty in the liquid height measurements due to gage uncertainty
6. Changes in reservoir from time of measurements to time of test

The uncertainties concerning the laser measurements are assumed to be negligible compared to the other sources of error. An additional source of error occurs when approximating this LNG mass release, plotted on the same x -axis as the pool area in Fig. A.1, for implementation as a time-dependent boundary condition in KFX.

Except for the measurement uncertainty for the radiometers, none of these uncertainties are quantified to any particular degree. Rather complicated and elaborate uncertainty analyses of other aspects investigated in the Phoenix experiment, such as spectral analysis of the flame, are detailed. However, as none of these other aspects are included for comparison with the simulations, they will not be discussed here.

3.5 Key Results

The two tests, Test 1 and Test 2, had LNG spreading diameters of about 21 meters and 83 meters, respectively, on top of the water pool. Some key data from the two tests is presented in Table 3.1. A blank space [-] means that no data were collected or given in the report, for various reasons. An interesting result from the experiments was that the diameter of fire was not equal to the spreading diameter of the LNG, and instead attached to the pipe outlet, suggesting that for an open-water LNG fire with both very light and strong crosswinds, the flame will anchor itself to, say, the ship from which the LNG is leaked [2].

Table 3.1: Key data from LNG Test 1 and LNG Test 2

	Test 1	Test 2
LNG spreading pool diameter (D) [m]	21	83
Volume discharge [m ³]	58.0	198.5
Flow rate, initial [m ³ /s]	0.061	–
Flow rate, end [m ³ /s]	0.123	–
Flow rate during fully open period ^a [m ³ /s]	0.121	1.91±0.84
Total discharge time [s]	510	144
Avg. mass discharge [kg/s]	50.8	802
Avg. wind speed [m/s]	4.8	1.6
Avg. wind direction [°]	331	324
Avg. length (L) of flame (horizontal) [m]	70	0
Avg. height (H) of flame (vertical) [m]	34	146
Avg. tilt angle of flame [°]	50	0
Avg. plume width (W) at height $z = 15$ m [m]	-	56
L/D ratio	3.4	0
H/D ratio	1.6	1.7
H/W ratio	-	2.6
Avg. overall SEP [kW/m ²]	277± 60 (2 σ)	286 ± 20(2 σ)

^aThe fully open period does not refer to the quasi-steady period referred to in Ch. 4. The fully open period refers to the period for which the LNG was flowing freely from the reservoir with fully open discharge pipes. The quasi-steady period refers to the period when the flame was neither rapidly increasing nor rapidly decreasing in size.

4 Simulations - Radiative Heat Fluxes

4.1 Initial Work and Basis for the Thesis

As a continuation of previous work [31], LNG Test 2 was chosen for further comparison of simulated and experimental results. A key point in the report by Blanchat [2] was the SEP of the fire. However, as this would be problematic to directly compare to the KFX simulations due to the advanced image processing done by Sandia National Laboratories (SNL), see Sec. 3.3, the directly measured radiative heat fluxes were chosen for comparison, e.g. q_{sensor} in Eq. (3.1).

When simulated as a constant release of gaseous methane from a circular, 83 m diameter pool with a constant vaporization rate of $0.147 \text{ kg/m}^2\text{s}$, it was found that the radiative heat fluxes measured in the experiment was of magnitude two to four times higher than the values computed in KFX [31]. Table 4.1 summarizes these results. A number of reasons to explain this difference in heat flux were proposed, and included (1) effect of flame anchoring to the discharge pipes; (2) effect of soot shielding; (3) effect of soot particles inside the flame; (4) setup of simulation case; (5) erroneous physical models in KFX; (6) effect of water vapor; and (7) sampling error.

Item 7 was promptly investigated and ruled out. However, the others needed more investigation, and items 1, 2 and 4 were, after discussion with supervisors, considered the most probable causes of this difference in heat flux.

4.2 Simulation Setup

Several different simulations scenarios were considered. Five main scenarios were chosen. For all, the CAD geometry in App. A.3 was used, unless otherwise stated. The five main scenarios initially simulated were

- Transient release of gaseous methane, with minimal relevant geometry;
- Constant release of gaseous methane;
- Transient release of gaseous methane;
- Constant release of liquid methane; and
- Transient release of liquid methane.

Table 4.1: Incident heat fluxes in kW/m² obtained in the project thesis [31]. The lengths indicate the distance from the pool center to the location the heat fluxes were measured. The standard deviation of the data over the averaging interval for the experiment are also given.

	North		East		South		West		Mean	
	SNL	KFX	SNL	KFX	SNL	KFX	SNL	KFX	SNL	KFX
110 m	20.9	9.9	–	10.0	39.4	8.9	20.6	8.1	26.1 ^a	9.2
<i>st.dev.</i>	1.6		–		3.4		1.9			
160 m	12.6	6.0	13.3	5.9	20.8	5.5	12.1	6.0	14.7	5.9
<i>st.dev.</i>	0.9		1.2		1.8		1.4			
210 m	8.4	3.7	8.6	4.0	13.3	3.8	7.7	3.4	9.5	3.7
<i>st.dev.</i>	0.6		0.7		1.2		0.8			

^aAs the 110 m tower on the east spoke failed to record, this mean is based on multiplying the 160 m and 210 m east spoke heat fluxes with the averaged ratio of the 110 m/160 m and 110 m/210 m heat fluxes from the other spokes. In both cases, the 110 m east spoke heat flux calculates to 23.3 kW/m².

Variations of these scenarios were also simulated, using various parameters and initial and boundary conditions.

Logging the heat flux in KFX was done by placing logging tools, called bullet monitors, in the calculation domain in a similar fashion to the instrument towers from the experiment. In addition to spatial location, the bullet monitors needs a specification of the direction to measure the heat fluxes in vectorial form. This was done by setting an option where the bullet monitors automatically detects the direction of maximum heat flux, and uses this as the normal vector. The x - and y -axes in the calculation domain coincided with the east-west and north-south axes from the experiment, with positive y being north and positive x being east. A schematic arrangement of the experimental setup, with water pool enclosure and instrumentation towers can be seen in Fig. 4.1. The towers, named T1, T2 and T3, were placed 110 m, 160 m and 210 m from the pool center, respectively.

Initial and boundary conditions included the wind speed and direction, air temperature, and temperature for the LNG and water pools (when used). The wind was set to 2 m/s with an clockwise angle of 344° from the positive y -axis. This was somewhat more than the experiment to adjust for the wind fluctuations in the experiment. The direction of the wind is also somewhat different to account for the fact that the «north» spoke did not directly align with magnetic north, from which the wind was measured. Ambient air temperature was set to -1°C, water pool temperature to 1°C, ground temperature to 1°C and liquid methane temperature to 111 K, to match the experimental conditions. In the case of a constant release, the release rate was 800 kg/s for both the liquid and gaseous releases. For the transient releases, the mass flow from Fig. A.1 was approximated as the mass flow seen in Fig. 4.2. By this approximation, a total of 81428 kg methane was released, and with a liquid methane density of 420 kg/m³, this would give a total release

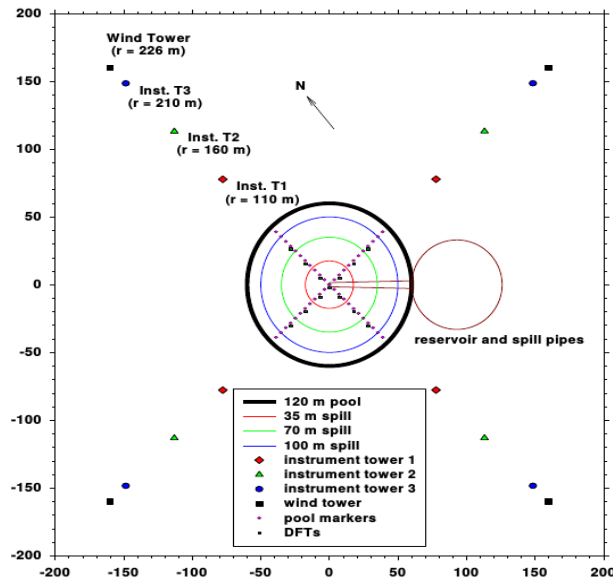


Figure 4.1: Location of the instrument towers in the LNG experiments. From [3]. The wind towers were used for wind measurements and for calibration purposed only.

of 193.9 m^3 liquid methane. Compared to the total volume discharge from Table 3.1, this is only about 2% less than the total LNG release in the experiment, so the approximation was thought to be reasonable. Note that the time $t = 0 \text{ s}$ in the simulations corresponds to $t = 100 \text{ s}$ from the experiment.

Due to limitations in the multicomponent pool model in KFX, the liquid releases were simulated as released on a flat surface, with various heat transfer coefficients to account for the heat transfer from the water to the LNG. The literature on the heat transfer coefficient between cryogenic liquids and water varies greatly. Various experimental data is summarized by Woodward and Pitblado [37, p. 146], and values for liquid methane on water are listed as between $149 \text{ W/m}^2\text{K}$ and $683 \text{ W/m}^2\text{K}$.

4.3 Numerical Solvers, Convergence and Grid Resolution

For all simulations, the SIMPLEC algorithm (see Sec. 2.6.8) are used for the computations. The transport equations are solved by the QTDMA (quadratic tri-diagonal matrix algorithm) solver, and the STONE (Stone strongly implicit) solver are used for the pressure correction equations and pressure equations. These solvers are iterated until convergence for each time step.

The equations for the pressure and pressure corrections are numerically the

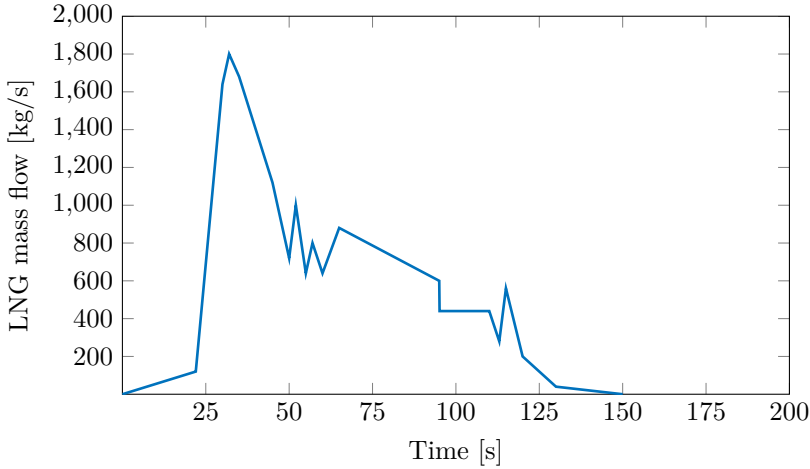


Figure 4.2: Approximated LNG mass flow rate used in simulations.

most demanding computations, as the pressure correction equation must be solved accurately for global conservation of mass. In theory, these equations should be iterated until the residuals, that is, the numerical errors, are zero. However, as this diverges the computational time to infinity, the maximum number of iterations are set to 100 for the pressure and pressure correction equations, with a convergence criterion of 10^{-4} for the ratio of the ingoing and outgoing residuals. A maximum number of iterations for the energy and species equations are set to 4. When the convergence criterion for one time step is met, the next time step is initiated.

Given the very large scale of the simulation scenario, the grid resolution needs to be a compromise between accuracy and computational efficiency. Unless otherwise noted, all simulations were performed in a domain spanning from -220 m to 220 m in the x - and y -directions and 0 m to 400 m in the z -direction, with 183 nodes in the x - and y -directions and 90 nodes in the z -direction, totaling 3014010 nodes. The grid was non-uniform, equal in x - and y -directions, and symmetrical over the x - and y -axes, with the origin being in the middle of the pool center. The finest grid resolutions were directly above the pool enclosure, and at lower altitudes along the z -axis. Fig. A.4 shows the full grid distribution in the x - y plane, Fig. A.5 shows the grid distribution zoomed in on the pool enclosure. Fig. A.6 shows a graphical representation of the grid distribution in the z -direction.

4.4 Initial Simulations and Radiative Heat Fluxes

Eight initial simulations were performed, with different initial and boundary conditions and parameters. The variations are shown in Table 4.2. The results for the radiative heat fluxes are shown in Table 4.3. The averaging intervals for the

Table 4.2: Overview of the initial simulations performed. *Surrounding water pool* means whether there was a water pool in the surrounding «ring». The *geometry* entry is whether any relevant geometry (pipes leading into the pool and reservoir) were included. *Leak time* is the initial spreading time of the water pool before the simulation was started. *Hc-ground* is the forced heat transfer coefficient between the ground and liquid pool(s).

Name	Gas/ liquid	Water pool	Constant/ transient	Geometry	Leak time	Hc-ground	Courant number	Averaging interval	Comment/ <i>other</i>
case1	Gas	Yes	Transient	No	0 s	0 W/m ² K	2	30 s – 130 s	
sim1	Gas	Yes	Transient	No	0 s	0 W/m ² K	2	30 s – 130 s	1
sim3	Gas	Yes	Transient	Yes	0 s	0 W/m ² K	2	30 s – 130 s	
sim6	Liquid	Yes	Constant	Yes	60 s	0 W/m ² K	2	60 s – 160 s	
sim7	Liquid	Yes	Constant	Yes	0 s	0 W/m ² K	2	60 s – 130 s	
sim8	Liquid	Yes	Transient	Yes	0 s	0 W/m ² K	2	60 s – 130 s	
sim9	Liquid	No	Transient	Yes	0 s	0 W/m ² K	2	60 s – 130 s	
sim10	Liquid	No	Transient	Yes	0 s	500 W/m ² K	2	30 s – 130 s	

¹ Different type of release cells than case1

Table 4.3: Incident heat flux in kW/m² from the initial simulations.

		N	E	S	W	Mean		N	E	S	W	Mean
110 m	case1	9.26	8.23	8.18	8.27	8.49	sim1	9.00	8.26	8.08	8.32	8.42
160 m		5.60	4.73	4.88	4.92	5.03		5.58	4.79	4.81	4.96	5.04
210 m		3.69	3.18	3.35	3.38	3.40		3.59	3.22	3.32	3.39	3.38
110 m	sim3	9.50	8.87	8.92	8.89	9.05	sim6	6.67	6.19	6.69	9.05	7.15
160 m		5.96	4.69	5.21	5.01	5.22		4.16	3.77	4.03	5.49	4.36
210 m		4.24	3.20	3.52	3.47	3.61		2.84	2.57	2.67	3.65	2.93
110 m	sim7	7.20	7.47	6.72	9.46	7.71	sim8	6.15	7.45	6.41	8.74	7.19
160 m		4.52	4.46	3.98	5.50	4.61		3.89	4.41	3.63	5.05	4.24
210 m		3.12	2.98	2.63	3.61	3.09		2.70	2.93	2.38	3.32	2.83
110 m	sim9	6.23	7.21	6.76	7.07	6.82	sim10	8.62	9.79	9.46	11.3	9.78
160 m		3.96	4.44	3.89	4.12	4.10		5.56	5.91	5.65	6.67	5.95
210 m		2.77	3.01	2.58	2.76	2.78		3.93	4.00	3.77	4.47	4.04

heat fluxes were chosen for a time period considered sufficiently long where the heat fluxes were relatively steady. Evidently, when comparing to the heat fluxes from the experiment in Table 4.1, these fluxes are still too low by a factor of between two and four, and well outside the standard deviations. There were only minor differences between the simulations with and without geometry, i.e. with or without the discharge pipes as part of the CAD model. However, the gaseous releases gave, on average, an incident heat flux of about 1 kW/m² more than the liquid releases for the 110 m monitors, 0.4 kW/m² for the 160 m monitors and 0.3 kW/m² for the 210 m monitors. sim10 included a forced heat transfer coefficient between the LNG pool and the ground beneath. This gave a rather large «peak» of radiation release at the beginning of the averaging interval due to a rapid vaporization of liquid methane giving a much larger flame for a short period of time. This contributed to the higher averaged heat fluxes seen, especially on the south spoke. The liquid releases gave less volatile, but unsteadier heat fluxes compared to the gaseous releases, even in the case of a constant liquid release and a transient gaseous release. Refer to Figs. 4.3 and 4.4 for comparison.

Fig. 4.3 is the time series of the heat fluxes from sim1, a gaseous, transient release, while Fig. 4.4 is the time series of the heat fluxes from sim10, a liquid, transient release, with a forced heat transfer coefficient to the LNG of 500 W/m²K, opposed to a heat transfer coefficient of 0 W/m²K for sim1. The other differences between these two simulations, is the surrounding water pool for sim1 and no surrounding water pool for sim10, and the inclusion of the discharge pipes in the CAD model in sim10. By investigating the time series of each simulation, sim1 through sim10, these differences were qualitatively explained. The largest factor separating Figs. 4.3 and 4.4 are the fluctuations over the near-steady interval of 30 s to 130 s for both sim1 and sim10, for which the heat fluxes were averaged.

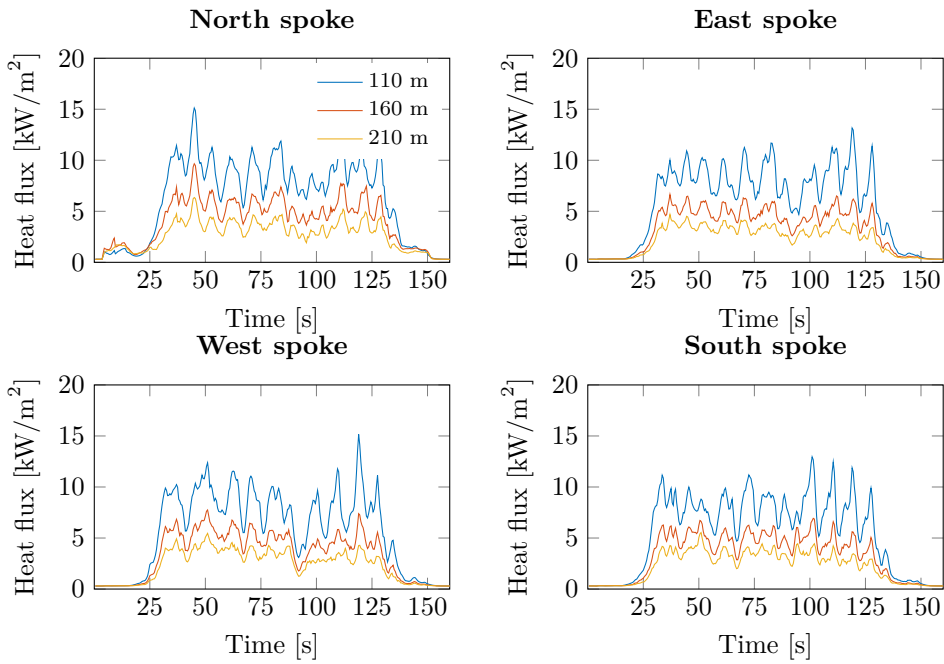


Figure 4.3: Time series of heat fluxes from sim1. Transient release of gaseous methane.

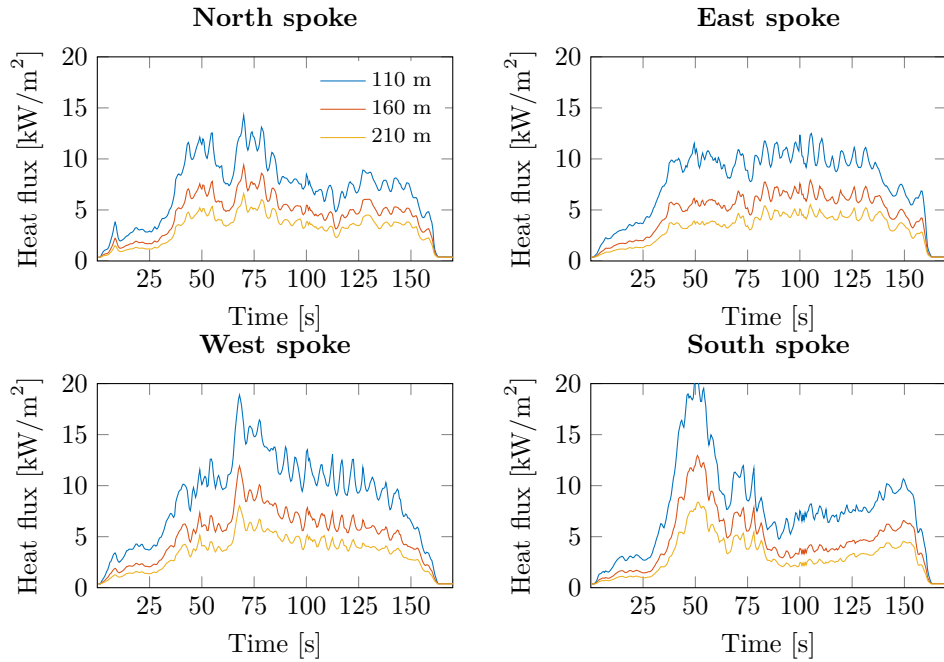


Figure 4.4: Time series of heat fluxes from sim10. Transient release of liquid methane.

All of the gaseous simulations had rather large, distinct fluctuations in the heat fluxes, with a frequency of approximately $1/10 \text{ s}^{-1}$. The liquid simulations all had fluctuations with lower amplitudes but far more frequent. The inclusion of the discharge pipes in the CAD model appeared to dampen the amplitudes somewhat, while maintaining a similar frequency. The influence of the surrounding water pool on the heat fluxes were negligible. As noted, the heat transfer coefficient in sim10 gave a rapid vaporization of LNG at the start of the simulation, most evident on the south spoke. This heat transfer coefficient increased the overall heat fluxes of about 10% compared to the other liquid releases.

Flame anchoring and effect of surrounding water pool were also investigated, but neither appeared to influence the simulations in any major way. The evaporation rate of the surrounding water (in kg/s) was of order 10 larger from the liquid releases than the gaseous releases, likely due to the center of the flame being closer to the ground. Flame anchoring in any form was not seen in any of these simulations.

The remaining factor most likely to dampen the radiative heat fluxes was the effect of soot shielding. To investigate this, a *volume texture rendering* image was produced. The KFX User Manual [35] describes volume texture rendering as a visual representation of the fire produced from a file «that contains four field variables, the first three is color scale and the last is the alpha variable, which is a representation of the local visual length in each control volume». The soot concentration is included in the alpha variable. When rendering a volume texture image, an opacity variable needs to be specified, which is a number between 0 and 1, and accounts for the opacity of the fire and soot. An opacity value of 0.5 was found to be appropriate.

Fig. 4.5 shows sim6 at about 30 s into the simulation. Evidently, the concentration of soot outside and above the flame was very high, especially downwind in the south-southeast direction. This was thought to be the main contributing factor to the lower radiative heat fluxes, and, when reviewing Table 4.3, likely accounts for the lower heat fluxes in the south and east directions, even though the flame was dragged to the south-southeast by the wind.

KFX includes a function called *Tcut(K) for absorption*. This function controls the absorption of radiation by gaseous species and soot by setting a temperature criterion, one for the gaseous species and one for soot. Below the given temperature criterion, absorption and emission of radiation is turned off. The default values are 1100 K for CO_2 and H_2O and 0 K for soot. A new simulation, sim11, based on sim3, was performed, with a *Tcut* of soot at 1100 K, to investigate whether the high concentrations of relatively cold soot outside the flame had any influence on radiation release from the flame, and to which extent. Additionally, in the post-processing, the function for extracting bullet monitor data includes an option which accounts for air humidity, by dampening the radiation by absorption due to water vapor in the atmosphere. The air humidity was set to 59 %, similar to the given atmospheric data in the Phoenix experiment [3]. The time series for the heat fluxes from this simulation are seen in Fig. 4.6.

The faint, dotted curves are the heat fluxes before the humidity option was activated. The values with this option are of magnitude of 0.8 to 0.9 compared

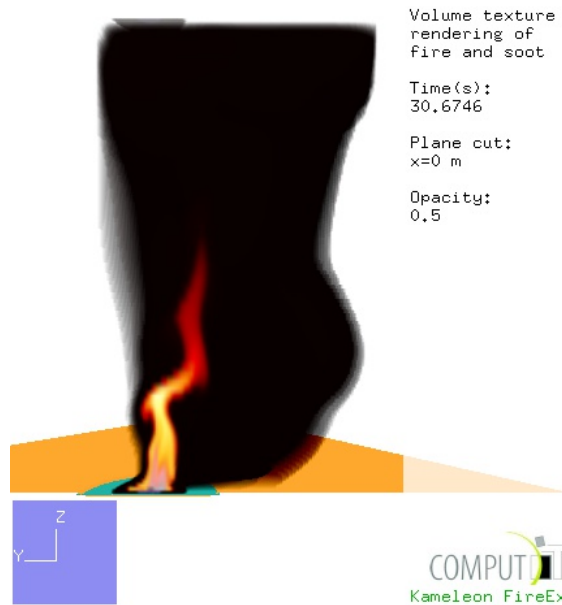


Figure 4.5: Volume texture rendering of sim6 at $t \approx 30$ s. Both the CAD import and flame and soot rendering was cut in the plane $x = 0$ m. Positive y - and z -directions are indicated. Positive x -direction is into the image plane.

to the radiative heat fluxes without this option. The measured values for the radiative heat fluxes in the experiment in Table 4.1 are corrected for atmospheric transmission loss (air humidity and a custom desert aerosol model) [3]. Thus, when using the humidity option in KFX, the *uncorrected* heat fluxes from the experiment, e.g. the ones directly measured, needs to be given for comparison. Averaging the radiative heat fluxes from sim11 in the interval 30 s – 100 s, and using the uncorrected values from the experiment, the values in Table 4.4 is obtained. Similar to Table 4.1, the mean ratios of the 110 m/160 m and 110 m/210 m heat fluxes for the other three spokes were used to quantitatively estimate the 110 m heat flux on the east spoke.

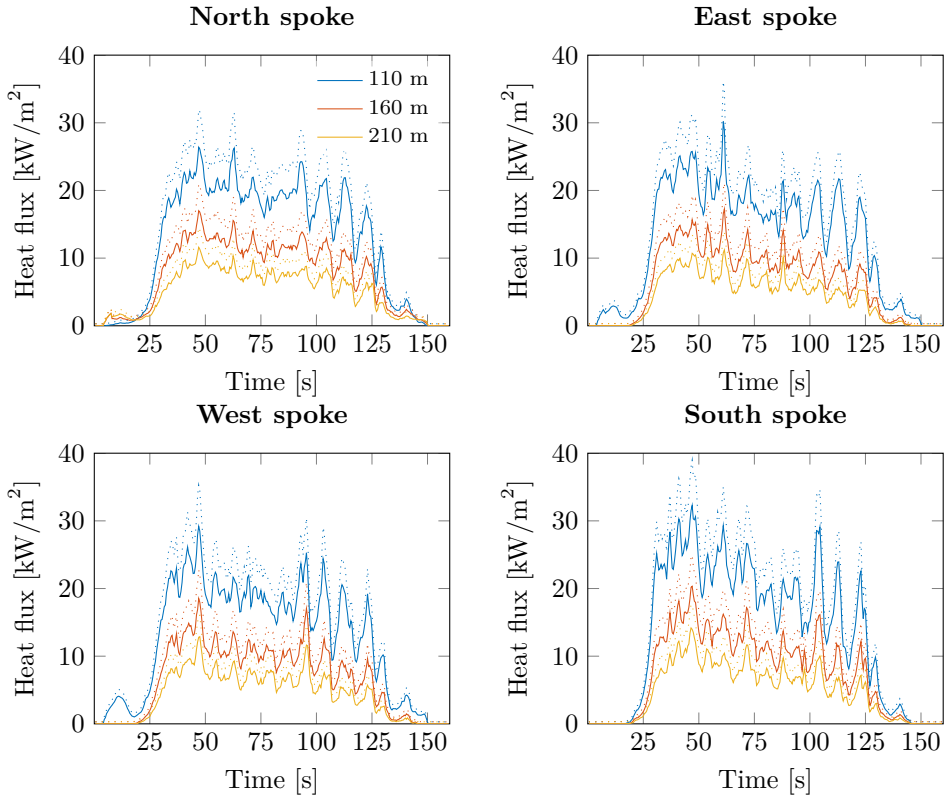


Figure 4.6: Time series of heat fluxes from sim11. Transient release of gaseous methane. $T_{cut}(\text{soot}) = 1100$ K. Solid lines: with humidity correction. Dotted lines: without humidity correction.

Table 4.4: Average radiative heat flux in kW/m^2 obtained in sim11 compared to experimental values. The standard deviation of the data over the averaging interval for the experiment are also given.

	North		East		South		West		Mean	
	SNL	KFX	SNL	KFX	SNL	KFX	SNL	KFX	SNL	KFX
110 m	16.5	19.4	–	19.4	31.5	22.2	18.1	19.6	21.2	20.3
<i>st.dev.</i>	1.2		–		2.7		1.5			
160 m	9.7	12.0	10.1	11.1	16.1	12.8	9.2	11.2	11.3	11.8
<i>st.dev.</i>	0.7		0.9		1.4		1.0			
210 m	6.4	7.85	6.4	7.32	9.9	8.37	5.9	7.38	7.15	7.73
<i>st.dev.</i>	0.4		0.5		0.9		0.6			

Table 4.5: Overview of the simulations performed with the modified soot model. *Surrounding water pool* means whether there was a water pool in the surrounding «ring» or not. The *geometry* entry is whether any relevant geometry (pipes leading into the pool and reservoir) were included. *Bounding* is whether or not there was any physical 83 m boundary limiting the spreading of the LNG pool. *Hc-ground* is the forced heat transfer coefficient between the ground and liquid pool.

Name	Gas/ liquid	Water pool	Constant/ transient	Geometry	Bounding	Hc-ground	Courant number	Averaging interval	Comment/ other
sim14	Liquid	No	Constant	Yes	Yes	0 W/m ² K	2	50 s – 100 s	
sim15	Liquid	No	Constant	Yes	Yes	500 W/m ² K	2	50 s – 100 s	
sim16	Liquid	Yes	Constant	Yes	Yes	0 W/m ² K	2	50 s – 100 s	
sim17	Liquid	No	Transient	Yes	No	0 W/m ² K	2	60 s – 100 s	
sim18	Liquid	No	Transient	Yes	No	500 W/m ² K	2	50 s – 100 s	
sim19	Liquid	No	Transient	Yes	No	100 W/m ² K	2	60 s – 100 s	
sim20	Liquid	No	Transient	Yes	No	300 W/m ² K	2	50 s – 90 s	
sim22	Liquid	No	Transient	Yes	No	0 W/m ² K	2	60 s – 100 s	²

² Absorptivity of LNG pool set to 0.8

4.5 Radiative Heat Fluxes with Modified Soot Model

Evidently, the results in Table 4.4 are a much closer fit to the experiment than the previous results, indicating that the soot model was the reason for the lower radiative heat fluxes previously obtained. The EDC soot model in KFX includes a criterion, deactivating the terms for combustion of soot in areas where no soot is formed. This criterion was turned off, such that more soot could be combusted in the vicinity of the flame, decreasing the soot concentration in these areas. A number of simulations were performed with this modified soot model. These are summarized in Table 4.5.

The majority of these simulations were performed with no surrounding water pool, as the effect of this was found to be negligible, while contributing to the total calculation time. The initial leak time was thus set to zero for all simulations, which is why it is not included in Table 4.5. A new column, *bounding*, is included, and refers to the physical boundary used to limit the maximum LNG pool diameter of 83 m in both the constant and transient releases, and to separate the LNG from the water pool for sim16, when a water pool was present. This bounding can be seen as a thin ring in the pool enclosure in Fig. A.3.

The results for the radiative heat fluxes from these simulations are seen in Table 4.6. When comparing to the initial simulations with Table 4.3, it is evident that these are a much better fit to the experimental values in Table 4.4, and several of these simulations have values within the standard deviation range of the heat fluxes from the experiment. The simulations with a forced *Hc-ground* of 500 W/m²K, sim15 and sim18, gave too high averaged heat fluxes, particularly on the north, east and west spokes. Additionally, sim18, with a transient release with a forced

Table 4.6: Incident heat flux in kW/m² from the simulations with the modified soot model.

		N	E	S	W	Mean			N	E	S	W	Mean
110 m	sim14	15.4	16.7	17.9	18.6	17.2	sim15	20.3	24.0	28.4	27.9	25.1	
160 m		9.86	10.0	11.5	11.0	10.6		13.5	15.6	18.6	17.7	16.4	
210 m		6.81	6.68	7.93	7.31	7.18		9.70	10.9	13.1	12.2	11.5	
110 m	sim16	14.6	18.7	20.0	20.8	18.5	sim17	15.9	19.4	25.5	23.5	21.1	
160 m		9.39	11.3	12.6	12.6	11.5		9.79	11.7	15.0	13.5	12.5	
210 m		6.53	7.62	8.56	8.37	7.77		6.59	7.72	9.62	8.60	8.13	
110 m	sim18	18.5	21.8	28.4	23.4	23.0	sim19	15.4	19.7	23.4	22.6	20.3	
160 m		11.3	12.8	17.2	13.6	13.7		9.56	12.1	13.9	13.1	12.2	
210 m		7.52	8.13	11.1	8.72	8.87		6.47	8.00	8.97	8.49	7.98	
110 m	sim20	17.7	20.3	28.0	22.1	22.0	sim22	15.7	20.2	25.6	22.6	21.0	
160 m		10.9	11.9	16.6	12.7	13.0		9.60	12.2	15.1	13.2	12.5	
210 m		7.25	7.70	10.6	8.21	8.45		6.46	8.02	9.67	8.44	8.15	

Hc-ground of $500 \text{ W/m}^2\text{K}$, gave a very high peak in the heat flux values, over 40 kW/m^2 on the south spoke and 30 kW/m^2 on the east spoke, in the time interval 50 s to 70 s, making it difficult to find a suitable averaging interval. This is also true for sim20, with a forced *Hc-ground* of $300 \text{ W/m}^2\text{K}$, however, to a lesser extent.

The constant releases without a forced heat transfer coefficient to the ground, sim14 and sim16, both produced good, relatively comparable results to the experiment. Of these two, only sim16 included a surrounding water pool and gave on average somewhat higher and more fluctuating heat fluxes. It is unclear whether the surrounding water pool caused this, or if this is due to some other effect. Both simulations reached an approximately steady heat flux after about 40 seconds, as sim14 in Fig. 4.7 shows.

Simulations sim17, sim19 and sim22, all transient, unbounded releases, gave very similar results. Fig. 4.8 shows the time series of sim17. Both sim19 and sim22 were variations of sim17, with sim19 having a forced *Hc-ground* of $100 \text{ W/m}^2\text{K}$ (as opposed to zero), and sim22 having a absorptivity coefficient of the liquid methane of 0.8 (as opposed to a value of 1). sim19 gave, somewhat surprisingly, slightly lower heat flux values than the other two. sim22 was only marginally different to sim17, suggesting that the absorptivity coefficient, and thus the evaporation of the pool due to radiative heat transfer from flame, is of secondary importance to the boiling produced by conductive and convective heat transfer from the surrounding gas. However, to make a certain conclusion regarding this, further investigation is needed, something that was not done in the work on this thesis.

None of the simulations performed gave the same magnitude of the heat flux at the 110 m tower on the south spoke as in the experiment, see Fig. 4.6. Only sim18 and sim20 produced comparable values at the 160 m and 210 m tower on the south spoke, but both gave too high values at the other spokes. This is probably due to the effect of flame anchoring, which was prominent in the experiment [3], but was not seen in any of the simulations. This effect can be clearly seen in videos from the Phoenix experiment, i.e. Video C in App. B.1, from 09:28 into the video clip. This caused the base of the flame to be dragged in a 45° angle between the east and south spokes, as the pipes leading the LNG onto the water pool were placed midway between these two spokes. Factoring in the direction of the wind, this was stated as a likely cause of the much higher heat flux obtained on the south spoke [3]. As no such effect was seen in the simulations, this could explain the lower heat fluxes on the south spoke, while making the west and north heat fluxes too high, compared to the experiment.

Similar to the previous soot model, a volume texture image was rendered, to inspect the visual implications of this modified soot model. sim16 was chosen at 30 s into the simulation, and is seen in Fig. 4.9. An equal opacity value and similar view angle to Fig. 4.5, was chosen, to best be able to compare the two images. Comparing to Fig. 4.5, the concentration of soot in the vicinity of the flame is far less, and likely at a more realistic amount, especially upon comparison to videos and images from the Phoenix experiment.

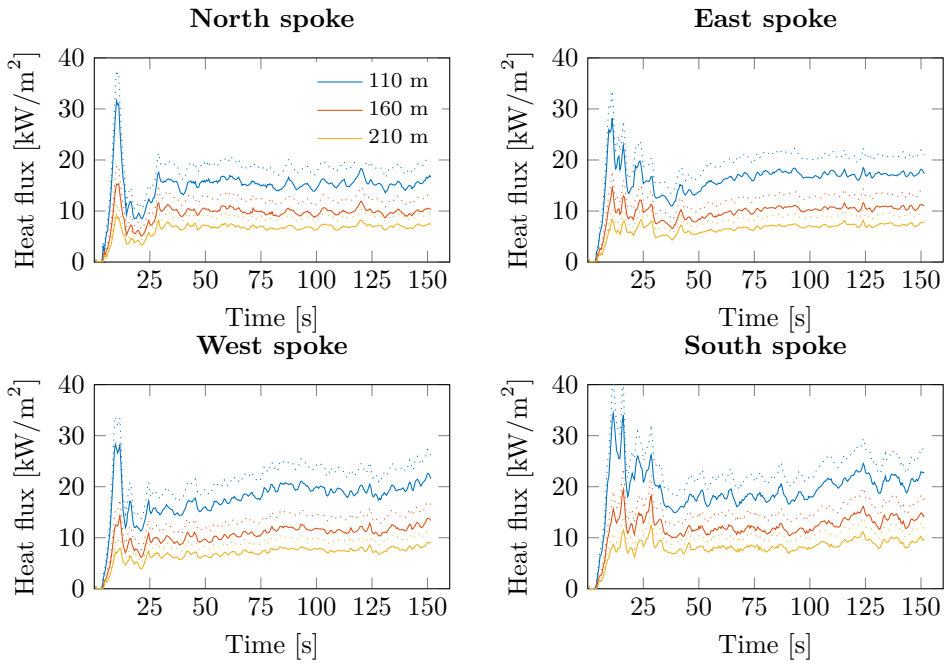


Figure 4.7: Time series of heat fluxes from sim14. Constant release of liquid methane. Solid lines: with humidity option. Dotted lines: without humidity option.

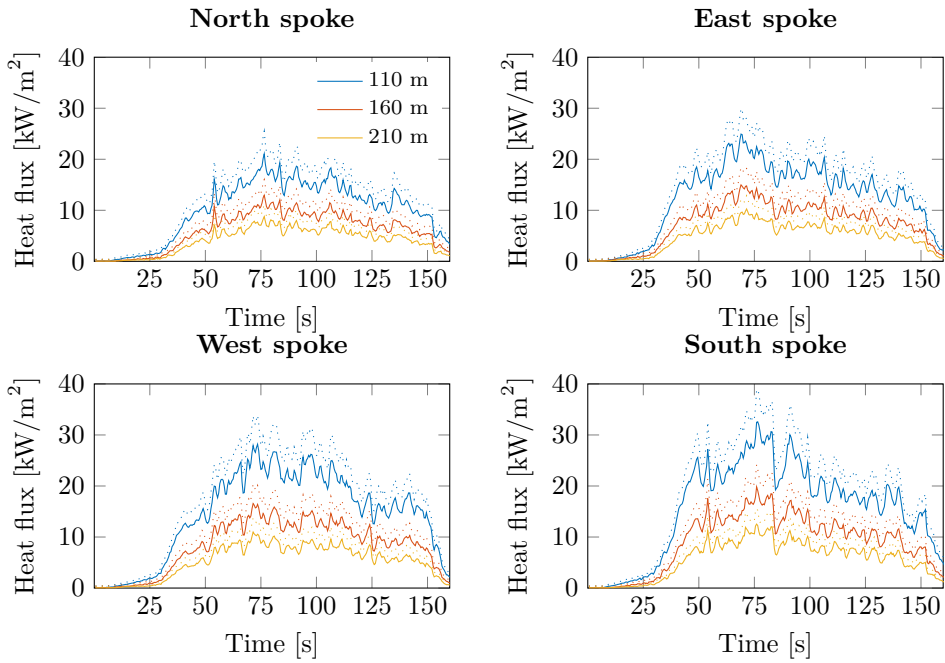


Figure 4.8: Time series of heat fluxes from sim17. Transient release of liquid methane.



Figure 4.9: Volume texture rendering of sim16 at $t \approx 30$ s. Both the CAD import and flame and soot rendering was cut in the plane $x = 0$ m. Uncombusted fuel shows as white. Positive y -axis in the left horizontal direction, positive x -axis into the plane.

5 Simulations - Pool Spreading and Area

5.1 LNG Pool Area

The second of the major investigations in the Phoenix LNG experiment was the pool spreading area and effective diameter. The LNG pool area from the experiment compared to the flow rate can be seen in Fig. A.1. By looking at this, while comparing the heat flux time series from the Phoenix experiments, Fig. A.7 to the heat flux time series obtained in the transient, liquid simulations, e.g. sim17 in Fig. 4.8, it is evident that the fire had a far longer duration in the experiment than the simulations. Fig. A.7 display significant heat fluxes in the time period 100 s to approximately 530 s, having a total duration of about 430 seconds. The LNG spill was over at about 250 s into the test execution, making the LNG pool burn more than 280 s after the LNG reservoir was emptied. As the heat fluxes in the liquid, transient releases all were approximately zero at 170 s, it can be concluded that all fuel had been combusted by then. The LNG spill was over at 150 s¹, making the LNG pool last only about 20 s after the spill ended.

To investigate this, the pool areas from the liquid, unbounded and transient simulations with the modified soot model, sim17, sim18, sim19, sim20 and sim22, were extracted. Additionally, one simulation, sim24, with a Courant number of 5 was performed, to inspect the time step dependence of the simulations. The results are seen in Fig. 5.1. The LNG mass flow is associated with the left y -axis, while the pool areas are associated with the right y -axis. The pool area from the Phoenix experiment is included for reference.

Evidently, none of the simulations had a similar pool area compared to the experiment. Simulations sim17, sim22 and sim24 had a similar maximum area to the Phoenix experiment of about 5300 m², corresponding to a diameter of approximately 82 m, assuming a perfectly circular pool. The pool areas are consistent in decreasing area with increasing heat transfer coefficient to the ground. This makes intuitively sense, as a higher heat transfer coefficient increases the energy transfer to the LNG, making it evaporate at a higher rate, reducing the amount of liquid LNG left in the pool. The simulations with an absorptivity of the LNG of 0.8 and Courant number of 5 showed very little difference to the «benchmark» simulation, sim17, as both curves lie almost directly on top of sim17 in this figure.

¹Remembering that $t = 100$ s in the experiment corresponds to $t = 0$ s in the simulations.

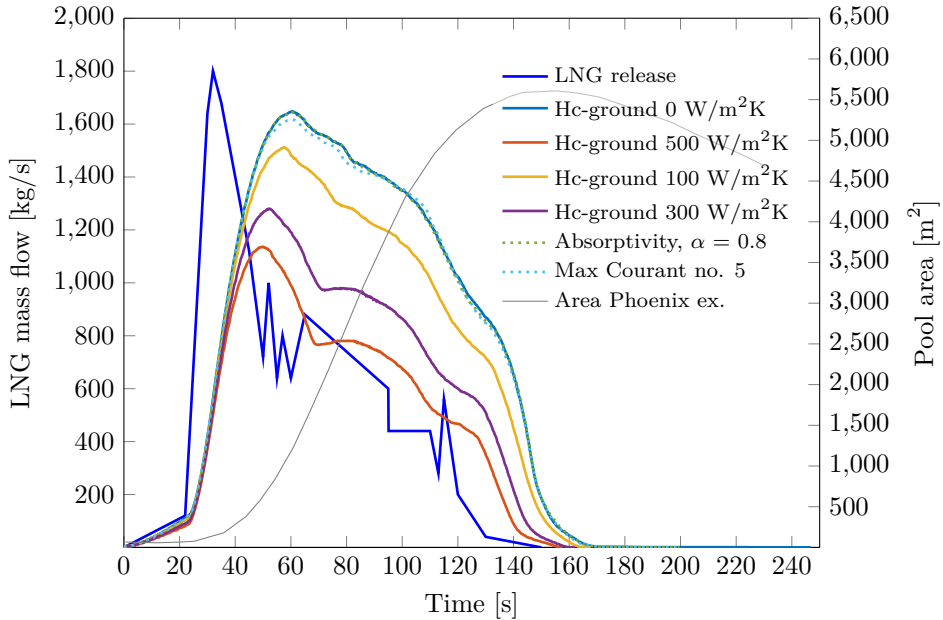


Figure 5.1: LNG mass flow in the simulations and simulated pool areas compared to pool area from the Phoenix experiment.

5.2 Mean Pool Depth

Another quantity provided in KFX is the pool depth. The mean pool depths of a few of the simulations were extracted and can be seen in Fig. 5.2, where the simulations with a pool absorptivity of 0.8 and Courant number of 5 have been omitted due to their close resemblance to the «benchmark» simulation, sim17. Though the pool areas varied quite a lot, the mean pool depths followed a very similar trend and follows the LNG release quite close in shape. A maximum mean depth of approximately 14 mm was seen for all simulations. Some oscillations are seen at the start and end of the simulations, when the pool area was small and mean depth was low. This is due to the pool spreading model implemented in KFX. The liquid pool model is a 2D sub-model lying directly below the free flow calculation domain. It uses the same grid spacing as the x - y plane with a numerical value for the depth in each cell, and as such, it has zero depth in the computational domain. The total area is calculated by summing up the area of each grid cell containing any liquid, implying that when the LNG spreads to a new cell where it instantly evaporates, fluctuations such as in Fig. 5.2 can be experienced.

Unfortunately, there is not provided any data on the pool depth in neither of the Phoenix LNG experiments, so there are no data which to compare the KFX results. This is understandable, as the pool depth would be very difficult to measure for such a large scale experiment.

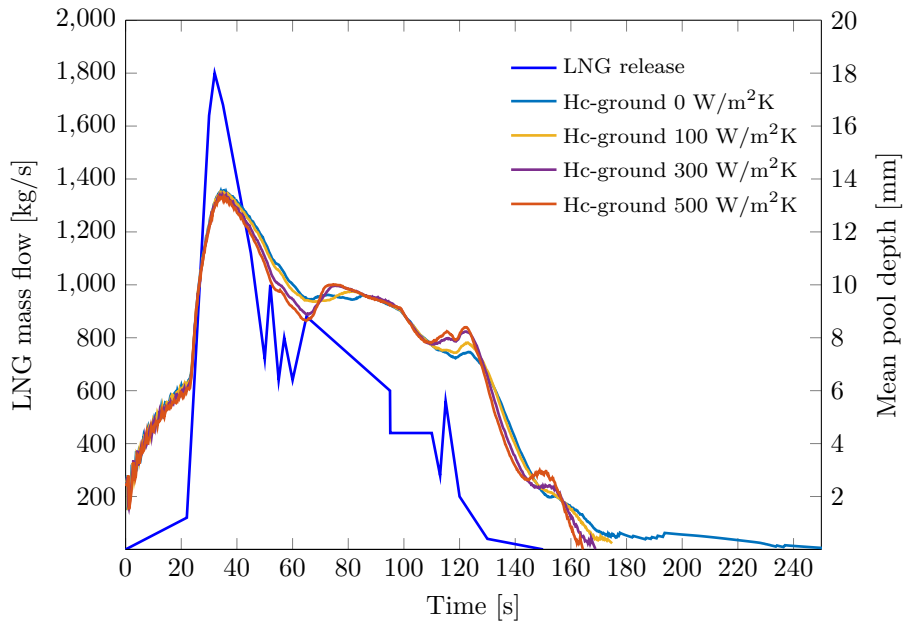


Figure 5.2: LNG mass flow in the simulations and simulated mean pool depths.

5.3 Cross-Sectional Pool Depth

While the data in Fig. 5.2 shows the mean pool depth at each time instance, it does not give any information on the difference in LNG pool depth throughout the domain. The pool could have a nearly uniform depth, or the pool could vary greatly in x - and y -direction. As the pool was nearly circular, a line segment between the points $(0, -50, 0)$ and $(0, 50, 0)$, that is, from one edge of the pool enclosure to the other along the y -axis, containing data for the pool depth in each control volume was extracted from KFX. This was done every 10 s for the simulation sim17. This was then revolved 180 degrees around the origin to produce a near circular profile of the pool depth for each 10-second time step. These can be seen in Figs. 5.3 and 5.4. In these figures, the z -axis, displaying the pool depth, is in mm and is scaled by a factor of 1000 compared to the lower x - and y -axes.

It is evident that the pool depth is non-uniform, and a protruding peak is visible for all time steps. This is most prominent in the time steps leading up to the maximum pool area at 60 s. Up until 40 s, at the time of the maximum mean pool depth, the shape of the pool is steeply increasing, growing from zero at a radius of approximately 30 m to a depth of about 30 mm at the pool center. The steepest shape is found at 30 s, which, rather unsurprisingly, coincides well with the highest growth rate of the pool area, see Fig. 5.1. After the maximum pool area was reached at 60 s, the pool depth had a relatively gradual, linear increase in depth from the edge to the center, opposed to the steep, curved shape seen for

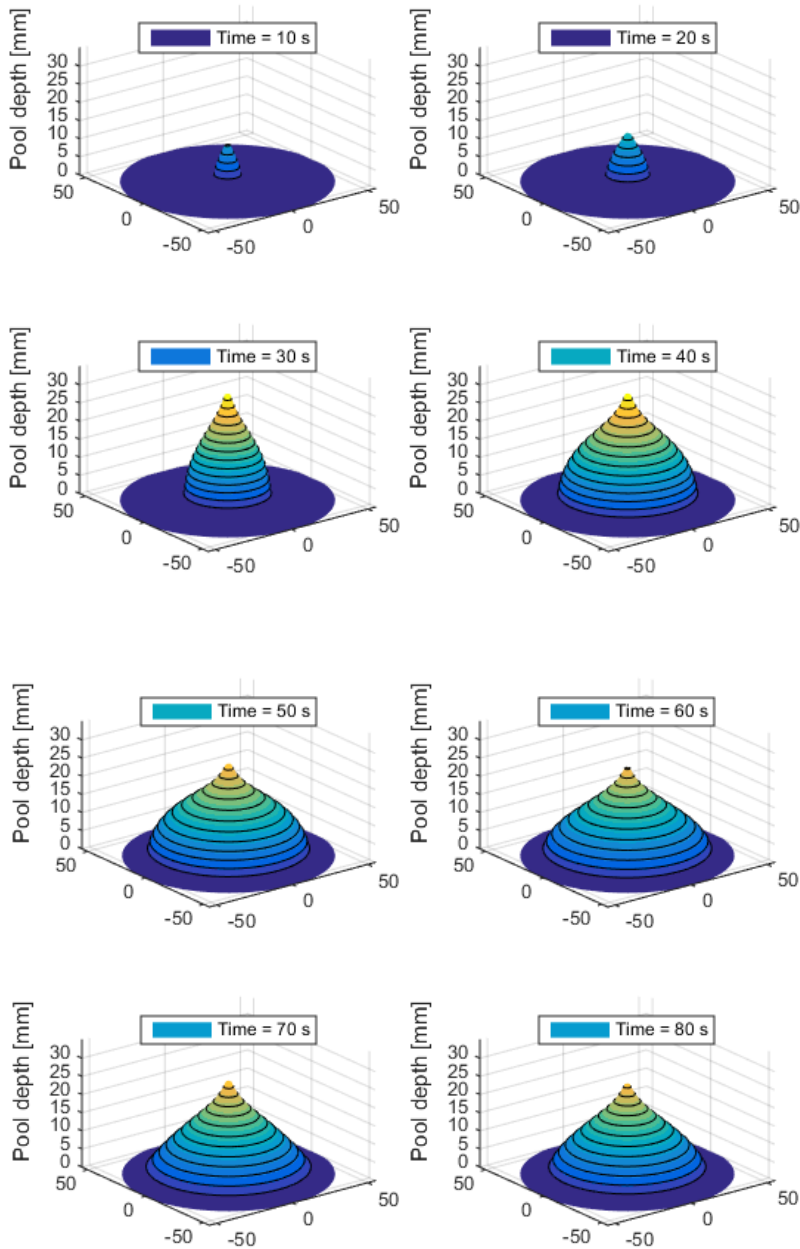


Figure 5.3: Cross-sectional pool depth development from 10 s to 80 s. Each contour line corresponds to a 2 mm difference. x - and y -axes in m, z -axis in mm.

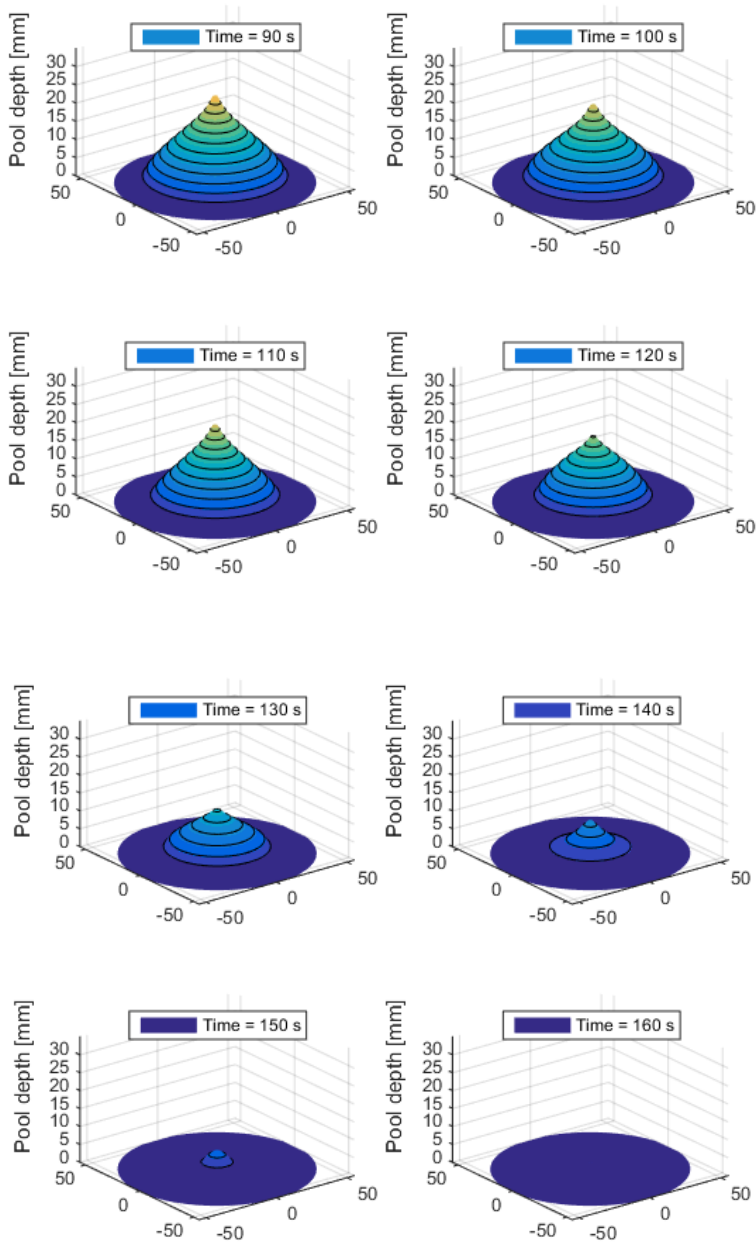


Figure 5.4: Cross-sectional pool depth development from 90 s to 160 s. Each contour line corresponds to a 2 mm difference in depth. x - and y -axes in m, z -axis in mm.

the earlier time steps. The «bulge» spreading outwards seen at time steps from 20 s through 60 s is likely a consequence of the rapid increase in LNG release at from approximately 20 s into the simulation time, spreading at a near-constant velocity.

While these figures are not directly comparable to any information provided of the Phoenix experiment [3], it is a nice supplement to Figs. 5.1 and 5.2, describing the pool area and mean pool depth, respectively.

5.4 No Ignition, Constant Fuel Regression Rate

Blanchat et al. [3] report an average burn rate for the smaller, 21 m LNG pool fire experiment of $0.147 \text{ kg/m}^2\text{s}$, by using a liquid methane density of 420 kg/m^3 . A similar quantity could not be computed for the larger, 83 m LNG pool fire experiment due to the reservoir emptying before the fire could reach a steady state. However, it is noted that dividing the average measured release rate of 802 kg/s by this regression rate, an equivalent pool diameter of 83.3 m is obtained, very similar to what was measured, so a mean fuel regression rate of $0.147 \text{ kg/m}^2\text{s}$ is suggested as a reasonable assumption for the larger LNG experiment as well.

Although not entirely physical, some simulations were performed in KFX with no ignition, but with a constant fuel regression rate. This was done in order to inspect how different burn rates caused by other effects (wind, water temperature, heat transfer to and from other sources) could affect an LNG spill, and to see to what effect this has on the shape of the LNG pool area curve. The KFX option *Forced ev.* was used to set forced vaporization rates of $0.147 \text{ kg/m}^2\text{s}$, $0.120 \text{ kg/m}^2\text{s}$ and $0.100 \text{ kg/m}^2\text{s}$, based evaporation data for cryogenic liquids on water [37, p. 146]. Additionally, one simulation with a 58% LNG mass flow and a vaporization rate of $0.085 \text{ kg/m}^2\text{s}$ (58% of $0.147 \text{ kg/m}^2\text{s}$) was performed. This was in order to account for the fact that, when assuming an LNG density of 420 kg/m^3 and water density of 1000 kg/m^3 , 42% of the LNG pool will be submerged below the water line, leaving 58% of the LNG above the water. Further, by assuming adiabatic conditions between the water and LNG and that only the LNG not submerged will spread, the «steady-state» vaporization rate and LNG spill are multiplied by 0.58. Though these last two assumptions are not entirely physical, this will be the basis of a simple model developed later, in Sec. 7.1.

The results are presented in Fig. 5.5, including the pool areas for sim17 and the Phoenix experiment for comparison. The pool area for the simulation with the constant quasi-steady vaporization rate follows that of the full simulation quite well, indicating that a steady burn rate of $0.147 \text{ kg/m}^2\text{s}$ is a reasonable approximation. It has a maximum area very similar to that of the Phoenix experiment. The pool area does not decline as rapidly after approximately 60 s, indicating that the vaporization rate in KFX is higher than $0.147 \text{ kg/m}^2\text{s}$ after approximately 60 s. The simulations with vaporization rates of $0.120 \text{ kg/m}^2\text{s}$ and $0.100 \text{ kg/m}^2\text{s}$ follows a very similar shape, however maximum areas were too high for both, with an equivalent diameter nearly 100 m for the simulation with a vaporization rate of $0.100 \text{ kg/m}^2\text{s}$. A general trend for all three is that the maximum area

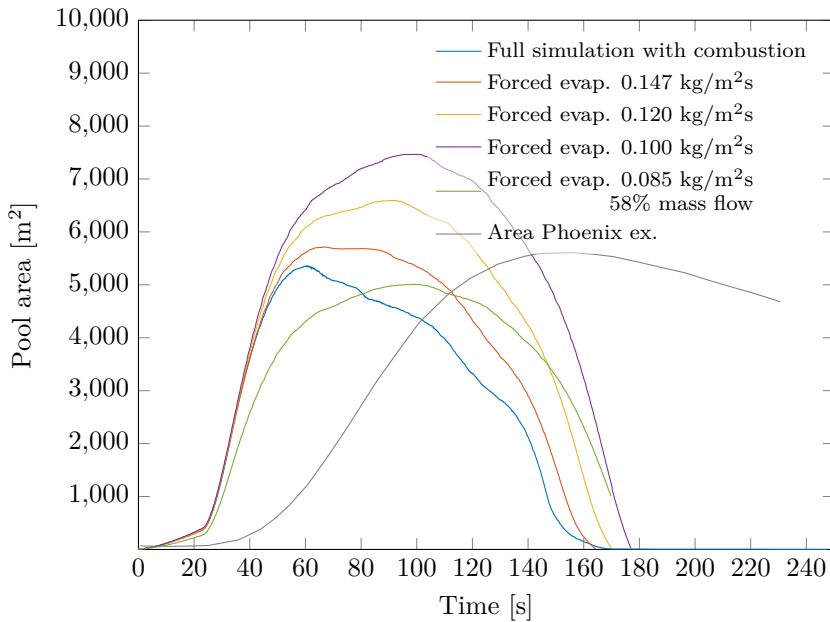


Figure 5.5: LNG pool areas for the simulations with no combustion and forced mass regression rates, compared to the «benchmark» simulation sim17 and the area trend of the Phoenix experiment.

appears later in the simulation time than the full simulations. This is likely due to several effects, radiative and convective heat transfer being the most prominent. As the fire grows, so will the radiative heat transfer from the fire down to the pool. Additionally, fire at these scales causes significant convective effects due to the buoyancy of the combustion products, sucking in surrounding air to replace the rapidly rising, less dense combustion products, increasing the convective heat transfer to the pool. These effects would not be present without combustion, and this is a possible reason for the difference in shape seen in the simulations with and without combustion. Common for all of these four simulations is that the LNG pool spreads at a much higher rate than the Phoenix experiment, and spreads almost three times as fast during the rapid spreading phase, i.e. the time period before the pool area starts to decrease, than the Phoenix experiment.

Finally, the simulation with mass flow and quasi-steady vaporization rate multiplied with a factor of 0.58 to account for the resistance of spreading through water, at least to see a general trend, achieved approximately the same peak area as the full simulation, however appearing almost 40 s later. While the simulation had a less steep initial spreading rate than the other simulations, it still had a maximum spreading rate almost twice as high as the Phoenix experiment.

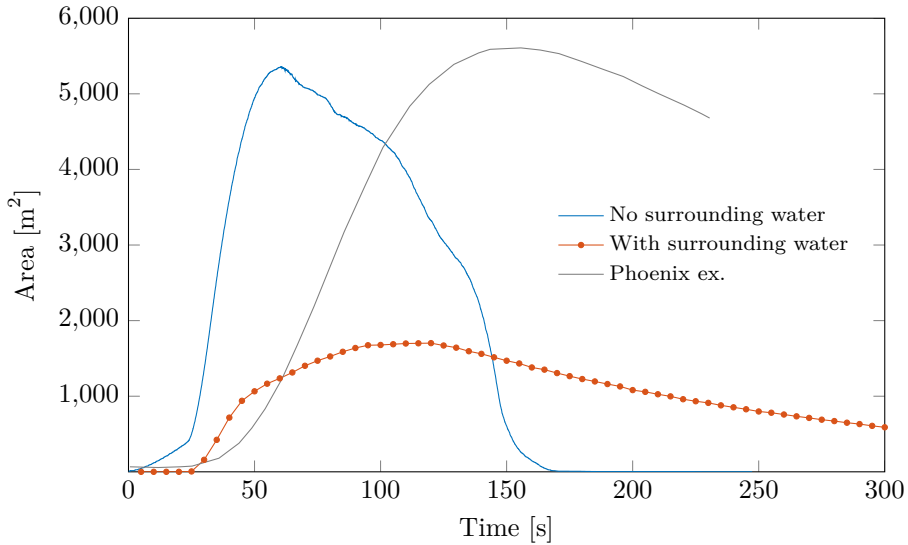


Figure 5.6: LNG spreading area in water, compared to the Phoenix experiment and the «benchmark» simulation sim17 with no surrounding water.

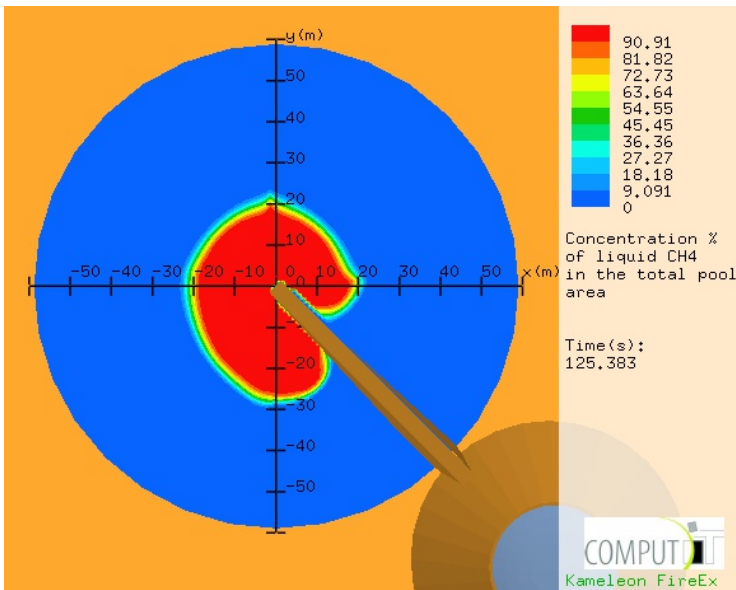
5.5 Effect of Surrounding Water Pool

The pool spreading model implemented in KFX is not optimized for multicomponent pools as noted in Sec. 4.2. Therefore, when the Phoenix experiment was modeled as a liquid release, it was modeled as an LNG release on flat ground, with various heat transfer coefficients to account for the heat transfer from the water to the LNG. However, this led to the LNG pool propagating too fast, as the physical effects of the LNG having to displace the surrounding water to spread were not included. Still, to test the spreading of LNG in a pool of water, a simulation was performed where the pool enclosure was filled with water ahead of the LNG leak time. Results for the area of LNG in the water pool over time is seen in Fig. 5.6.

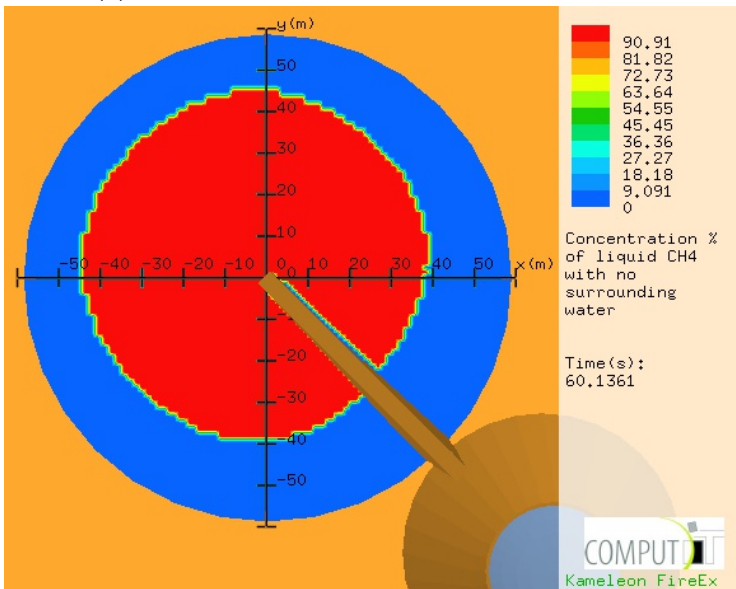
This data was sampled every five seconds², with dots indicating the data points. The LNG pool spread at a much lower rate, and reaching a maximum area far less than the single-component LNG pools. The total simulation time was 600 s, and at this point, approximately 1300 kg of LNG was still left in the pool, pointing to a LNG regression rate far less than both the previous simulations and the Phoenix experiment. The maximum pool area of approximately 1700 m² has an equivalent diameter of 47 m, almost half of the maximum diameter of Phoenix experiment and the other simulation cases.

The maximum pool area of this simulation with surrounding water is seen in Fig. 5.7a and compared to the maximum pool spreading area of the «benchmark» simulation sim17 in Fig. 5.7b.

²Contrary to the previous simulations, which were sampled at each time step.



(a) Maximum pool spread with surrounding water.



(b) Maximum pool spread without surrounding water.

Figure 5.7

By looking at the mass conservation for the liquid species, it is clear that this simulation case was somewhat unphysical. The mass conservation should naturally be 100%, meaning that no mass is created and no mass is destroyed. A value above 100% indicates that mass is created, and destroyed for value below 100%. When investigating the mass conservation over time, it is clear that it is numerically stable for the first 80 s, oscillating somewhat between 99.8% and 100.2%, within reasonable tolerance. However, after 80 s, the mass conservation percentage grows rapidly, converging towards 109% at the end of the simulation time. This may explain why there was a relatively low regression rate for the LNG pool area for the higher time steps, as mass was being created at a rate just below the vaporization rate.

Clearly, simulating the Phoenix case like this gave worse results than simulated as an LNG release on flat ground. An improved multicomponent pool spreading model for LNG and water would be of considerable interest, as LNG safety is largely related to harbor and open-water locations, where the LNG would be likely to leak from a ship or tank onto water. As demonstrated, neither of the two ways of simulating a large scale LNG release in KFX, on ground or on water, proved to accurately demonstrate the pool spreading effects seen in the Phoenix experiment.

6 Simulations - Flame Morphology

After the radiative heat fluxes and the pool spreading, the third major aspect of the investigations in the Phoenix experiments was the flame morphology, i.e. the width, height and area of the flame. As the grid resolution in the previous simulations in Chs. 4 and 5 was found sufficient for computing and measuring heat fluxes and pool spreading, some analysis was made that deemed the grid resolution, particularly in the vertical direction, not completely satisfying for investigation into the flame morphology. See *Animation 0* of sim23 in App. B.2, where it is evident that the grid was too coarse at the highest altitudes.

Thus, three new simulations were performed with refined grids. All were liquid releases, with the same transient release previously used. Two simulations, sim28 and sim29, had equal, very fine grids of $273 \times 271 \times 178 = 13.2 \times 10^6$ grid nodes, and one simulation, sim31, with $182 \times 182 \times 149 = 4.93 \times 10^6$ grid nodes, compared to the previous simulations with $183 \times 183 \times 90 = 3.01 \times 10^6$ grid nodes for the previous simulations. Simulations sim28 and sim29 had a very refined grid in the x - and y -directions directly above the pool enclosure, and all three simulations had refined grids in the z -direction, especially at higher altitudes. sim28 had the standard KFX option *all cells to ignition*¹, while sim29 had the option *ignition cells*², to investigate whether the ignition method influenced the simulations, and if so, to what effect. In sim29, one ignition cell was placed four grid nodes above the lower boundary, directly above the LNG release cells.

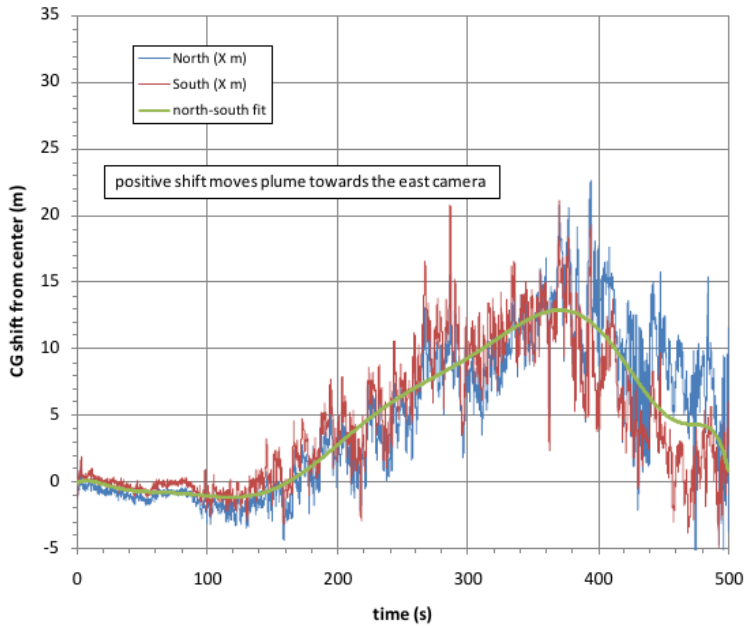
6.1 Flame Centroid and Maximum Height

Figs. 6.1 and 6.2 display the flame centroid shift³ on the x -axis (east-west), y -axis (north-south), z -axis (vertical) and the maximum flame height determined by calibrated video analysis from each of the four spokes in the Phoenix experiment.

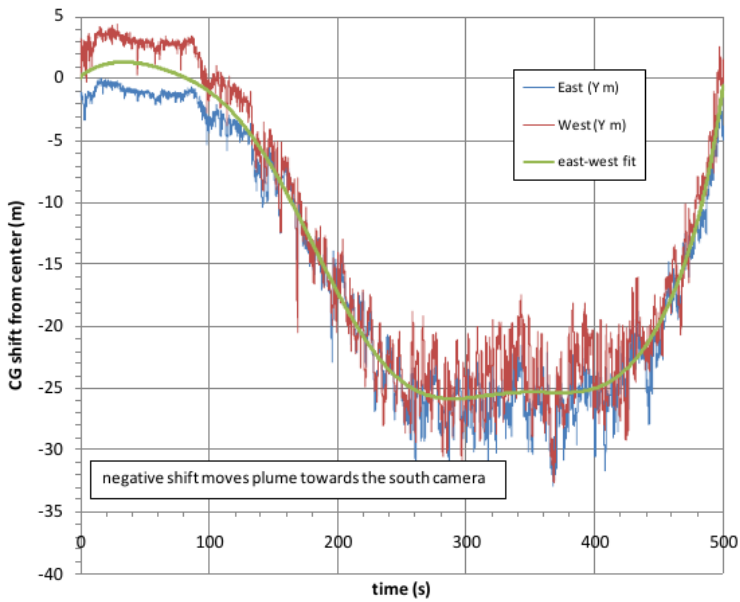
¹*Ignition in all free cells. The ignition is turned off if the maximum temperature in the field is raised to half the adiabatic flame temperature [35].*

²*Ignition in ignition cells. If the cells are located just above a pool, a heat flux of 6 kW/m^2 is imposed in the pool cells. The ignition is turned off if the maximum temperature in the field is raised to half the adiabatic flame temperature [35].*

³Somewhat incorrectly described as center of gravity (CG), by Blanchat et al. [3]. A center of gravity is a mass weighted spatial center, whereas a centroid is purely volumetric. For a body with uniform density, they are equal.

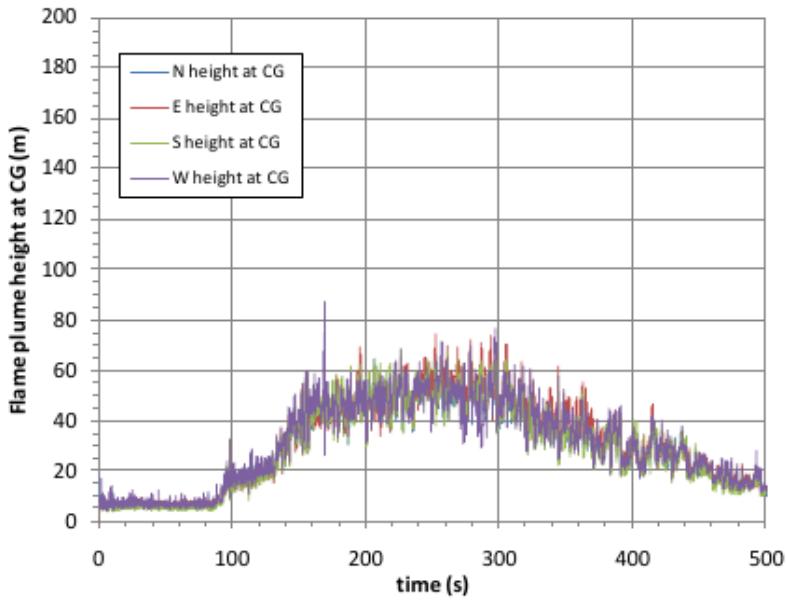
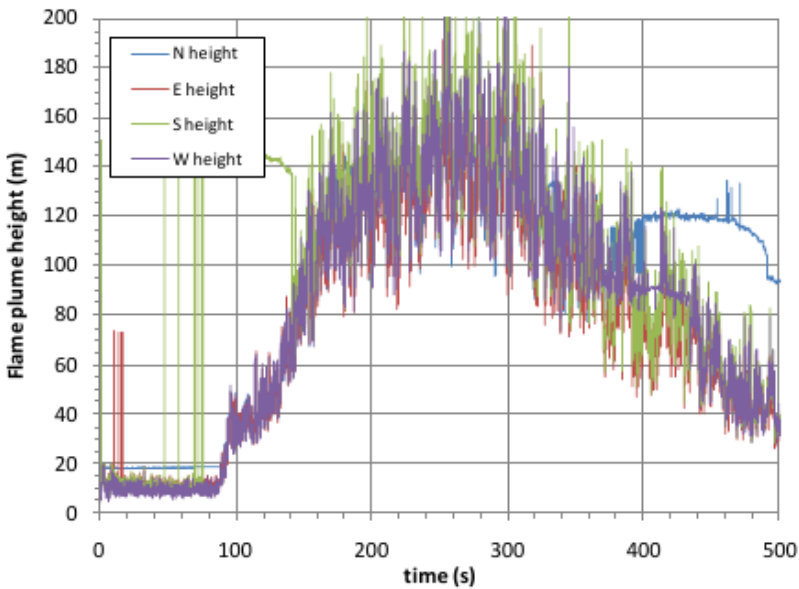


(a) x -axis centroid shift in the Phoenix experiment.



(b) y -axis centroid shift in the Phoenix experiment.

Figure 6.1: Centroid shift on the x - and y -axis in the Phoenix experiment. From [3].

(a) z -axis centroid shift in the Phoenix experiment.

(b) Flame peak height in the Phoenix experiment. Some clouds erroneously showed as fire by the image processing during the later times of the test. This can be seen on the far right, captured by the camera on the north spoke.

Figure 6.2: Centroid shift on the z -direction and maximum flame height. From [3].

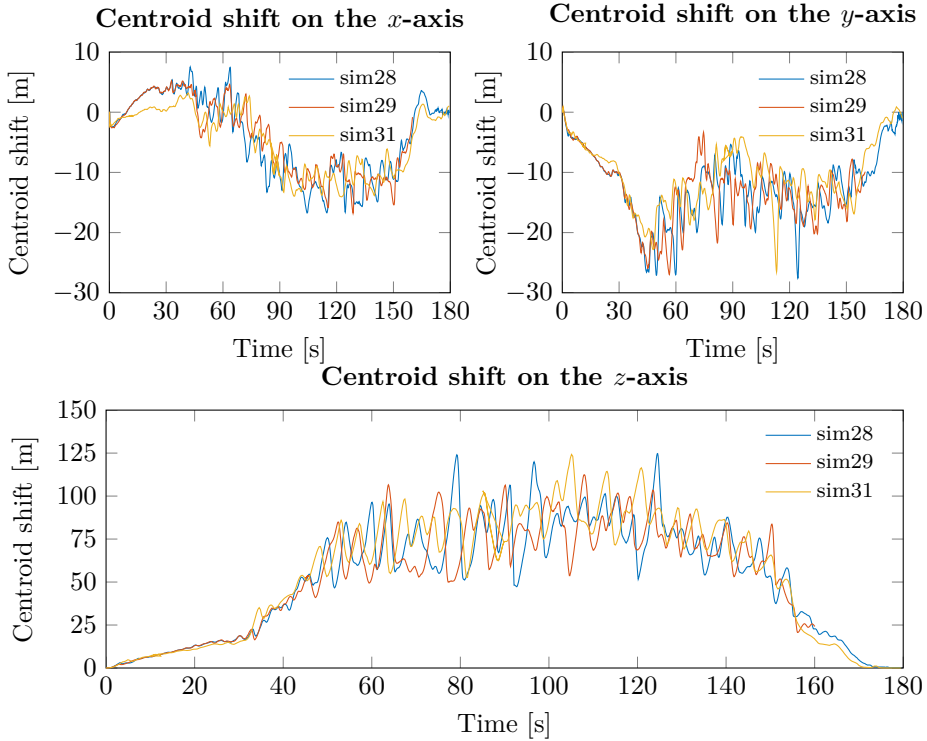


Figure 6.3: Centroid shift in the KFX simulations sim28, sim29 and sim31.

The flame centroid was dragged to the south-southeast direction, as the wind was predominantly from the north and as the flame anchored to the discharge pipes, lying at a 45° angle between the south and east spokes. Again, remember that $t = 100$ s in the Phoenix experiment corresponds to $t = 0$ s in the simulations.

During the simulations, KFX prints out the flame centroid for each time step. This data was then extracted in the post-processing for the three simulations, and plotted against time on the x -, y - and z -axes in Fig. 6.3. The three simulations all had very similar trends, despite individual fluctuations. The fluctuations in all three simulations were higher than the fluctuations seen in the Phoenix experiment, especially in the vertical directions.

The centroid on the y -axis shifted in the negative direction right away, towards the south spoke, consistent with the direction of the wind. A maximum shift of about 25 m was seen at 50 s for all three simulations. The centroid then fluctuated between about 10 m and 20 m for the rest of the simulation time, with a sudden shift to almost 30 m in both sim28 and sim29 around 120 s. On average, this is consistent with the centroid shift in the Phoenix experiment y -axis shift, Fig. 6.1b.

After a minor initial shift in the positive x -direction, all three simulations shifted in the negative x -direction, that is, to the west. This is somewhat surprising, as the

flame was expected to be dragged along the direction of the incoming wind – to the south-southeast. However, the x -component of the wind was small compared to the y -component, and the centroid shift to the east seen in the Phoenix experiment, Fig. 6.1a, is believed to mostly be a consequence of the flame anchoring, not the wind. For the duration of the experiment, the wind direction was relatively steady at about 330° clockwise from the magnetic north, with some fluctuations between 310° and 340° . As seen in Fig. 6.1a, the centroid shifted more and more towards the east for the duration of the test, at a time where the both the wind speed and direction was relatively steady.

The z -axis centroid had an almost linear increase in altitude as the LNG flow into the pool increased until about 30 s into the run time of the simulations. As the flow rate greatly increased at about 30 s, so did the vertical centroid shift, reaching a time-averaged peak height at approximately 90 m. However the centroid fluctuated greatly, varying between 50 m and up to 125 m between 60 s and 140 s. These fluctuations of ± 35 m from the average of 90 m (determined by visual inspection), is far greater than the fluctuations of ± 10 m from an average of 50 m in the Phoenix experiment during the nearly steady-state interval of 250 s – 300 s, seen in Fig. 6.2a. Additionally, the average centroid height is almost 40 m greater in the simulations, than the experiment. This may also be a consequence of the flame anchoring (or, the lack of), which had the effect holding the plume relatively steady for a large part of the experiment.

The maximum flame height is not something KFX outputs by itself, so in order to inspect this, two animations were made from sim31. These can be seen in the links in App. B.2, in *Animation 1* and *Animation 2* of sim31. *Animation 1* has an opacity value of 0.3 and *Animation 2* has an opacity value of 0.7, and a nearly opposite horizontal view angle of *Animation 1*. Together, they produce a good view of the transient behavior of the fire. As indicated by the vertical centroid shift, the flame far higher maximum heights than the Phoenix experiment. During the interval 50 s – 150 s, plume heights below 150 m are rarely seen, with a total maximum height bordering 300 m at a few instances. This is in contrast to the plume height in the Phoenix experiment, Fig. 6.2b, where maximum values of about 200 m were recorded.

The flame tilt was qualitatively investigated, and appeared to be similar to that of the Phoenix experiment: approximately zero. Some tilting was observed, but both the angle and duration of this tilt was fluctuating, and varied from simulation to simulation.

6.2 Flame Anchoring

As noted in Ch. 4, the effect of flame anchoring prominent in the Phoenix experiment was not seen in any of the simulations. As noted, the grids in the three simulations sim28, sim29 and sim31 were refined in z -direction, especially at the higher altitudes. However, the vertical grid was also refined in the lower regions of the domain, to investigate if the lack of flame anchoring in the simulations was

due to the grid being too coarse near the discharge pipes. *Animation 3* in App. B.2 shows an animation of sim31 from a bird's-eye view with a cut in the plane $z = 6$ m, displaying the transient behaviour of the flame near the ground. No flame anchoring is evident, and both the fire and evaporated methane, showing as white, seem largely unaffected by the discharge pipes. Further refinement of the grid at this level was deemed unnecessary, as the animation shows fire structures with a length scale significantly smaller in size than the discharge pipes.

7 Non-KFX Analysis of Pool Spreading

As seen in Ch. 5, the LNG pool in the KFX simulations spread at a much higher rate than that in the Phoenix experiment. It was also noted in Sec. 5.4 that a new, simple model for spreading of a less dense liquid through a denser one was developed based on the density differences of liquid methane and water. This model is thought to take into account the fact that the LNG has to displace the surrounding water to spread, significantly reducing the spreading rate, and hence the radial velocity of the LNG.

7.1 New Model for Oil Pool Spreading Through Water

Consider a two-component pool, LNG and water in this case, as in Fig. 7.1. Assuming a circular pool, we can denote the radial velocity, or front velocity, as \bar{v} . By expressing the density of the less dense liquid (i.e. LNG) as ρ_l , the denser liquid (i.e. water) as ρ_w , and by assuming that the less dense liquid has a uniform thickness, δ , on top of the denser liquid, the front velocity is estimated by Magnussen [21] to be

$$\bar{v} = \frac{2}{3} \left(2g\delta \frac{\rho_w - \rho_l}{\rho_w} \right)^{1/2} \left(\frac{\rho_w - \rho_l}{\rho_w} \right), \quad (7.1)$$

where g is the gravitational constant. The fraction of the densities, $(\rho_w - \rho_l)/\rho_w$, is equal to the ratio of the height of the LNG above the waterline, H_1 , to the total thickness, δ , that is, H_1/δ . Eq. (7.1), is then written as

$$\bar{v} = \frac{2}{3} (2gH_1)^{1/2} \left(\frac{\rho_w - \rho_l}{\rho_w} \right). \quad (7.2)$$

By assuming that the LNG above the waterline spreads similarly as on flat ground, its mean velocity, denoted by v_1 , can be given as a function of the square root of the potential energy of the liquid above the waterline, multiplied by a factor for $\frac{2}{3}$ to account for its resultant hydrostatic pressure force in the radial direction being a distance of two thirds of its total height from the free surface:

$$v_1 = \frac{2}{3} \sqrt{2gH_1}. \quad (7.3)$$

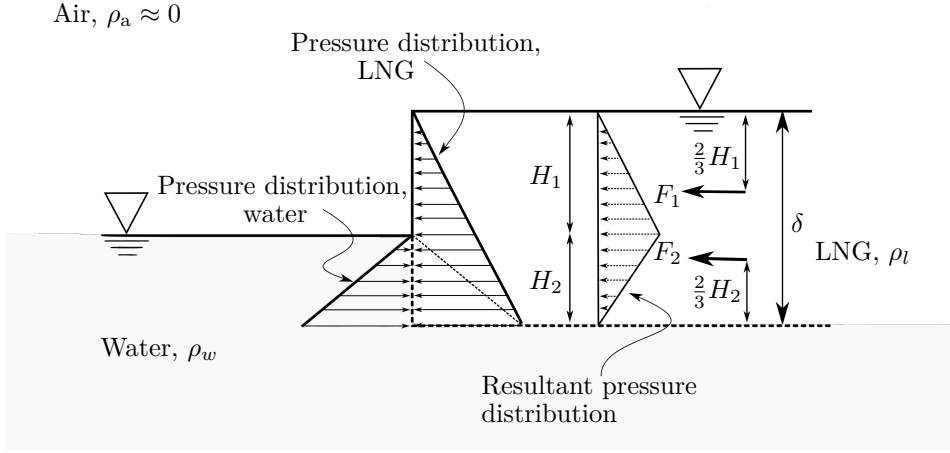


Figure 7.1: Spreading of LNG on water. F_1 and F_2 are resultant forces from the pressure distribution.

The total momentum per unit volume of the displaced water equals the mean velocity of the LNG, \bar{v} , multiplied by the density of water, ρ_w . By applying a momentum balance (per unit volume) and neglecting the density of the air, we get

$$v_1(\rho_w - \rho_l) = \bar{v}\rho_w, \quad (7.4)$$

and solving for \bar{v} gives

$$\bar{v} = \frac{\rho_w - \rho_l}{\rho_w} v_1. \quad (7.5)$$

By combining Eqs. (7.5) and (7.3), Eq. (7.1) is produced.

Returning to the original formulation, Eq. (7.1) can be rearranged to

$$\bar{v} = \underbrace{\left(\frac{2}{3} (2g)^{1/2} \left(\frac{\rho_w - \rho_l}{\rho_w} \right)^{3/2} \right)}_C \delta^{1/2}, \quad (7.6)$$

or

$$\bar{v} = C \cdot \delta^{1/2}. \quad (7.7)$$

With $\rho_l \approx 420 \text{ kg/m}^3$ being the density of liquid methane, $\rho_w \approx 1000 \text{ kg/m}^3$ being the density of water and g being the gravitational constant, the coefficient C is approximately equal to $1.30 \text{ m}^{1/2}/\text{s}$.

Two approaches to test this relation were performed, called *Method 1* and *Method 2*. In both methods, the pool was assumed to be circular in shape with a constant vaporization rate.

7.1.1 Method 1

Method 1 was based on solving for the pool radius r , by the relation

$$\bar{v} = \frac{dr}{dt} = C\delta^{1/2}. \quad (7.8)$$

The pool thickness δ , can be expressed as

$$\delta = \frac{m(t)}{\rho_l A(t)}, \quad (7.9)$$

where $m(t)$ is the mass in the pool at time t , $A(t)$ is the pool area at time t and ρ_l is the LNG density, assumed constant, 420 kg/m³. The mass in the LNG pool at a given time, $m(t)$, can be expressed

$$m(t) = \int_0^t \dot{m}_{\text{in}} dt - \int_0^t \dot{m}_{\text{out}} dt = \int_0^t \dot{m}_{\text{in}} dt - \int_0^t \dot{m}_{\text{vap}}'' A dt. \quad (7.10)$$

\dot{m}_{in} is the mass flow of LNG into the pool and is known through the approximation in Fig. 4.2. \dot{m}_{vap}'' is the vaporization rate of the LNG, and by approximating this as constant, 0.147 kg/m²s, it can be taken outside the integral in Eq. (7.10) to produce

$$m(t) = \int_0^t \dot{m}_{\text{in}} dt - \dot{m}_{\text{vap}}'' \int_0^t A dt. \quad (7.11)$$

The radius r can from the equation for the area of a circle, $A = \pi r^2$, be written

$$r(t) = \frac{1}{\sqrt{\pi}} A^{1/2}. \quad (7.12)$$

Inserting Eqs. (7.11) and (7.12) into Eq. (7.8), we get

$$\frac{1}{\sqrt{\pi}} \frac{dA^{1/2}}{dt} = C \left(\frac{\int_0^t \dot{m}_{\text{in}} dt - \dot{m}_{\text{vap}}'' \int_0^t A dt}{\rho_l A} \right)^{1/2}. \quad (7.13)$$

Rearranging gives

$$A \frac{dA^{1/2}}{dt} = C \left(\frac{\pi}{\rho_l} \right)^{1/2} \left[\int_0^t \dot{m}_{\text{in}} dt - \dot{m}_{\text{vap}}'' \int_0^t A dt \right]^{1/2}, \quad (7.14)$$

where $A(t)$ and $\dot{m}_{\text{in}}''(t)$ are written as A and \dot{m}_{in}'' , respectively, for simplicity. $\int_0^t \dot{m}_{\text{in}} dt$ is the integrated curve in Fig. 4.2 at time t , and can be written as $m_{\text{in}}(t)$. Eq. (7.14) is then simplified to

$$A \frac{dA^{1/2}}{dt} = C_1 \left[m_{\text{in}} - \dot{m}_{\text{vap}}'' \int_0^t A dt \right]^{1/2}, \quad (7.15)$$

where $C_1 = C(\pi/\rho_l)^{1/2}$. By writing $A^{1/2}$ as $\sqrt{\pi}r$ and A as πr^2 , we get

$$\sqrt{\pi}r\sqrt{\pi}\frac{dr}{dt} = \pi r r' = C_1 \left[m_{\text{in}} - \pi \dot{m}_{\text{vap}}'' \int_0^t r^2 dt \right]^{1/2}, \quad (7.16)$$

and solving for $r' = \frac{dr}{dt}$ gives

$$r'(t) = \frac{C_1 \left[m_{\text{in}} - \pi \dot{m}_{\text{vap}}'' \int_0^t r^2 dt \right]^{1/2}}{\pi r}. \quad (7.17)$$

Introducing the substitution $\int_0^t r(t)^2 = f(t) \Rightarrow f'(t) = r(t)^2$, we get the differential vector \mathbf{u} containing the set of first order ordinary differential equations (ODEs):

$$\frac{d\mathbf{u}}{dt} = \begin{bmatrix} r'(t) \\ f'(t) \end{bmatrix} \quad (7.18)$$

where $r'(t)$ and $f'(t)$ are

$$r'(t) = \frac{C_1 \left[m_{\text{in}}(t) - \pi \dot{m}_{\text{vap}}'' f(t) \right]^{1/2}}{\pi r(t)} \quad (7.19)$$

and

$$f'(t) = r(t)^2, \quad (7.20)$$

respectively. This set of ODEs was solved numerically in MATLAB by the ODE solver `ode45`, which is the recommended MATLAB solver for nonstiff ODEs [23]. The script is seen in App. C.1.1. The initial values, $r_0 = 9$ m and $f_0 = 81$ m², were based on an educated guess and modified to give the best results. After solving this, the area was evaluated by $A(t) = \pi r(t)^2$, the pool thickness was evaluated by inserting Eq. (7.11) into Eq. (7.9) to produce

$$\delta = \frac{1}{\rho_l A} \left(m_{\text{in}} - \int_0^t \dot{m}_{\text{vap}}'' A dt \right). \quad (7.21)$$

Finally, the front velocity \bar{v} was computed by Eq. (7.7). The results are presented in Fig. 7.2.

7.1.2 Method 2

While *Method 1* was based on solving for the pool radius $r(t)$ and a function of the pool radius $f(t)$, *Method 2* is based on solving the set of ODEs for the pool radius and thickness

$$\frac{d\mathbf{u}}{dt} = \begin{bmatrix} r'(t) \\ \delta'(t) \end{bmatrix}, \quad (7.22)$$

where

$$r'(t) = C\delta^{1/2}, \quad (7.23)$$

which follows from Eq. (7.7). The derivation of $\delta'(t)$ starts with the relation for the mass in the pool at time t :

$$m(t) = \rho_l A(t)\delta(t) = m_{\text{in}}(t) - m_{\text{out}}(t). \quad (7.24)$$

Rearranging gives

$$\delta = \frac{1}{\rho_l} \left(\frac{m_{\text{in}}}{A} - \frac{m_{\text{out}}}{A} \right) = \frac{1}{\rho_l} \left(\frac{m_{\text{in}}}{\pi r^2} - m''_{\text{vap}} \right). \quad (7.25)$$

Taking the time derivative of Eq. (7.25) gives

$$\frac{d\delta}{dt} = \delta'(t) = \frac{1}{\rho_l} \left(\frac{\dot{m}_{\text{in}}\pi r^2 - 2\pi r m_{\text{in}} \frac{dr}{dt}}{\pi^2 r^4} - \dot{m}''_{\text{vap}} \right), \quad (7.26)$$

where the quotient rule has been used on $m_{\text{in}}(t)/\pi r(t)^2$. Simplifying, we get

$$\delta'(t) = \frac{1}{\rho_l} \left(\frac{\dot{m}_{\text{in}}r - 2m_{\text{in}}r'}{\pi r^3} - \dot{m}''_{\text{vap}} \right), \quad (7.27)$$

which then goes into Eq. (7.22). \dot{m}_{in} , m_{in} and \dot{m}''_{vap} are as previously defined. As with *Method 1*, this was solved numerically in MATLAB by the solver `ode45`. The initial conditions were set to $r_0 = 9$ m and $\delta_0 = 1$ mm. The script can be found in App. C.1.2. After solving for the radius and pool thickness, the area was found by $A = \pi r^2$ and the front velocity was found from the LNG thickness by Eq. (7.7). Results are seen in Fig. 7.3.

7.1.3 Results

The numerical results for all of the calculations were after some time complex, with the imaginary part exceeding the tolerance criterion of approximately $2 \cdot 10^{-5}$ at the green, vertical line in Figs. 7.2 and 7.3. This is roughly where the pool thickness δ is zero, making sense from both a physical and mathematical point of view. The physical reason is obvious; a physical quantity such as the pool thickness, cannot be of negative value. The mathematical reason follows from Eq. (7.7); as δ is to the power of $\frac{1}{2}$, a negative value implies a complex solution. Thus, only the results to the left of the green lines can be considered relevant for this discussion.

In both Figs. 7.2 and 7.3, the area trend from the Phoenix experiment is plotted alongside the area curves. The results were considered fairly good, with *Method 1* being somewhat more numerical stable in suppressing the imaginary parts for a longer time than *Method 2*. The reason for this is not known, but likely is based the higher order of complexity in the ODEs in *Method 2*. However, the solutions followed each other closely, and all four quantities, radius, area, pool thickness and

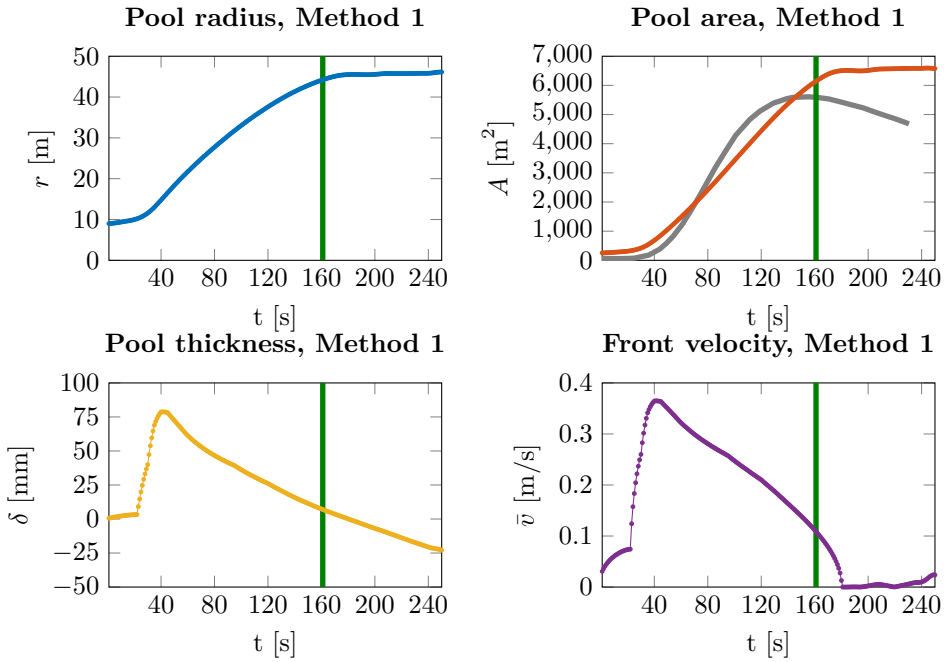


Figure 7.2: Solution of Eq. (7.7) by Method 1

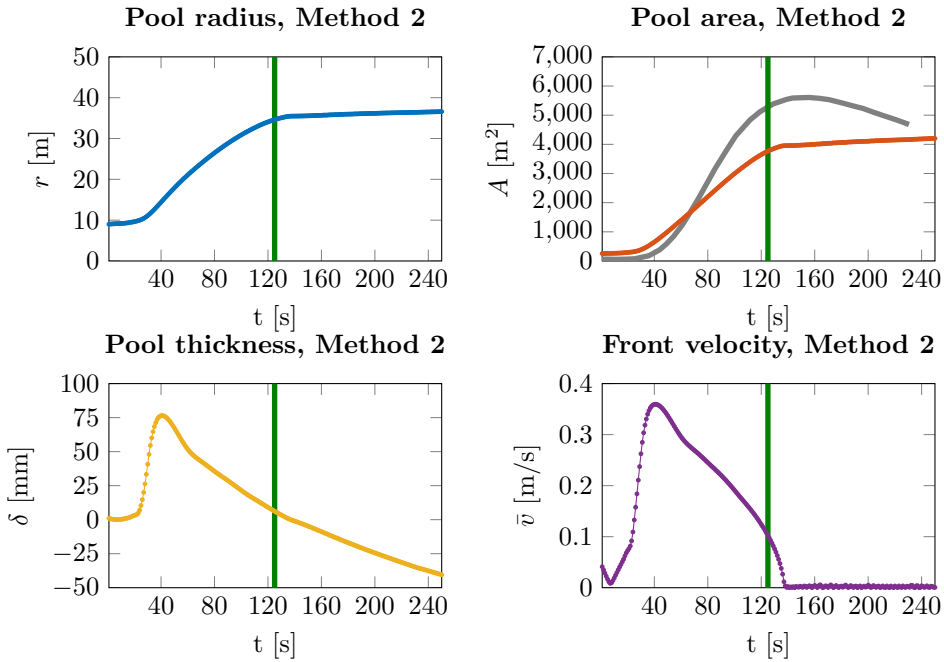


Figure 7.3: Solution of Eq. (7.7) by Method 2

front velocity, were similar in shape and magnitude.

The computed area in *Method 1* followed the area from the Phoenix experiment quite closely until the experimental area started to retract, and the computed area went into the complex domain as the pool thickness approached zero.

The pool thickness in both *Method 1* and *Method 2* peaked at a much higher level than the mean pool depth in KFX, seen in Fig. 5.2, achieving a maximum of about 75 mm, more than five times the levels reached the KFX simulations. However, the maximum pool thickness was reached at 40 s, the same time as the mean depths in the KFX simulations reached their maximum value.

Given the limitations of these results due to the various assumptions (constant vaporization rate, approximated LNG mass flow and uniform pool thickness), these results are thought to be very promising, and should be of interest for future investigation.

7.2 Calculations Based on the Phoenix Experiment Data

It is evident when compared to the trend from the Phoenix experiment, that the pool areas in Figs. 7.2 and 7.3 spread at a lower rate than the Phoenix experiment after about 50 s. Hence, the front velocity would also have been lower. To investigate this, some calculations of pool spreading were done based on the pool area curve given by Blanchat et al. [3]. Unfortunately, no data for the pool area is given beyond 230 s, even though the fire had a total duration of approximately 420 s.

Two approaches were made for these calculations. The first approach involved approximating the area curve from the Phoenix experiment as a polynomial function, and then performing various operations on this in order to get the front velocity, and then using the relation in Eq. (7.7) to get the pool thickness. The other involved solving a single ODE for the mean LNG pool thickness, and then applying Eq. (7.7) to get the front velocity.

7.2.1 The Polynomial Approach

The MATLAB function `polyfit` was used to approximate the area with a polynomial function. A ninth degree polynomial was, after some trial and error, found to fit the data set nicely, except for the first couple of seconds.¹ After this polynomial was found, the radius was calculated by $r = \sqrt{A/\pi}$. The front velocity was then found by taking the derivative of this and inserting time values in the domain of 0 s to 230 s. Finally, the mean LNG pool thickness was found by applying Eq. (7.7). As the front velocity has negative values for $t \gtrsim 150$ s, the values for the mean LNG pool thickness are not to be seen as valid, as Eq. (7.7) does not allow negative front velocities. Results are seen in Fig. 7.4.

¹ $A(t) = -2.41 \cdot 10^{-15}t^9 + 2.62 \cdot 10^{-12}t^8 - 1.18 \cdot 10^{-9}t^7 + 2.82 \cdot 10^{-7}t^6 - 3.75 \cdot 10^{-5}t^5 + 2.66 \cdot 10^{-2}t^4 - 8.77 \cdot 10^{-2}t^3 + 1.37t^2 - 8.97t + 70.4$

7.2.2 The ODE Approach

The data sets for the area from the Phoenix experiment and the approximated LNG release rate were used as basis functions. The LNG density and vaporization rate were assumed constant as 420 kg/m^3 and $0.147 \text{ kg/m}^2\text{s}$, respectively. Starting with the equation for mass in the pool at a given time t , we have

$$m(t) = \rho_l A(t) \delta(t), \quad (7.28)$$

where the (t) 's will be omitted for simplicity. Taking the derivative of this, we get

$$\dot{m} = \dot{m}_{\text{in}} - \dot{m}''_{\text{vap}} A = \rho_l \left(\frac{dA}{dt} \delta + A \frac{d\delta}{dt} \right). \quad (7.29)$$

Rearranging, this becomes

$$\frac{dA}{dt} \delta + A \frac{d\delta}{dt} = \frac{1}{\rho_l} (\dot{m}_{\text{in}} - \dot{m}''_{\text{vap}} A), \quad (7.30)$$

and after dividing by A and introducing the functions $f(t)$ and $g(t)$ we get

$$\frac{d\delta}{dt} + \underbrace{\frac{1}{A} \frac{dA}{dt}}_{f(t)} \delta = \underbrace{\frac{1}{\rho_l} \left(\frac{\dot{m}_{\text{in}}}{A} - \dot{m}''_{\text{vap}} \right)}_{g(t)}. \quad (7.31)$$

Finally, we get the ODE for δ with the two known, time-dependent functions $f(t)$ and $g(t)$:

$$\delta'(t) = -f(t)\delta(t) + g(t). \quad (7.32)$$

This was also solved numerically in MATLAB by the solver `ode45`, with the initial condition $\delta_0 = 0 \text{ mm}$. A curve smoothing function was used on the area data set $A(t)$ before finding the numerical derivative $A'(t)$, to avoid step functions in the data set. Results are seen in Fig. 7.5.

7.2.3 Results

Figs. 7.4 and 7.5 shows the results for the mean LNG pool thickness and frontal velocity. The polynomial approach, Sec. 7.2.1 and Fig. 7.4, first computed the front velocity, then applied Eq. (7.7) to obtain the mean LNG pool thickness. The ODE approach, Sec. 7.2.2 and Fig. 7.5, went the other way, by first computing the mean LNG pool thickness and then applying Eq. (7.7) to obtain the front velocity. Obviously, the results for the ODE approach are not valid after about 180 s, when the mean LNG pool thickness have negative values. However, despite these differences, the results are comparable. The polynomial approach gave a maximum front velocity of just below 0.6 m/s at about 50 s, giving a maximum mean LNG pool thickness of approximately 180 mm. The ODE approach produced a higher mean LNG pool thickness at almost 220 mm, giving a maximum front velocity of

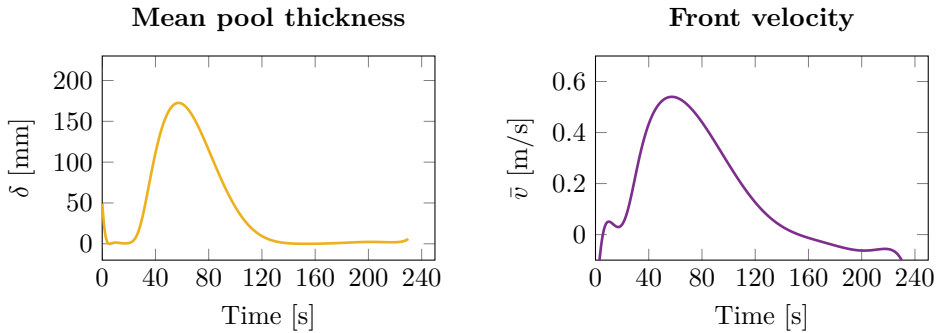


Figure 7.4: Polynomial computation of front velocity and mean LNG pool thickness based on Phoenix series data. Computation order: front velocity \rightarrow Eq. (7.7) \rightarrow mean LNG pool thickness.

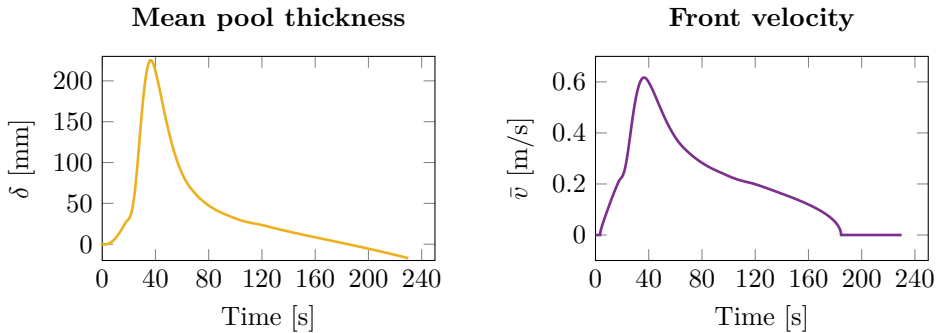


Figure 7.5: Differential computation of front velocity and mean LNG pool thickness based on Phoenix series data and approximated LNG mass flow. Computation order: mean LNG pool thickness \rightarrow Eq. (7.7) \rightarrow front velocity.

0.6 m/s. This peak occurred somewhat earlier, just before 40 s. This difference in maximum values is what separates these solution methods the most, as the shape of the curves are similar, however with the polynomial approach being somewhat more rounded in shape than the ODE approach.

Comparing to the computations in Sec. 7.1, the most distinctive result is the magnitude of the mean LNG pool thickness, even more so when comparing to the results by KFX in Sec. 5.2. These last results are of magnitude two to three times those seen in Sec. 7.1, and more than ten times the pool depth obtained in the KFX simulations. It is worth noting that in the results for the mean LNG pool thickness in the non-KFX computations, approximately 42% of the pool would be below the waterline², leaving only 58% of the computed LNG pool thickness as an actual «thickness» to be seen above the waterline.

²Assuming hydrostatic conditions.

7.3 Comparison to Other Models

Woodward and Pitblado [37] summarizes some of the existing models for oil spills on water, and note that the spreading rate in the radial direction is proportional to the potential energy of the leading edge. This radial velocity can be written in a number of ways, in terms of the volume of liquid, V , in the pool, mass m and density ρ_l of the oil. The spreading rate can be written as [37, p. 138]

$$\bar{v} = \frac{dr}{dt} = k_s (\delta g \Delta)^{\frac{1}{2}} = k_s \left(\frac{gV\Delta}{r^2} \right)^{\frac{1}{2}} = k_s \left(\frac{m_l g \Delta}{\rho_l A} \right)^{\frac{1}{2}} = k_s \left(\frac{m_l g \Delta}{\rho_l \pi} \right)^{\frac{1}{2}} \frac{1}{r}, \quad (7.33)$$

where k_s is a thermal conductivity coefficient to the water, suggested as 1.41 W/mK, and Δ is the ratio $(\rho_w - \rho_l)/\rho_w$, approximately equal to 0.58.³ The term $k_s (\delta g \Delta)^{\frac{1}{2}}$ in Eq. (7.33) bears similarity to Eq. (7.1). By using the suggested value for k_s , $\Delta = 0.58$ and $g = 9.81 \text{ m/s}^2$, we get

$$\bar{v} = 3.36 \cdot \delta^{1/2}, \quad (7.34)$$

a factor of 2.58 higher than Eq. (7.7). Eq. (7.34) was used in the computation methods in Secs. 7.1.1 and 7.1.2, and compared with the previous computations. The computations with Eq. (7.7) in Secs. 7.1.1 and 7.1.2 followed the area from the Phoenix experiment better and were somewhat more numerically stable than by using Eq. (7.34). Both this model and the one developed in Sec. 7.1 assumes that the water surface can be treated as a perfectly flat, with minimal disturbance by the spreading oil, e.g. waves and similar effects, and an essentially uniform oil pool thickness.

Woodward and Pitblado [37] establish that the relationships in Eq. (7.33) are stable for a pool thickness larger than some minimal stable value, depending on the surface on which the LNG is spilled. Two open water tests by Esso are cited, where minimum stable thicknesses of 4.4 mm and 6.7 mm were found. This is quite consistent with what was experienced with Eq. (7.7), where the imaginary part exceeded the tolerance value when the pool thickness was below 7.0 mm and 6.2 mm for *Method 1* and *Method 2*, respectively.

Three different regimes for cryogenic liquid spreading on water are stated. These are [37, p. 140]:

1. *Gravity-inertia regime* – equate gravity and inertial spreading
2. *Gravity-viscous regime* – equate gravity and viscous spreading
3. *Surface tension regime* – equate viscous drag and surface tension

Eqs. (7.7) and (7.34) both apply to the first regime. A generalized solution is provided for a continuous release rate $\dot{m}_{\text{in}}(t)$:

³For simplicity, the same notation as previously is retained. Woodward and Pitblado [37] use a slightly different notation.

Gravity-inertia regime, $0 < t < t_3$:

$$r(t) = 1.24(g\Delta)^{1/4}\dot{m}_{\text{in}}(t)^{1/4}t^{3/4}. \quad (7.35)$$

Gravity-viscous regime, $t > t_3$:

$$r(t) = 1.09 \left(\frac{g\Delta}{\nu_w^{1/2}\rho_l} \right)^{1/6} \dot{m}_{\text{in}}(t)^{1/3}t^{7/12}. \quad (7.36)$$

Transition time for the two regimes, t_3 :

$$t_3 = \left(\frac{1.09}{1.24} \right)^6 \left(\frac{\dot{m}_{\text{in}}(t)}{\mu_w \rho_l g \Delta} \right)^{1/2}. \quad (7.37)$$

These relations have not been tested numerically during the work on this thesis. However, in combination with Eq. (7.7), these relations could form a basis for improvement of the pool spreading model in KFX.

8 Discussion

A number of simulations have been performed to compare the KFX CFD software to various aspects of the Phoenix large scale LNG pool fire experiments. The larger of the two experiments, called LNG Test 2, had a maximum pool spreading diameter of approximately 83 m. The main aspects investigated were the radiative heat flux, the pool spreading area and the morphology (i.e. height, length and width) of the flame.

The radiative heat fluxes were measured on four principal spokes around the pool, with three measuring points on each spoke, 110 m, 160 m and 210 m from the pool center.

With the currently implemented standard soot model in KFX, the Eddy Dissipation Soot Model, the time-averaged radiative heat fluxes for all four spokes were dampened by a factor of two to four, compared to the Phoenix experiment. Modeled as a gaseous release of methane, the time-averaged heat fluxes were on average about 20% higher than when simulated as a liquid release, and letting the various submodels in KFX handle the vaporization rate. When simulated as a transient release, the boundary condition for the LNG release was approximated from LNG release in the Phoenix experiment. For these transient simulations, the heat fluxes for the time-averaged interval (where the heat fluxes remained relatively steady) were about 10% lower than when simulated as a constant release, based on an average release rate of 800 kg/s. Other than the pond containing the water pool, the only significant structures in the experiment were the discharge pipes leading the LNG from the storage reservoir and onto the water pool. When these were included in the CAD model, the time-averaged heat fluxes increased with approximately 10%. Due to limitations on the pool multicomponent spreading model in KFX, the water was modeled as a «ring» of water in an enclosure outside of the LNG area. This surrounding water pool gave a small increase of the heat fluxes, but negligible compared to the other variations to the simulations.

Due to the heat fluxes being too low, the soot model was investigated, and it was found that the amount of relatively cold soot in the vicinity of the flame was too high. This layer of cold soot acted as a radiation screen, reducing the thermal radiation from the flame to the surroundings. A term in the soot model controlling combustion of produced soot was then modified such that the combustion of soot increased. This proved to give a positive impact on the heat fluxes, and the average radiative heat fluxes from the Phoenix experiment and the KFX simulations were

very equal in magnitude.

Variations of the simulations performed with this modified soot model included constant/transient release, various heat transfer coefficients to the ground and surrounding water pool. All of these simulations were of liquid methane, as the heat fluxes in the liquid releases were found to be far less volatile. With no heat transfer coefficient to the ground, the heat fluxes in the transient releases were 15% to 20% higher than in the constant releases. With heat transfer coefficient to the ground of $500 \text{ W/m}^2\text{K}$, it was the other way around. Again, the simulations with a surrounding water pool gave somewhat higher heat fluxes, but it is unclear if this was caused by other effects, such as the averaging interval or numerical differences. The simulations with a heat transfer coefficients of $500 \text{ W/m}^2\text{K}$ and $300 \text{ W/m}^2\text{K}$ gave a rather large «spike» in the radiation release varying between 10 s and 30 s into the simulation. This made it difficult to find a suitable averaging interval, especially for the transient releases. In the case of an LNG leakage, the maximum radiative heat flux might be of equal, if not higher, importance compared to the time-averaged heat fluxes. Two simulations were found to best fit the heat fluxes from the experiment, both liquid, transient releases without a surrounding water pool. One had adiabatic conditions to the ground below, letting the radiative and convective effects of the air handle the vaporization. The other had a heat transfer coefficient to the ground of $100 \text{ W/m}^2\text{K}$.

So far in this discussion, the mean heat flux over all four spokes have been used for comparing to the Phoenix experiment. However, the heat flux could vary significantly over the various spokes. In the Phoenix experiment, the south spoke had the highest heat fluxes for all three measurement distances on the spoke, almost twice as high as the north spoke, which measured the lowest values. This ratio of the high-to-low values of heat fluxes were not seen in any of the simulation, with the averaged south spoke heat flux at most being a factor of 1.6 higher than the north spoke. However, consistent with the Phoenix experiment, the south spoke generally obtained the highest heat fluxes, and the north spoke the lowest. This was expected, due to the wind blowing at an angle of 15° counterclockwise from the north spoke.

For all but one simulation, the west spoke heat fluxes were from just under 10% to almost 20% higher than the east spoke, inconsistent with the direction of the wind and the results from the Phoenix experiment. However, the east-west component of the wind in the Phoenix experiment, corresponding to the x -component in the simulations, was rather small compared to the north-south/ y -component. In the Phoenix experiment, the effect of the flame «anchoring» itself to the discharge pipes was prominent, and it is suggested that this both stabilized the flame, as well as dragging it towards the south-southeast, as these pipes were situated at a 45° angle directly between the south and east spokes. This effect was not seen in any of the simulations, and may explain both this difference in east-west spoke heat flux, as well as the generally higher fluctuations seen in the heat fluxes from the simulation than in the experiment. By looking at Figs. 4.3, 4.4 and 4.6 from the simulations with the «old» soot model and Figs. 4.7 and 4.8 with the modified soot model, it is clear that all fluctuate quite a lot more than

the heat fluxes from the Phoenix experiment, Fig. A.7.

The morphology of the flame was investigated for the transient, liquid releases, and had both similarities and differences to the Phoenix experiment. Similarities included, for the most part, the width and tilt of the flame. Both were somewhat fluctuating during the individual simulations, and from one simulation to another. Some flame tilting was observed, mostly along the direction of the wind. A qualitative analysis determined that, on average, it was negligible compared to the buoyancy effects caused by the combustion. The width of the flame at some altitude during a near-steady interval varied between 45 m and 60 m, depending on the simulation and the altitude. This was significantly narrower than the base of the plume, which was equal to the LNG pool area at any instance. Again, this was consistent with the Phoenix experiment.

The main differences regarding the morphology of the flame was the centroid shift and total height of the plume. In the Phoenix experiment, the centroid on vertical axis varied between 40 m and 60 m, whereas in the simulations the centroid on the vertical axis fluctuated greatly between 50 m and almost 120 m. An average plume height of 146 m and maximum height of approximately 200 m were seen in the Phoenix experiment. In the KFX simulations, the tip of the plume rarely, if ever, dropped below 150 m, and a maximum height of 300 m was observed at some instances. Again, this is believed to be due to the lack of flame anchoring. With this effect, the base of the flame would likely be greatly stabilized, dampening the fluctuations and «pulling» the flame towards the ground. A possible cause for the lack of this effect was the grid resolution. If the grid resolution was too coarse, the turbulence effects believed to cause this would not be realistically included. However, after several rounds of grid refinement, flame anchoring was not witnessed, likely ruling out any grid dependence on this effect.

As noted, the pool model implemented in KFX has limitations in handling multicomponent pools. Therefore, the water pool onto which the LNG was release was modeled as a flat ground, with various heat transfer coefficients based on experimental data to emulate the heat transfer between the water and the LNG. The pool spreading and maximum area from the liquid, transient simulations were compared to the data from the Phoenix area. It was found that the maximum area for the simulations with adiabatic conditions between the LNG and the ground reached a similar maximum area, equivalent to a circular diameter of 83 m. This was reached after approximately 60 s. The simulations with heat transfer coefficients of 100 W/m²K, 300 W/m²K and 500 W/m²K reached significantly lower areas, with the simulation with a heat transfer coefficient of 500 W/m²K having the lowest maximum area, with an equivalent circular diameter of approximately 67 m.

In the transient simulations, the LNG release ended at 150 s. At this time, the pool area for all simulations was very small, and all LNG was vaporized by 170 s. This is far sooner than in the Phoenix experiment. The maximum area was reached at approximately 170 s after the initial LNG release, and the fire had a total duration of over 400 s. No data for the pool area is given after 240 s, likely due to break-up of the LNG into the water, making it difficult to separate the LNG

from the water in the post-experiment video analysis determining the LNG pool area.

It is noted [3] that in the smaller, 21 m pool diameter LNG experiment *LNG Test 1*, two-phase flow effects were prominent in the LNG flow through the discharge pipes. For the larger experiment, measures were taken to reduce these effects, and to include some two-phase effects in the pre-test calculations. However, this is still an uncertainty in the experiment. Additionally, the LNG release rate was calculated from a height reduction of the liquid surface inside the LNG reservoir, and these measurements were based on pressure head from a dip tube and the laser-determined volume vs. liquid height measurements [3], and by using a constant liquid methane density of 420 kg/m^3 . This mass flow was approximated by a release curve for the computations in KFX, adding an additional source of error. Including uncertainties due to possible two-phase flow effects and a time delay due to the almost 100 m length of the discharge pipes the LNG had to pass through, a question could be posed whether this mass release follows the same curve at the end of the discharge pipes as inside the reservoir. In KFX, the LNG release cells are equivalent to the end of the discharge pipes, and the curve used for approximating the mass flow rate might be of both different shape and length, than the curve obtained from inside the reservoir. Still, given that the duration of the fire was almost 250 s longer in the experiment than any of the KFX simulations, these uncertainties are thought to be of secondary importance to the pool spreading model.

The too high spreading rate of the LNG is thought to be a source of error for the other investigations as well, such as the flame morphology. The spreading rate likely caused the vaporization of LNG in the simulations to exceed the assumed vaporization rate of $0.147 \text{ kg/m}^2\text{s}$ in the experiment. A too high vaporization rate would, in turn, cause a too high influx of fuel into the domain, increasing the total combustion rate, elongating the flame to unphysical heights. Evidence of the higher vaporization rate in the simulations is found when comparing the duration of the simulation to the duration of the experiment. As the experiment outlasted the simulations with about 250 s with the same amount of total LNG release, this points to an unphysically high vaporization rate in the simulations.

In Sec. 7.1, a new, relatively simple, model for LNG pool spreading through water was developed. The model gives the radial velocity, or front velocity, of the LNG pool on top of a water pool as a function of the density differences of the two liquids and the thickness of the LNG. It assumes a circular pool and uniform thickness of the LNG, and does not include heat transfer between the LNG and the water or air. Based on initial numerical computations, this model gives very promising results. However, due to its formulation and simplicity, it bears some weaknesses. One weakness is due to the fact that the front velocity of the LNG is proportional to the square root of the LNG pool thickness, therefore not allowing retraction of the LNG pool. Other weaknesses include the assumptions of uniform LNG pool thickness and perfectly circular spreading. As noted, heat transfer and/or vaporization rate of the LNG is not included in the model, and needs to be included by other means. This model was compared to an established

model for oil/LNG pool spreading on water, and was found to be a better fit for the LNG pool area from the Phoenix experiment than the model to which it was compared. Both the model developed and the one which it was compared to are only valid for the gravity-inertia regime of the spreading phase, where gravitational and inertial forces are approximately equal, and assume that most of the cryogenic liquid will evaporate before the other two identified regimes, the gravity-viscous regime, where the gravitational and viscous forces are similar, and the surface tension regime, where the viscous and drag forces are of dominant, are reached. Relations for the pool radius as a function of mass flow, fluid properties and time were introduced for the gravity-inertia and the gravity-viscous regimes, as well as a transition time between the two. These were not tested numerically, but suggested as a topic for further investigation and possible improvement of the multicomponent pool spreading model in KFX.

9 Conclusions and Further Work

9.1 Conclusions

The KFX CFD software has been found to have several strengths and weaknesses when simulating a large-scale LNG release with subsequent combustion.

When monitoring the radiative heat fluxes at typical hazard distances for a large-scale LNG pool fire, they were initially found to be of magnitude one half to one quarter of the experimentally obtained values. This was found to be caused by an unphysical high concentration of soot just outside the flame. With a modification to the soot model, increasing the combustion of soot particles, the radiative heat fluxes were found to be in accordance with the experimental values.

If such a modification is cumbersome to implement, a guideline temperature of 1100 K for the KFX option *T_{cut}(K) for absorption* for soot should be recommended, opposed to the standard value of 0 K. This option prevents the emission and absorption of soot at temperatures below the given value, increasing the radiation release from the flame to the surroundings.

A potential for improvement in KFX is the pool spreading model. In all simulations, the LNG spread at a far higher rate compared to the experimental values. Consequently, the total duration of the pool fire in all simulations were less than half of that in the experiment.

Due to limitations in the multicomponent pool model (e.g. LNG and water), unphysical results were obtained when simulating an LNG release in an existing pool of water. Therefore, the LNG release has to be defined on a flat surface. As an effect, the physics of the LNG having to displace the surrounding water in order to spread were not included, which likely caused the erroneous spreading rates. For a physical representation of this, a multi- or two-component pool model of LNG and water should be implemented into KFX. If this is not realizable, an option could be included where the solid ground is defined as «water», and a limiting factor to the pool spreading rate in the model could be introduced.

A prominent effect in the experiment was the flame anchoring itself to the discharge pipes leading onto the water. This effect was not seen in any of the simulations. The grid resolution was initially thought to cause this lack of flame anchoring, due to the turbulent structures needing a sufficiently fine grid to be realistically simulated. However, despite several rounds of grid refinement, the effect of flame anchoring was not seen.

The morphology (height, width, tilt and general shape) of the simulated flame was also investigated. The width and tilt were comparable to the experiment. The flame was highly elongated and experienced large fluctuations in the centroid shift along the vertical axis compared to the experiment. This is likely as a result of the high pool spreading rate and lack of flame anchoring. With the effect of flame anchoring, the fire would likely be greatly stabilized, dampening the amplitude of the fluctuations in the centroid shift. The high pool spreading rate lead to a too high vaporization rate of the LNG, likely causing the influx of fuel into the domain to be higher than realistic values. This increased amount of fuel available for combustion in turn led to a larger and higher plume.

A new model for LNG spreading through water was introduced. This model includes the physics of the LNG having to displace the surrounding water in order to spread. The model was numerically tested and compared to values from the experiment. These preliminary results were highly promising, and should be further investigated in order for a possible implementation into KFX.

9.2 Recommendations for Further Work

The work done in this thesis could be used as a foundation for further work. The following investigations may be of interest:

- Validation of the radiative heat fluxes with the modified soot model against large-scale experiments other than the Phoenix series LNG Test 2.
- Investigation into the effects and physics of flame anchoring, including a literature study. A starting point could be a parametric study of the various input parameters in KFX, including, but not limited to:
 - The turbulence viscosity
 - The eddy viscosity
 - Initial values for k and ε
 - A detailed grid and time step analysis
 - Convergence criteria of the equation solvers in KFX

Additionally, various simulations may be performed as a steady, liquid release (as opposed to a transient release) for a number of different input parameters, and then running the simulations until steady-state for comparison.

- Further work on a multicomponent pool model for KFX. As an LNG leakage likely would be in a marine environment, a realistic pool model for a two-specie mixture would be of great benefit, and likely a competitive advantage. A starting point could be the new pool spreading model developed, for a possible combination with the currently implemented pool spreading model in KFX.

Bibliography

- [1] Abramowitz, M. and Stegun, I. A. (1972). *Handbook of Mathematical Functions*. United States Department of Commerce, National Bureau of Standards, 10th edition.
- [2] Blanchat, T. (2011). Summary of the Phoenix Series Large Scale LNG Pool Fire Experiments. In *23rd International Colloquium on the Dynamics of Explosions and Reactive Systems, July 24-29, 2011*, Irvine, California, USA.
- [3] Blanchat, T., Helmick, P., Jensen, R., Luketa, A., Deola, R., Suo-Anttila, J., Mercier, J., Miller, T., Ricks, A., Simpson, R., Demosthenous, B., Tiszen, S., and Hightower, M. (2011). The Phoenix Series Large Scale LNG Pool Fire Experiments. Technical report, Sandia National Laboratories, Albuquerque, New Mexico, USA.
- [4] Dellinger, B., D'Alessio, A., D'Anna, A., Ciajolo, A., Gullett, B., Henry, H., Keener, M., Lighty, J., Lomnicki, S., Lucas, D., Oberdörster, G., Pitea, D., Suk, W., Sarofim, A., Smith, K., Stoeger, T., Tolbert, P., Wyzga, R., , and Zimmermann, R. (2008). Combustion byproducts and their health effects: Summary of the 10th international congress. *Environmental Engineering Science*, 25(8):1107–1114.
- [5] Ertesvåg, I. S. (1991). *Utvikling av turbulensmodell for låge reynoldstal med likning for reynoldsspenningane og likning for karakteristisk frekvens*. PhD thesis, NTH, Insitutt for teknisk varmelære.
- [6] Ertesvåg, I. S. (2000). *Turbulent strøyming og forbrenning*. Tapir Akademisk Forlag, Trondheim.
- [7] Hamming, R. W. (1973). *Numerical Methods for Scientists and Engineers*. Dover Publications, Inc., New York, 2nd edition.
- [8] Incropera, F. P., Dewitt, D. P., Bergman, T. L., and Lavine, A. S. (2013). *Principles of Heat and Mass Transfer*. John Wiley & Sons, Inc., 7th edition.
- [9] Jakobsen, H. A. (2014). *Chemical Reactor Modeling: Multiphase Reactive Flows*. Springer, 2nd edition.

- [10] Johnsson, J., Olofsson, N. E., Bladh, H., and Bengtsson, P. E. (2015). Laser-induced incandescence (LII). <http://www.forbrf.lth.se/english/research/measurement-methods/laser-induced-incandescence-lii/>. Accessed: 2016-04-22.
- [11] Jones, W. P. and Launder, B. E. (1972). Kinetics of dispersed carbon formation. *International Journal of Heat and Mass Transfer*, 15:301–314.
- [12] Kundu, P. K., Cohen, I. M., and Dowling, D. R. (2012). *Fluid Mechanics*. Academic Press, 5th edition.
- [13] Launder, B. E. and Spalding, D. (1974). The numerical computation of turbulent flows. *Computer Methods in Applied Mechanics and Engineering*, 3:269–289.
- [14] Leckner, B. (1972). Spectral and total emissivity of water vapor and carbon dioxide. *Combustion and Flame*, 19:33–48.
- [15] LeVeque, R. (2002). *Finite Volume Methods for Hyperbolic Problems*. Cambridge University Press, 1st edition.
- [16] Lockwood, F. and Shah, N. (1981). A new radiation solution method for incorporation in general combustion prediction procedures. *Eighteenth Symposium (Int.) on Combustion*, pages 1405–1414.
- [17] Magnussen, B. (1981). On the structure of turbulence and a generalized eddy dissipation concept for chemical reaction in turbulent flow. In *19th American Institute of Aeronautics and Astronautics Science Meetings, January 12-15, 1981*, St. Louis, Missouri, USA.
- [18] Magnussen, B. and Hjertager, B. (1976). On mathematical modeling of turbulent combustion with special emphasis on soot formation and combustion. *Sixteenth Symposium (Int.) on Combustion*, 16:719–729.
- [19] Magnussen, B. F. (1989). Modeling of NO_x and soot formation by the Eddy Dissipation Concept. In *International Flame Research Foundation, First Topic Oriented Technical Meeting*, Amsterdam, Netherlands.
- [20] Magnussen, B. F. (2005). The Eddy Dissipation Concept - a bridge between science and technology. In *ECCOMAS Thematic Conference on Computational Combustion, Lisbon*.
- [21] Magnussen, B. F. (2016). Private notes.
- [22] Magnussen, B. F., Lilleheie, N. I., Vembe, B. E., L. B., Grimsmo, B., A., L. L., Kleiveland, R., Rian, K. E., Olsen, R., and Evanger, T. (2010). Numerical computation of large scale fires and fire mitigation – from combustion science to industry application. In *6th International Seminar on Fire and Explosion Hazards*, Leeds, UK.
- [23] MATLAB (2014). *Version 8.4.0 (R2014b)*. The MathWorks Inc., Natick, Massachusetts.

- [24] Mills, A. F. (1995). *Heat and Mass Transfer*. Irwin, 1st edition.
- [25] Modest, M. F. (2013). *Radiative Heat Transfer*. Academic Press, 3rd edition.
- [26] Mudan, K. S. (1984). Thermal radiation hazards from hydrocarbon pool fires. *Progress in Energy and Combustion Science*, 10:59–80.
- [27] Myrmo, Ø. (2011). Numerical modeling of pool spreading, heat transfer and evaporation in liquefied natural gas (LNG). Master's thesis, Norwegian University of Science and Technology (NTNU).
- [28] Orloff, L., Modak, A. T., and Markstein, G. H. (1979). Radiation from smoke layers. *Symposium (International) on Combustion*, 17:1029–1038.
- [29] Pai, S.-I. (1966). *Radiation Gas Dynamics*. Springer-Verlag, 1st edition.
- [30] Pope, S. S. (2013). *Turbulent Flows*. Cambridge University Press, 11th edition.
- [31] Skinnemoen, M. M. (2015). LNG safety - leakage, spreading and fire. Project Thesis, Norwegian University of Science and Technology (NTNU).
- [32] Tesner, P. A., Smegiriova, T. D., and Knorre, V. G. (1971a). Kinetics of dispersed carbon formation. *Combustion and Flame*, 17:253–260.
- [33] Tesner, P. A., Tsygankova, E. I., Guilazetdov, L. P., Zuyev, V., and Loshakova, G. (1971b). The formation of soot from aromatic hydrocarbons in diffusio flames of hydrocarbon-hydrogen mixtures. *Combustion and Flame*, 17:279–285.
- [34] Vembe, B., Rian, K., Holen, J., Lilleheie, N., Grimsmo, B., and Myhrvold, T. (2001). *Kameleon FireEx 2000 Theory Manual*. ComputIT AS.
- [35] Vembe, B. E., Kleiveland, R. N., Grimsmo, B., Lilleheie, N. I., Rian, K. E., Olsen, R., Lakså, B., Nilsen, V., Vembe, J. E., and Evanger, T. (2014). *KFX Furcifier - User Manual*. ComputIT AS.
- [36] Versteeg, H. and Malalasekera, W. (1995). *An Introduction to Computational Fluid Mechanics - The Finite Volume Method*. Longman Scientific & Technical, 1st edition.
- [37] Woodward, J. L. and Pitblado, R. M. (2010). *LNG Risk Based Safety – Modeling and Consequence Analysis*. John Wiley & Sons, Inc.

A Appendix A

Various figures.

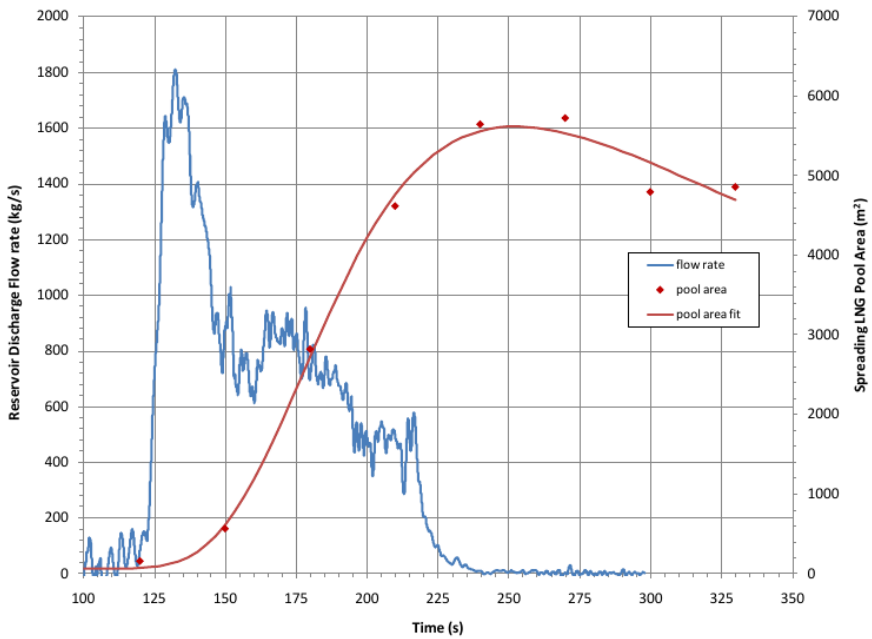


Figure A.1: Time series of LNG pool area and mass flow discharge from the reservoir. From [3].

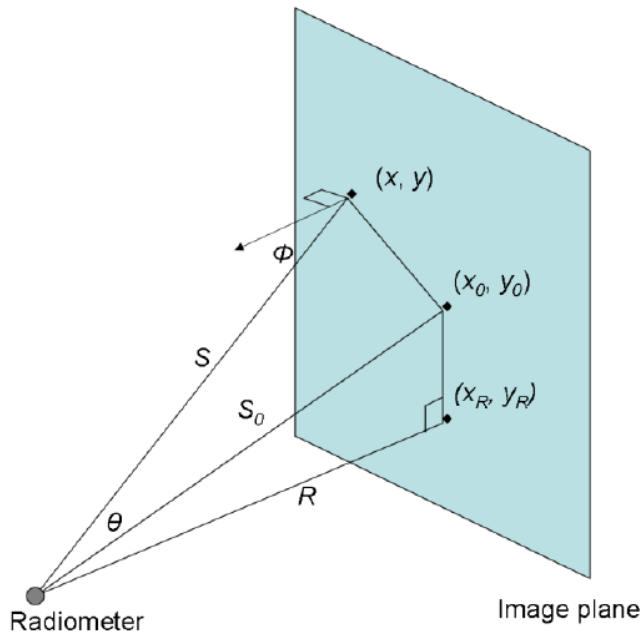
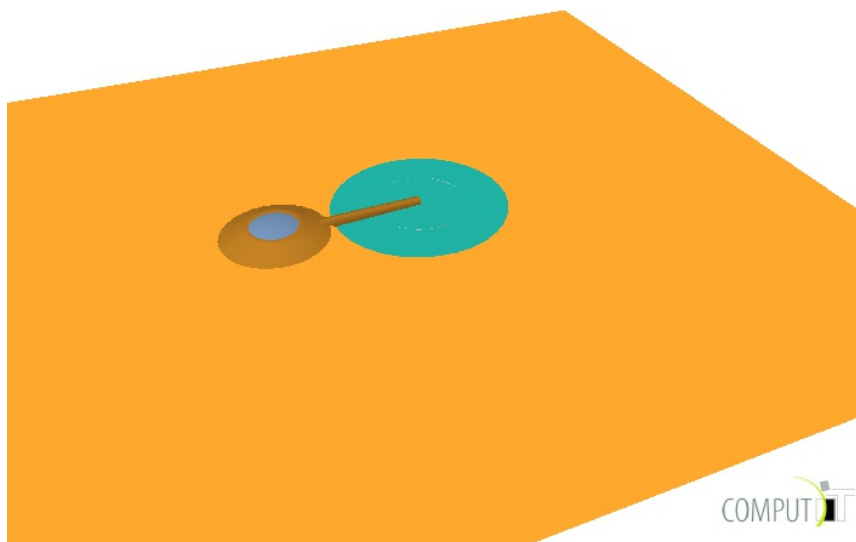
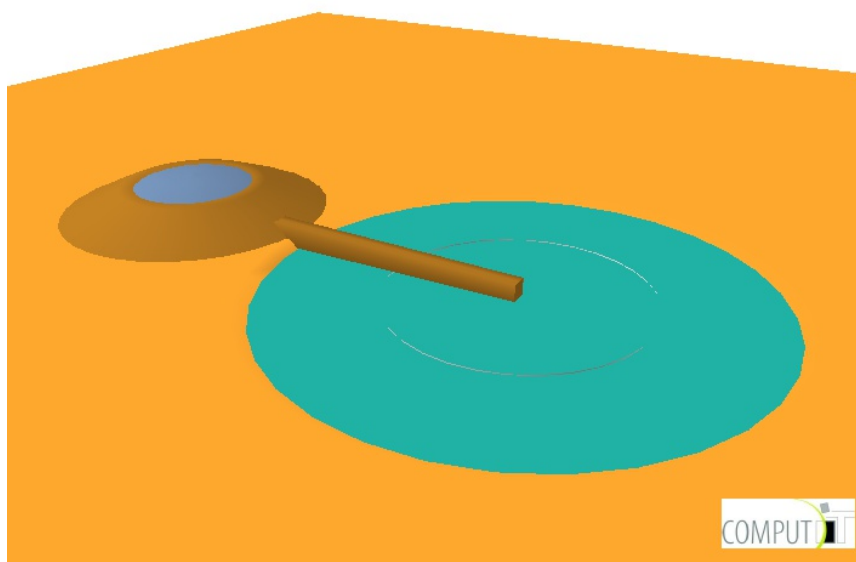


Figure A.2: Image plane used for image processing for finding the surface emissive powers in the two LNG fire experiments. From [3].



(a) Overview view.



(b) Close-up view.

Figure A.3: The test site used in most of simulations performed.

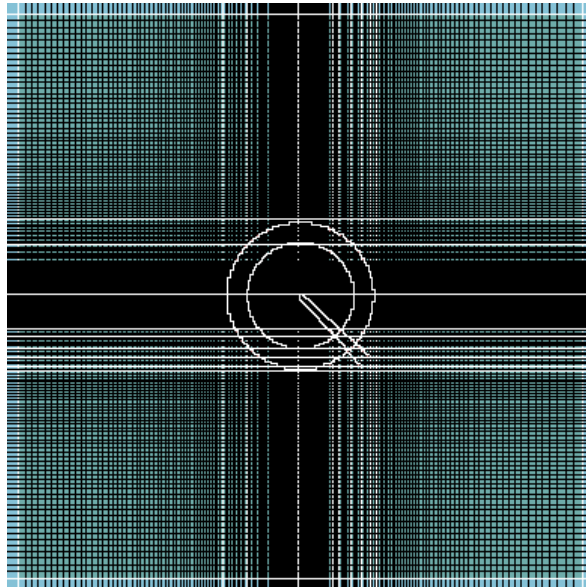


Figure A.4: Grid distribution in the full x - y plane. White lines indicate «locked» grid lines at locations in the domain, preventing scaling errors around important geometry when changing grid sizes.

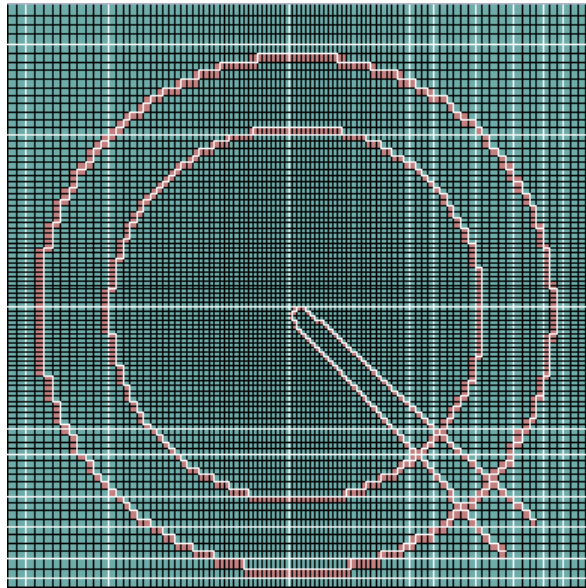


Figure A.5: Zoomed in view over the pool enclosure, showing grid distribution. Pool enclosure and discharge pipes can be seen as red nodes. White lines indicate «locked» grid lines at locations in the domain, preventing scaling errors around important geometry when altering the grid.

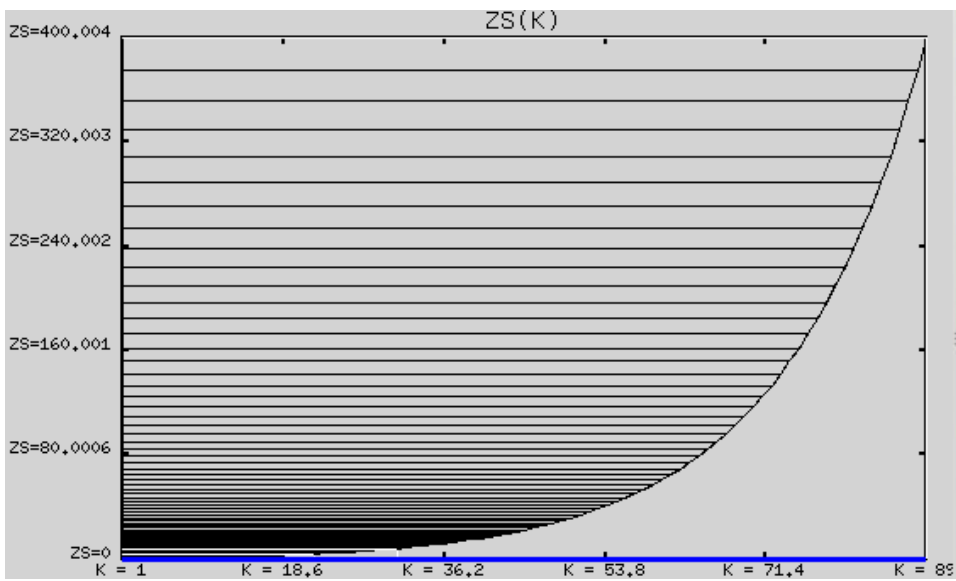
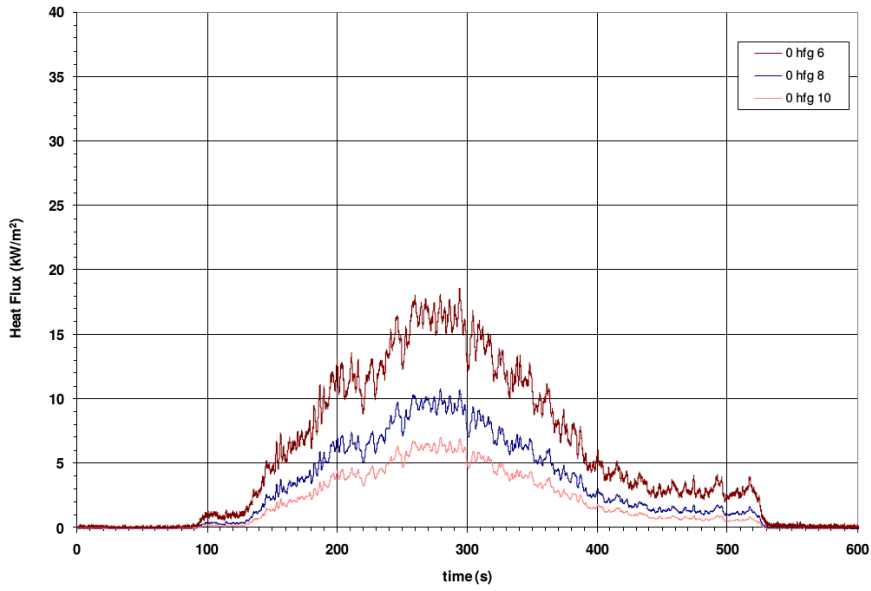
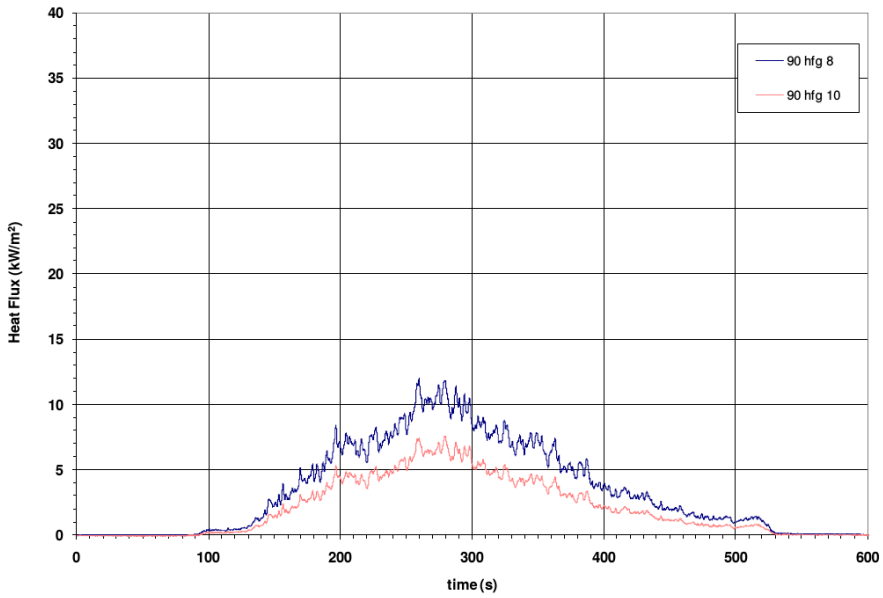


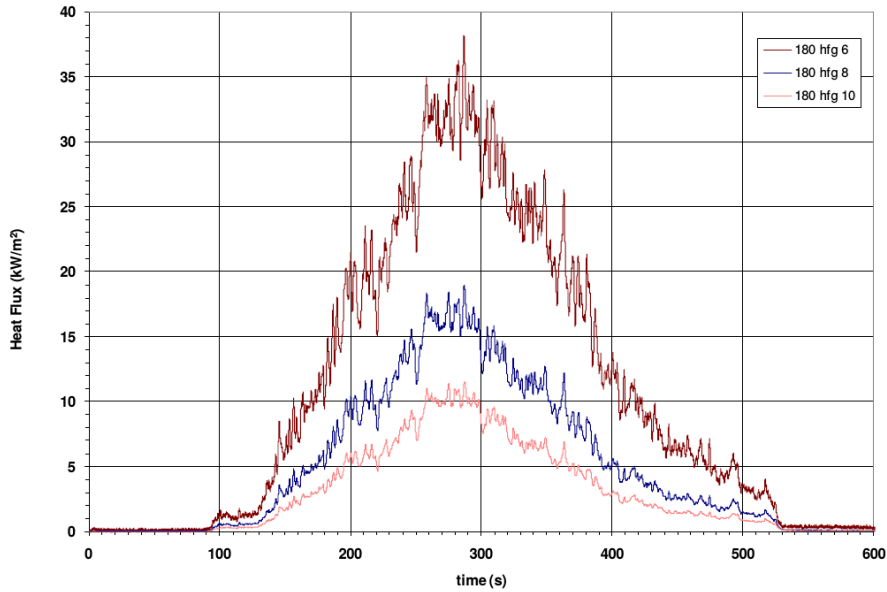
Figure A.6: Graphical representation of the grid distribution in the z -direction. Vertical axis: altitude. Horizontal axis: node number from the lower boundary. Each horizontal line indicates a boundary between cells.



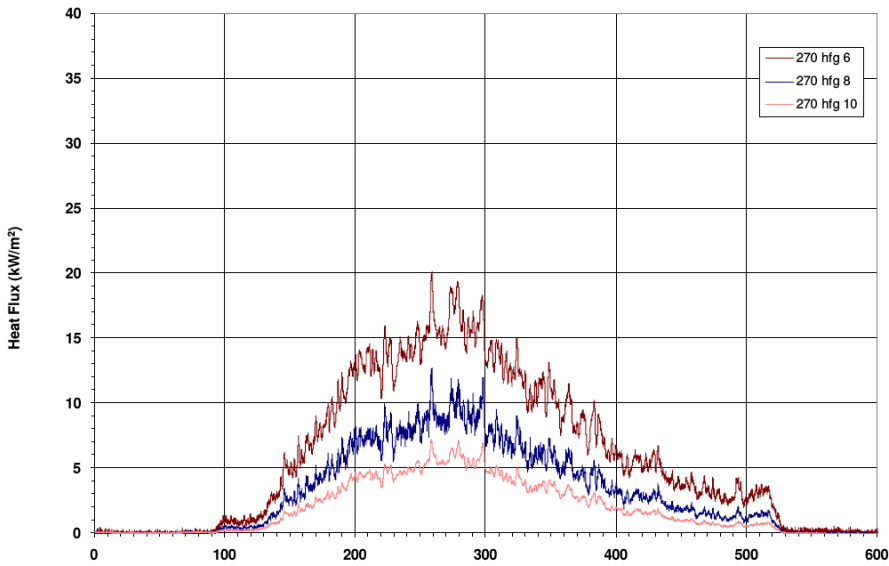
(a) North spoke heat flux.



(b) East spoke heat flux.



(c) South spoke heat flux.



(d) West spoke heat flux.

Figure A.7: Radiative heat fluxes measured in the Phoenix experiment. $[x]$ hfg $[y]$ indicate the various instrumentation towers. $[x]$ is the clockwise angle in degrees from the north spoke, hfg is short for heat flux gauge. $[y]$ denotes the individual towers on each spoke, with 6, 8 and 10 being the towers at 110 m, 160 m and 210 m from the pool center, respectively. From [3].

B Appendix B - Videos and simulations

B.1 Links to Videos of the SNL Phoenix LNG Experiments

Video A: Phoenix Series Liquefied Natural Gas Pool Fire Experiments

<https://vimeo.com/105661774>

Duration: 6m20s

Video B: Phoenix Series LNG Pool Fire Presentation Clips

<https://vimeo.com/105661775>

Duration: 1m53s

Video C: Phoenix Series LNG Pool Fire Clips¹

[http://digitalops.sandia.gov/Mediasite/Play/](http://digitalops.sandia.gov/Mediasite/Play/aad7a52ad14e4cb38bc2fca86d044ea61d?catalog=7402e84d-48e4-467e-813c-0ecd42ca3d08)

[aad7a52ad14e4cb38bc2fca86d044ea61d?](http://digitalops.sandia.gov/Mediasite/Play/aad7a52ad14e4cb38bc2fca86d044ea61d?catalog=7402e84d-48e4-467e-813c-0ecd42ca3d08)

[catalog=7402e84d-48e4-467e-813c-0ecd42ca3d08](http://digitalops.sandia.gov/Mediasite/Play/aad7a52ad14e4cb38bc2fca86d044ea61d?catalog=7402e84d-48e4-467e-813c-0ecd42ca3d08)

Duration: 11m15s

Description:

00:00 Ground View

05:58 Ground View @ 2.5x

08:55 Ground View Clip :30

09:28 90 degree Aerial View :30

10:00 90 degree Aerial View :17

10:19 270 degree Aerial View :30

10:51 270 degree Aerial View :17

¹Most easily found by performing a Google search with the search string "Phoenix Series LNG Pool Fire Clips" (in quotes).

B.2 Animations of KFX simulations

sim23

Animation 0

<https://youtu.be/MuhWAnymn4k>

Opacity = 0.7

Duration: 4m06s

sim31

Animation 1

https://youtu.be/xB4RsflQ_A

Opacity = 0.3

Duration: 3m02s

Animation 2

<https://youtu.be/XjxeZOJyqI>

Opacity = 0.7

Duration: 3m02s

Animation 3

https://youtu.be/Nz9_jZsA6X8

Opacity = 0.3

Cut in plane $z = 0.6$ m

Duration: 3m02s

C Appendix C

C.1 MATLAB Codes and Scripts

Note: if trying to run these scripts, an error message will be displayed. The command `loaddata` needs the input of the strings in the `input=[...]` vector, to load the various data files.

C.1.1 Method 1

```
1 %% Poolarea_diff
2 % Solves equation for LNG pool spreading through water
3
4 %{
5   Loads data for LNG mass flow and data from the Phoenix
6   experiment for comparison when plotting
7   %{
8   input = [{'release'} {'SNL'}];
9   loaddata
10
11 % Setting time domain, time step, constant and
12   coefficients
13 tmax = 250;
14 tmin = 1;
15 tstep = 1;
16 mdot_evap = 0.147; % kg/m^2s
17 rho = 420; % kg/m^3
18 C = 1.30; % m^0.5/s
19 tplot = tmin:tstep:tmax;
20 C1 = C*sqrt(pi/rho);
21
22 %{
23   Interpolating the LNG release to produce a vector with
24   the same size as the time domain
25   %}
```

```
23 rel_cum = interp1(t_rel,rel_tot,tplot);
24 m_in = rel_cum;
25 mt = tplot;
26 %{
27     Finding NaN values after the end of the release, where
        m_in is not defined, and setting these equal to the
        last element in the vector
28 %}
29 TF = isnan(m_in);
30 m_in(TF) = max(m_in);
31
32 %{
33     Setting initial conditions for r(t) and g(t), to 9 m
        and 81 m^2, respectively. Setting numerical
        tolerances. Solving the set of ODEs by the vector u
        = [r(t); g(t)] by the solver ode45. Defining the
        ODEs in the function myode2.
34 %}
35 ic = [9 81];
36 opts = odeset('RelTol',1e-2,'AbsTol',1e-6);
37 [t,u] = ode45(@(t,u) myode2(t,u,C1,mdot_evap,mt,m_in),
        tplot, ic, opts);
38
39 % Getting values for r(t) and g(t) from the vector u
40 r = u(:,1); % = r(t)
41 g = u(:,2); % = g(t)
42
43 % Calculating the area as a function of time based on
        the radius
44 A = pi*r.^2;
45 %{
46     Calculating the mean pool thickness as a function of
        time based on the relation (mass in - mass out)/(
        density * area)
47 %}
48 delta = (m_in - mdot_evap*cumtrapz(t,A))./(rho*A');
49 % Calculation the radial, or frontal, velocity
50 v = C*delta.^(1/2);
51
52 %{
53     Finding the time where the solution becomes complex, by
        finding where the first entry either the r vector
        or A vector reaches a certain tolerance
54 %}
55 r_imag = find(abs(imag(r)) > eps*10e+10);
```

```
56 r_imag = r_imag(1);
57 A_imag = find(abs(imag(A)) > eps*10e+10);
58 A_imag = A_imag(1);
59 t_imag = min([r_imag A_imag]);
60
61 %{
62     Plotting the radius vector vs. time. Marking where the
        solution becomes complex.
63 %}
64 figure
65 subplot(2,2,1)
66 plot(t,real(r),'.-','Color',[0 0.4470 0.7410])
67 axis([tmin tmax 0 50])
68 y1=get(gca,'ylim');
69 hold on
70 ax = gca;
71 ax.XTick = 0:40:tmax;
72 ax.YTick = 0:10:50;
73 plot([t_imag t_imag],y1,'Color',[0 0.5 0],'LineWidth',2)
74 xlabel('t [s]')
75 ylabel('r [m]')
76 title('Pool radius, Method 1')
77 hold off
78
79 %{
80     Plotting the area vector vs. time. Marking where the
        solution becomes complex.
81 %}
82 subplot(2,2,2)
83 plot(t,real(A),'.-r','Color',[0.8500 0.3250
        0.0980])
84 axis([tmin tmax 0 7000])
85 y1=get(gca,'ylim');
86 hold on
87 ax = gca;
88 ax.XTick = 0:40:tmax;
89 ax.YTick = 0:1000:7000;
90 plot(t_ex,area_ex,'Color',[0.5 0.5 0.5],'LineWidth',2)
91 plot([t_imag t_imag],y1,'Color',[0 0.5 0],'LineWidth',2)
92 xlabel('t [s]')
93 ylabel('A [m^2]')
94 title('Pool area, Method 1')%
95 hold off
96
97 %%
```

```

98 | Plotting the mean thickness vector vs. time. Marking
    | where the solution becomes complex.
99 | %}
100 | subplot(2,2,3)
101 | plot(t,real(delta)*1000,'.-b','Color',[0.9290    0.6940
    |         0.1250])
102 | axis([tmin tmax -50 100])
103 | y1=get(gca,'ylim');
104 | hold on
105 | ax = gca;
106 | ax.XTick = 0:40:tmax;
107 | ax.YTick = -50:25:100;
108 | plot([t_imag t_imag],y1,'Color',[0 0.5 0],'LineWidth',2)
109 | xlabel('t [s]')
110 | ylabel('\delta [mm]')
111 | title('Mean pool depth, Method 1')
112 | hold off
113 |
114 | %{
115 | Plotting the front velocity vector vs. time. Marking
    | where the solution becomes complex.
116 | %}
117 | subplot(2,2,4)
118 | plot(t,real(v),'.-','Color',[0.4940    0.1840
    |         0.5560])
119 | axis([tmin tmax 0 0.4])
120 | y1=get(gca,'ylim');
121 | hold on
122 | ax = gca;
123 | ax.XTick = 0:40:tmax;
124 | ax.YTick = 0:0.1:0.4;
125 | plot([t_imag t_imag],y1,'Color',[0 0.5 0],'LineWidth',2)
126 | xlabel('t [s]')
127 | ylabel('v [m/s]')
128 | title('Front velocity, Method 1')
129 | hold off

```

```

1 | function dudt=myode2(t,u,C1,mdot_evap,mt,m_in) %Called
    | by "poolarea_diff.m"
2 | % Defines the vector of ODEs, u. u(1) = r(t), u(2) = g(t
    | ).
3 | dudt = zeros(2,1);
4 | m_in = interp1(mt,m_in,t); % Interpolate the data set (
    | mt,m) at time t
5 | % Defining the ODEs

```



```

6 dudt(1) = C1*( (m_in - pi*mdot_evap* u(2)) ).^(1/2) / (
    pi*u(1) );
7 dudt(2) = u(1).^2;
8 end

```

C.1.2 Method 2

```

1  %% poolradius_diff.m
2  % Solves equation for LNG pool spreading through water
3
4
5  %{
6  Loads data for LNG mass flow and data from the Phoenix
    experiment for
7  comparison when plotting
8  %}
9  input = [{'release'} {'SNL'}];
10 loaddata
11
12 % Setting time domain, time step, constant and
    coefficients
13 tmax = 250;
14 tmin = 1;
15 tstep = 1;
16 mdot_evap = 0.147; % kg/m^2s
17 rho = 420; % kg/m^3
18 C = 1.30;
19 tplot = tmin:tstep:tmax; % s
20
21 %{
22 Interpolating the instantaneous and time integrated LNG
    release to produce a vector with the same size as the
    time domain
23 %}
24 rel = interp1(t_rel,rel,tplot);
25 mdot_in = rel; % g=g(t), rel_cum=rel_cum(t)
26 rel_cum = interp1(t_rel,rel_tot,tplot);
27 m_in = rel_cum;
28 % Interpolating intervall of the mass flow
29 mt = tplot;
30
31 %{
32 Finding NaN values after the end of the releases, where
    mdot_in and m_in is not defined, and setting these

```

```

    equal to the last element in the vector
33 %}
34 TF = isnan(mdot_in);
35 mdot_in(TF) = 0;
36 tf = isnan(m_in);
37 m_in(tf) = max(m_in);
38
39 %{
40 Setting initial conditions for the radius and thickness
    to 9 m and 1e-3 m, respectively. Setting numerical
    tolerances. Solving the set of ODEs by the vector u =
    [r(t); delta(t)] by the solver ode45. Defining the
    ODEs in the function myode3.
41 %}
42 ic = [9 1.0e-3];
43 opts = odeset('RelTol',1e-2,'AbsTol',1e-6);
44 [t,u]=ode45(@ (t,u) myode3(t,u,C,mdot_evap,rho,mt,mdot_in
    ,m_in),...
45     tplot,ic,opts);
46
47 % Getting values for r(t) and delta(t) from the vector u
48 r = u(:,1);
49 delta = u(:,2);
50
51 % Calculating the area as a function of time based on
    the radius
52 A = pi*r.^2;
53 % Calculating the fron velocity as a function of time
    based on the radius
54 v = C*delta.^(1/2);
55
56 %{
57 Finding the time where the solution becomes complex, by
    finding where the first entry either the r vector or
    A vector reaches a certain tolerance
58 %}
59 r_imag = find(abs(imag(r)) > eps*10e+10);
60 r_imag = r_imag(1);
61 A_imag = find(abs(imag(A)) > eps*10e+10);
62 A_imag = A_imag(1);
63 d_imag = find(abs(imag(delta)) > eps*10e+10);
64 d_imag = d_imag(1);
65 t_imag = min([r_imag A_imag d_imag]);
66
67 %{

```

```
68 | Plotting the radius vector vs. time. Marking where the
    | solution becomes complex.
69 | %}
70 | figure
71 | subplot(2,2,1)
72 | plot(t,real(r),'.-','Color',[0 0.4470 0.7410])
73 | axis([tmin tmax 0 50])
74 | y1=get(gca,'ylim');
75 | hold on
76 | ax = gca;
77 | ax.XTick = 0:40:tmax;
78 | ax.YTick = 0:10:50;
79 | plot([t_imag t_imag],y1,'Color',[0 0.5 0],'LineWidth',2)
80 | xlabel('t [s]')
81 | ylabel('r [m]')
82 | title('Pool radius, Method 2')
83 | hold off
84 |
85 | %{
86 | Plotting the area vector vs. time. Marking where the
    | solution becomes complex.
87 | %}
88 | subplot(2,2,2)
89 | plot(t,real(A),'.-r','Color',[0.8500 0.3250
    | 0.0980])
90 | axis([tmin tmax 0 7000])
91 | y1=get(gca,'ylim');
92 | hold on
93 | ax = gca;
94 | ax.XTick = 0:40:tmax;
95 | ax.YTick = 0:1000:7000;
96 | plot(t_ex,area_ex,'Color',[0.5 0.5 0.5],'Linewidth',2)
97 | plot([t_imag t_imag],y1,'Color',[0 0.5 0],'LineWidth',2)
98 | xlabel('t [s]')
99 | ylabel('A [m^2]')
100 | title('Pool area, Method 2')%
101 | hold off
102 | %{
103 | Plotting the mean thickness vector vs. time. Marking
    | where the solution becomes complex.
104 | %}
105 | subplot(2,2,3)
106 | plot(t,real(delta)*1000,'.-b','Color',[0.9290 0.6940
    | 0.1250])
107 | axis([tmin tmax -50 100])
```

```

108 y1=get(gca,'ylim');
109 hold on
110 ax = gca;
111 ax.XTick = 0:40:tmax;
112 ax.YTick = -50:25:100;
113 plot([t_imag t_imag],y1,'Color',[0 0.5 0],'LineWidth',2)
114 xlabel('t [s]')
115 ylabel('\delta [mm]')
116 title('Mean pool depth, Method 2')
117 hold off
118
119 %{
120     Plotting the front velocity vector vs. time. Marking
121     where the solution becomes complex.
122 %}
123 subplot(2,2,4)
124 plot(t,real(v),'.-','Color',[0.4940 0.1840
125     0.5560])
126 axis([tmin tmax 0 0.4])
127 y1=get(gca,'ylim');
128 hold on
129 ax = gca;
130 ax.XTick = 0:40:tmax;
131 ax.YTick = 0:0.1:0.4;
132 plot([t_imag t_imag],y1,'Color',[0 0.5 0],'LineWidth',2)
133 xlabel('t [s]')
134 ylabel('v [m/s]')
135 title('Front velocity, Method 2')
136 hold off

```

```

1 function dudt=myode3(t,u,C,mdot_evap,rho,mt,mdot_in,m_in
2 )
3 % Called by "poolradius_diff.m"
4 % Defines the vector of ODEs, dudt. u(1) = r(t), u(2) =
5 delta(t).
6 dudt = zeros(2,1);
7 % Interpolates mdot_in and m_in
8 mdot_in = interp1(mt,mdot_in,t);
9 m_in = interp1(mt,m_in,t);
10 % Defining the ODEs
11 dudt(1) = C*u(2).^(1/2);
12 dudt(2) = (1/rho)*((mdot_in.*u(1)-2*m_in.*dudt(1))/(pi*u
13 (1).^3)-mdot_evap);
14 end

```